

Master Thesis



Czech  
Technical  
University  
in Prague

**F3**

Faculty of Electrical Engineering  
Department of Control Engineering

## Vehicle battery state and parameters estimator for demonstration vehicle

**Ondřej Masopust**

Supervisor: Ing. David Vošahlík  
Field of study: Cybernetics and Robotics  
January 2024



## Acknowledgements

All thanks go to God in the first place. He created all the things that we now can discover. He created all the materials and theory that we can use to develop complex and fascinating things such as a battery management system for an electric vehicle. In the second place, huge thanks go to my supervisor and other colleagues from Garrett Motion Company, who made this thesis possible. In addition, my wife and my daughter are a big part of the achievement I was able to make during work on this thesis. They supported me and stayed with me, although my studies were sometimes at the expense of family time together. They will eventually enjoy free family weekends if the Lord wills. Last but not least, I want to thank my dear friend Matthew Smith who did the final grammar proofreading.

An artificial intelligence (AI) tool for grammar checking and enhancements was used. No content was generated by the AI. The author reviewed the changes proposed by the tool and takes full responsibility for the content.

## Declaration

I declare that the presented work was developed independently and that I have listed all sources of information used within it in accordance with the methodical instructions for observing the ethical principles in the preparation of university theses.

Prague, January 9<sup>th</sup> 2024

.....

Author's signature

## Abstract

This thesis describes the development of a state estimator for an electric vehicle battery. Battery cell models are discussed, and the so-called 2RC equivalent circuit model is selected. The cell model is improved in state of charge (SOC) modeling and the thermal dynamics execution complexity. Next, model identification is described using laboratory measured data obtained from the Department of Electrotechnology, Czech Technical University in Prague. Challenges related to model identification at low SOC values are discussed. After model parameter estimation is described, the cell model state estimator is presented. Conventional unscented Kalman Filter and its improved implementation called square root unscented Kalman Filter (SR-UKF) are presented and implemented. Further, numerical enhancements are described and implemented. In the last step, the state estimator is validated using the measured data. The SR-UKF is compared with an extended Kalman filter (EKF), which was previously implemented in [12]. Overall, EKF and SR-UKF appear to perform similarly with respect to root mean square error (RMSE) values. Although EKF does not exhibit significant execution time on average, UKF's execution time is superior.

**Keywords:** battery management system, mathematical modeling, filtering, Kalman filter, battery, electric vehicle

**Supervisor:** Ing. David Vošahlík  
Charles Square 13  
Prague 2, 120 00, New Town

## Abstrakt

Tato práce se zabývá vývojem odhadovače stavu pro baterii elektrického vozidla. Možnosti modelování článku baterie jsou porovnány a z nich je vybrán tzv. 2RC model ekvivalentního elektrického obvodu. Matematický model je vylepšen v odhadování stavu nabití baterie (SOC) a teplotní dynamika je vylepšena z pohledu výpočetní složitosti. Dále je popsána identifikace modelu z dat, která byla převzata z Katedry Elektrotechnologie, Českého vysokého učení technického v Praze. Zmíněny jsou i výzvy spojené s modelováním článku v rozmezí nízkých hodnot SOC. Po identifikaci modelu je uveden odhadovač stavu baterie. Běžný “unscented Kalman filter” a jeho vylepšená implementace “square root unscented Kalman filter” (SR-UKF) jsou představeny a naimplementovány. Dále jsou popsána určitá numerická vylepšení, která jsou následně naimplementována. Jako poslední krok je estimátor stavu validován pomocí naměřených dat. SR-UKF je porovnán s “extended Kalman filter” (EKF), který byl dříve naimplementován v [12]. Celkově odhadují EKF a SR-UKF srovnatelně z pohledu hodnot směrodatné odchylky (RMSE). Na druhou stranu, SR-UKF dominuje v testech měřících výpočetní čas na cílovém počítači.

**Klíčová slova:** systém správy baterie, matematické modelování, filtrace, Kalmanův filtr, baterie, elektrické vozidlo

**Překlad názvu:** Návrh systému odhadování stavu a parametrů baterky pro demonstrační vozidlo

# Contents

<b>Project Specification</b>	<b>1</b>	4.7 Conclusion of the Identification Phase . . . . .	47
<b>1 Introduction</b>	<b>3</b>	<b>5 State Estimation and Filtering</b>	<b>49</b>
1.1 Thesis Goal and Overview . . . . .	4	5.1 State of Health Estimation . . . . .	49
<b>2 Measurements</b>	<b>7</b>	5.2 Conventional Unscented Kalman Filter . . . . .	50
2.1 Cells and Measurement Conditions	7	5.2.1 Matlab Implementation . . . . .	50
2.2 Capacity and Open Circuit Voltage Measurements . . . . .	8	5.2.2 Numerical Robustness Issues	51
2.3 Pulse Measurements . . . . .	11	5.3 Square Root UKF . . . . .	52
2.4 Driving Profiles . . . . .	11	5.4 Covariance Matrix Recovery . . . . .	52
<b>3 Mathematical Model</b>	<b>15</b>	5.4.1 Covariance Decomposition . . . . .	53
3.1 Cell Model . . . . .	15	5.4.2 Numerical Tolerance for Positive Definiteness . . . . .	53
3.1.1 2RC Model . . . . .	15	5.4.3 Eigenvalue Manipulation . . . . .	54
3.1.2 Enhancing SOC Modeling . . . . .	16	5.4.4 Composition of the Modified Matrix . . . . .	55
3.1.3 Simplifying Thermal Dynamics	18	5.4.5 Computation of the Returned Cholesky Factor . . . . .	56
3.1.4 State of Health Modeling . . . . .	18	5.5 Possible Improvements . . . . .	56
3.1.5 Considering the Effect of Coulombic Efficiency . . . . .	19	5.6 Conclusion of the Estimator Implementation Phase . . . . .	57
3.1.6 Full dynamic model . . . . .	20	<b>6 Testing and Validation</b>	<b>59</b>
3.2 Battery Pack Modeling . . . . .	21	6.1 Root Mean Square Error . . . . .	59
3.2.1 Battery Pack Structure . . . . .	21	6.2 Validation of Neglecting Coulombic Efficiency . . . . .	59
3.2.2 Augmenting the Cell Model to the Whole Pack . . . . .	21	6.3 Estimator MIL Validation . . . . .	60
3.3 Implementation in Matlab . . . . .	23	6.3.1 Incorrect Initial Conditions . . . . .	61
3.4 Conclusion of the Modeling Phase	24	6.3.2 Capacity Degradation . . . . .	64
<b>4 Model Identification</b>	<b>27</b>	6.3.3 Temperature Behavior . . . . .	66
4.1 Cell Capacity . . . . .	27	6.4 Estimator RDE Data Validation	70
4.2 Open-circuit Voltage . . . . .	27	6.5 Execution Time Measurement . . . . .	71
4.2.1 Comparison with Pulse Data	30	<b>7 Conclusion</b>	<b>75</b>
4.3 Internal Resistance . . . . .	31	7.1 Overall Results . . . . .	75
4.3.1 Extracting Values from the Data . . . . .	31	7.2 Possible Extensions of this Work	76
4.3.2 Considering Dependence on the C-rate . . . . .	32	<b>A Bibliography</b>	<b>79</b>
4.3.3 Measured Data Fitting . . . . .	32		
4.4 RC Couples . . . . .	37		
4.4.1 Identification Method . . . . .	37		
4.4.2 Limitations of the Method Used . . . . .	39		
4.4.3 Identification at Low SOC Values . . . . .	40		
4.4.4 Final RC Estimation Results	41		
4.5 Thermal Dynamics . . . . .	44		
4.6 Comparison of the Identified Model and Measured Data . . . . .	44		

## Figures

<p>1.1 Tesla Cybertruck, adopted from [11] . . . . . 3</p> <p>2.1 Demonstration of the first phase of capacity and OCV measurement, which took place at 0 °C, discharge current was 0.11 A . . . . . 9</p> <p>2.2 Demonstration of the second phase of capacity and OCV measurement, which took place at 25 °C. This phase was measured 2 hours after the first phase took place. The discharge current was 0.11 A. . . . . 9</p> <p>2.3 Demonstration of the third phase of capacity and OCV measurement, which took place at 0 °C, charge current was 0.11 A . . . . . 10</p> <p>2.4 Demonstration of the fourth phase of capacity and OCV measurement, which took place at 25 °C. This phase was measured 2 hours after the third phase took place. The charge current was 0.11 A. . . . . 10</p> <p>2.5 Pulse measurement illustration . 11</p> <p>2.6 US06 driving profile measurement illustration . . . . . 12</p> <p>3.1 Schematics of the 2RC equivalent circuit model, <i>OCV</i> stands for an open circuit voltage . . . . . 16</p> <p>3.2 Schematic of the battery . . . . . 21</p> <p>3.3 Comparison of drive cycle measurements of all 3 measured cells 22</p> <p>4.1 Transfer characteristic between the open-circuit voltage and the state of charge of one cell at -10 °C. Comparison of charge, discharge and final characteristic. . . . . 28</p> <p>4.2 Transfer characteristic between the open-circuit voltage and the state of charge of one cell at 0 °C. Comparison of charge, discharge and final characteristic. . . . . 28</p>	<p>4.3 Transfer characteristic between the open-circuit voltage and the state of charge of one cell at 25 °C. Comparison of charge, discharge and final characteristic. . . . . 29</p> <p>4.4 Transfer characteristic between the open-circuit voltage and the state of charge of one cell at 50 °C. Comparison of charge, discharge and final characteristic. . . . . 29</p> <p>4.5 Transfer characteristics between the open circuit voltage and the state of charge of one cell for different temperatures . . . . . 31</p> <p>4.6 Demonstration of an immediate terminal voltage drop at the start of a current pulse . . . . . 32</p> <p>4.7 <math>R_0</math> dependence on C-rate for different SOC values, new cell [33] 33</p> <p>4.8 <math>R_0</math> dependence on C-rate for different SOC values, aged cell [33] 33</p> <p>4.9 Measured <math>R_0</math> dependence on C-rate for different SOC values . . . 34</p> <p>4.10 Comparison of measured and fitted characteristic of internal resistance at -10 °C . . . . . 35</p> <p>4.11 Comparison of measured and fitted characteristic of internal resistance at 0 °C . . . . . 35</p> <p>4.12 Comparison of measured and fitted characteristic of internal resistance at 25 °C . . . . . 36</p> <p>4.13 Comparison of measured and fitted characteristic of internal resistance at 50 °C . . . . . 36</p> <p>4.14 Transfer characteristics between the cell's internal resistance and the state of charge at different temperatures, and final fitted polynomials . . . . . 37</p> <p>4.15 Demonstration of the border point (red) when effect of the 2<sup>nd</sup> RC pair starts to dominate the 1<sup>st</sup> RC pair. The green points indicate the start and end of the transition period . . 38</p>
---	---

4.16 Explanation of the terms “active” and “passive” part of the current pulse . . . . .	39	6.9 Estimator validation, response to nominal capacity decrease, state of charge course . . . . .	66
4.17 Demonstration of different dynamics for the active and passive part of a pulse . . . . .	40	6.10 Estimator validation, response to ambient temperature change, terminal voltage course . . . . .	67
4.18 Demonstration of poor fitting at low SOC values, excerpt from measurement taken at 25 °C . . . . .	41	6.11 Estimator validation, response to ambient temperature change, nominal capacity course . . . . .	68
4.19 Final values of $R_1$ parameter . .	42	6.12 Estimator validation, response to ambient temperature change, depleted charge course . . . . .	68
4.20 Final values of $C_1$ parameter . .	42	6.13 Estimator validation, response to ambient temperature change, state of charge course . . . . .	69
4.21 Final values of $R_2$ parameter . .	43	6.14 Estimator validation, response to ambient temperature change, ambient temperature course . . . . .	69
4.22 Final values of $C_2$ parameter . .	43	6.15 Estimator validation, RDE data scenario, terminal voltage course . .	70
4.23 Validation of a cell model using UDDS data, -10 °C . . . . .	45	6.16 Estimator validation, RDE data scenario, nominal capacity course .	71
4.24 Validation of a cell model using UDDS data, 0 °C . . . . .	45	6.17 Estimator validation, RDE data scenario, depleted charge course . .	72
4.25 Validation of a cell model using UDDS data, 25 °C . . . . .	46	6.18 Estimator validation, RDE data scenario, state of charge course . .	72
4.26 Validation of a cell model using UDDS data, 50 °C . . . . .	46	6.19 Histogram of execution times on the target computer . . . . .	73
4.27 Voltage $V_2$ generated by the cell model, -10 °C . . . . .	47		
6.1 MIL scenario schematic . . . . .	60		
6.2 Estimator validation, response to incorrect filter initial conditions, terminal voltage course . . . . .	62		
6.3 Estimator validation, response to incorrect filter initial conditions, nominal capacity course . . . . .	62		
6.4 Estimator validation, response to incorrect filter initial conditions, depleted charge course . . . . .	63		
6.5 Estimator validation, response to incorrect filter initial conditions, state of charge course . . . . .	63		
6.6 Estimator validation, response to nominal capacity decrease, terminal voltage course . . . . .	64		
6.7 Estimator validation, response to nominal capacity decrease, nominal capacity course . . . . .	65		
6.8 Estimator validation, response to nominal capacity decrease, depleted charge course . . . . .	65		

## Tables

2.1 Cells ( $C_i$ ) division based on measurement conditions . . . . .	7
3.1 Discharge capacity measurements, Dchgd. Capacity reflects the capacity discharged at a given temperature, Capacity Left reflects the capacity discharged at 25 °C after the battery achieved a steady state at 25 °C . .	17
3.2 Charge capacity measurements, Chgd. Capacity reflects the capacity charged at a given temperature, Capacity Left reflects the capacity charged at 25 °C after the battery achieved a steady state at 25 °C. .	18
3.3 Capacity and coulombic efficiency values of one cell with respect to temperature, computed from the measured data. . . . .	20
3.4 Matlab model parameters . . . . .	23
4.1 Coefficients values of fitting polynomial for the transfer function of the internal resistance for different temperatures. . . . .	34
6.1 Difference in total drained capacity, absolute difference and relative difference with respect to total drained capacity. . . . .	60
6.2 RMSE values for estimator validation, incorrect initial condition scenario . . . . .	61
6.3 RMSE values for estimator validation, $C_0$ decrease scenario . . .	64
6.4 RMSE values for estimator validation, ambient temperature change scenario . . . . .	67
6.5 RMSE values for estimator validation, RDE data scenario . . . .	70
6.6 Execution time statistics, comparison of SR-UKF and EKF .	71



## I. Personal and study details

Student's name: **Masopust Ond ej**

Personal ID number: **483591**

Faculty / Institute: **Faculty of Electrical Engineering**

Department / Institute: **Department of Control Engineering**

Study program: **Cybernetics and Robotics**

## II. Master's thesis details

Master's thesis title in English:

**Vehicle battery state and parameters estimator for demonstration vehicle**

Master's thesis title in Czech:

**Návrh systému odhadování stavu a parametrů baterky pro demonstrační vozidlo**

Guidelines:

The goal of this thesis is to implement algorithms for estimation of vehicle battery state of charge and state of health. The thesis will consist of the following steps:

- 1) Get familiar with battery mathematical modeling, state estimation, and degradation models.
- 2) Derive battery parameters like capacity, internal resistance etc. as a function of the battery state variables (e.g. temperature). Adopt parameter estimation algorithm and identify the battery model from measurements.
- 3) Adopt battery estimation algorithms previously implemented in the team.
- 4) Propose estimation algorithm augmentation for the battery state and parameters estimation.
- 5) Validate and compare all implemented estimators.

Bibliography / sources:

- [1] Lewis, F. L., L. Xie, D. Popa: Optimal and Robust Estimation: With an Introduction to Stochastic Control Theory, CRC Press, 2005. ISBN 978-1-4200-0829-6
- [2] Simon, D.: Optimal State Estimation: Kalman, H Infinity, and Nonlinear Approaches. Wiley, 2006, ISBN: 978-0-471-70858-2
- [3] Dieter Schramm, Manfred Hiller, Roberto Bardini – Vehicle Dynamics – Duisburg 2014
- [4] Robert Bosch GmbH - Bosch automotive handbook - Plochingen, Germany : Robert Bosch GmbH ; Cambridge, Mass. : Bentley Publishers

Name and workplace of master's thesis supervisor:

**Ing. David Vošahlík Department of Control Engineering FEE**

Name and workplace of second master's thesis supervisor or consultant:

Date of master's thesis assignment: **04.09.2023**

Deadline for master's thesis submission: **09.01.2024**

Assignment valid until:

**by the end of summer semester 2023/2024**

Ing. David Vošahlík  
Supervisor's signature

prof. Ing. Michael Šebek, DrSc.  
Head of department's signature

prof. Mgr. Petr Páta, Ph.D.  
Dean's signature

## III. Assignment receipt

The student acknowledges that the master's thesis is an individual work. The student must produce his thesis without the assistance of others, with the exception of provided consultations. Within the master's thesis, the author must state the names of consultants and include a list of references.

\_\_\_\_\_  
Date of assignment receipt

\_\_\_\_\_  
Student's signature



# Chapter 1

## Introduction

Nowadays, electric vehicles are rapidly evolving. For example, it can be seen that from the start of production of the Tesla Roadster, which was the first electric vehicle (EV) produced by Tesla<sup>1</sup>, in 2008, Tesla evolved into an EV development giant, which is now producing futuristic vehicles such as the new Tesla Cybertruck, which is supposedly built for any planet.<sup>2</sup> Although Tesla



**Figure 1.1:** Tesla Cybertruck, adopted from [11]

can be considered a pioneer who pushed the EV industry forward, Tesla's innovative approach is not the only driving force. Recent activist events raise awareness about environmental pollution and its possible consequences. Partly because of that, new emission standards are published that aim at lowering the emissions as much as possible. For example, the Euro 7 emission standard [25] contains stricter rules regarding exhaust particle emissions. EVs and hybrid electric vehicles are promising relief from the high pollution caused by cars in general.

The Smart Driving Solutions research group at the Faculty of Electrical Engineering Czech Technical University in Prague<sup>3</sup> develops a prototype electric vehicle with an individually actuated motor for each wheel. Each motor has a rated power  $\approx 90$  kW. Brakes are controlled using the brake-by-wire approach, which development was conducted in [31]. All brakes are actuated independently. Similarly, steering is implemented as the steer-

<sup>1</sup>[https://en.wikipedia.org/wiki/Tesla,\\_Inc.](https://en.wikipedia.org/wiki/Tesla,_Inc.)

<sup>2</sup>[https://www.tesla.com/en\\_eu/cybertruck](https://www.tesla.com/en_eu/cybertruck)

<sup>3</sup><https://sds.fel.cvut.cz/>

by-wire approach developed in [3]. The vehicle main computer runs Linux with the PREEMPT\_RT patch. The vehicle chassis is adopted from a first-generation Skoda Fabia car and adapted accordingly to meet the electric demonstration vehicle needs.

The overall goal of the project is to develop a prototype platform for testing advanced algorithms for vehicle control. The advantage of developing a custom EV is that by doing so, control over all aspects of the car is granted. Borrowing a car from a large-scale manufacturer involves restrictions caused by complex data protocols and bus communication encryption. As the demonstration EV is still in development, a battery management system (BMS) must be implemented to ensure proper battery handling and state estimation.

## 1.1 Thesis Goal and Overview

This thesis describes the development of a battery state estimator that can be used in the demonstration EV. Generally, a plant model is needed for estimator development. Therefore, a classical procedure consisting of data processing, model selection, model identification, estimator implementation and overall testing, and validation is conducted.

Laboratory measurements were obtained externally. High-accuracy laboratory tools were used at the Department of Electrotechnology, Czech Technical University in Prague to precisely measure the characteristics of a Panasonic cells used in the target demonstration vehicle. Measurements are described in further detail in Chapter 2.

As described later in Chapter 3, battery cell modeling options are presented. An equivalent circuit model is chosen and a more detailed description is provided. Cell modeling modifications are presented that enable improvement in state of charge (SOC) modeling and computational efficiency. The procedure of using a cell model to model the entire vehicle battery pack is described, and a Matlab implementation overview is provided.

Next, model identification is performed. The obtained data are processed and cell model parameters are estimated. The estimation of cell capacity, open-circuit voltage, internal resistance and resistor-capacitor (RC) couple parameters is described in Chapter 4. The resulting parameters are represented as look-up tables depending on the temperature and state of charge. The only exception is cell capacity, which is dependent only on temperature. The cell model is validated using measured data. More details are provided in the aforementioned chapter.

After the model identification, the cell state estimator is presented in Chapter 5. A brief overview of battery state of health modeling and estimation is provided. Unscented Kalman Filter (UKF) and square root unscented Kalman filter (SR-UKF) implementation in Matlab is described. Furthermore, a numerical robustness enhancement algorithm is presented, which makes the implemented estimator robust with respect to runtime errors caused by numerical inaccuracies.

In Chapter 6, testing and validation procedure is described. Successive estimator validation steps are conducted. A comparison between two different estimators is provided, and execution time is measured on the target hardware platform using measured cell data.

Finally, Chapter 7 provides an overall conclusion of this thesis. The results are summarized and evaluated. Furthermore, possible improvements and future follow-up work are proposed.



# Chapter 2

## Measurements

As stated in the introductory chapter, the goal of this thesis is to develop an estimator for an electric vehicle battery pack. For this purpose, battery cell measurements are needed to identify the mathematical model. This chapter describes the measurements, how they were obtained, and their structure. Different measuring scenarios are described and their later usage is briefly outlined.

### 2.1 Cells and Measurement Conditions

Measurements were obtained from the Department of Electrotechnology, Czech Technical University in Prague. The scenarios were measured on Panasonic 18650 NCR cells. [20] NCR denotes the particular cell chemistry that was used. NCR (equivalently NCA) indicates the specific usage of lithium nickel cobalt aluminum oxides ( $LiNiCoAlO_2$ ) with a graphite anode. These cells are used in the target demonstration EV, where the recycled Tesla Model S car battery pack [5] is used.

In total, 12 cells were used in the measurement process. These cells were divided into 2 groups of 6 cells. The first group was used for measurements where active cooling was not incorporated. The second group was used for measurements with active cooling. Active cooling was implemented by heat sinks with fans. Cell dynamics was measured at four different temperatures:  $-10\text{ }^\circ\text{C}$ ,  $0\text{ }^\circ\text{C}$ ,  $25\text{ }^\circ\text{C}$  and  $50\text{ }^\circ\text{C}$ . Each group of cells was divided into sets of 3 cells. The first set was used for the two lower temperature measurements ( $-10\text{ }^\circ\text{C}$ ,  $0\text{ }^\circ\text{C}$ ), and the second set was used for the two higher temperature measurements ( $25\text{ }^\circ\text{C}$ ,  $50\text{ }^\circ\text{C}$ ). All measurements were performed in a thermal chamber to achieve the desired ambient temperature. Table 2.1 shows individual cells division between the measuring scenarios.

<i>Cooling</i> \ <i>Temp.</i> [ $^\circ\text{C}$ ]	-10	0	25	50
Without cooling	$C_1, C_2, C_3$	$C_1, C_2, C_3$	$C_4, C_5, C_6$	$C_4, C_5, C_6$
With cooling	$C_7, C_8, C_9$	$C_7, C_8, C_9$	$C_{10}, C_{11}, C_{12}$	$C_{10}, C_{11}, C_{12}$

**Table 2.1:** Cells ( $C_i$ ) division based on measurement conditions

The measurements always started from a fully charged state. The fully

charged state was achieved using constant-current-constant-voltage (CC-CV) approach. [27] This approach involves charging the battery with constant current until the upper voltage threshold is reached. Then, constant voltage charging begins and continues until the charging current is lower than a specified value.

A direct cell temperature measurement was performed for the scenarios with active cooling. The cell temperature was measured at 4 points: anode, cathode, cell's center upper side and cell's center lower side.

In this thesis, three types of cell measurements were used.

- capacity and open-circuit voltage measurements
- pulse measurements
- driving profiles

The following sections describe each of these measurement types.

## ■ 2.2 Capacity and Open Circuit Voltage Measurements

Capacity and open-circuit voltage (OCV) were measured simultaneously using one identical scenario. These measurements were performed without heat sinks, i.e., the first group of cells was used ( $C_{1..6}$ ). The measurement scenario was adopted from [21]. The procedure involves starting with a fully charged cell. A specific test temperature is selected, e.g.  $0\text{ }^{\circ}\text{C}$ . The cell is discharged at the test temperature by a low ( $C/30$ ) current until the terminal voltage reaches a given lower threshold value ( $2.5\text{ V}$ ). This threshold was chosen based on typical lithium cell operating range. Then, the cell is placed in  $25\text{ }^{\circ}\text{C}$  and after 2 hours the battery is (dis)charged to achieve a terminal voltage equal to the threshold value. After that, the cell is charged at the test temperature with current of  $C/30$  amplitude until the upper threshold ( $4.2\text{ V}$ ) is reached. Finally, the cell is put into  $25\text{ }^{\circ}\text{C}$  again and after 2 hours, it is (dis)charged to achieve a terminal voltage of  $4.2\text{ V}$ . During this entire procedure, the terminal voltage and accumulated ampere-hours are recorded. A demonstration of this procedure is shown in Figures 2.1, 2.2, 2.3 and 2.4. They depict the procedure for measuring OCV and capacity at  $0\text{ }^{\circ}\text{C}$ .

It is assumed that by using very low discharge current, the battery dynamics is not very excited and thus negligible. Discharge and charge OCV curves must be processed to obtain the final OCV curve dependent on the SOC. Measurement processing is further described in Chapter 4, which is dedicated to model identification.

This scenario was measured at sample time  $T_s = 1\text{ s}$ .



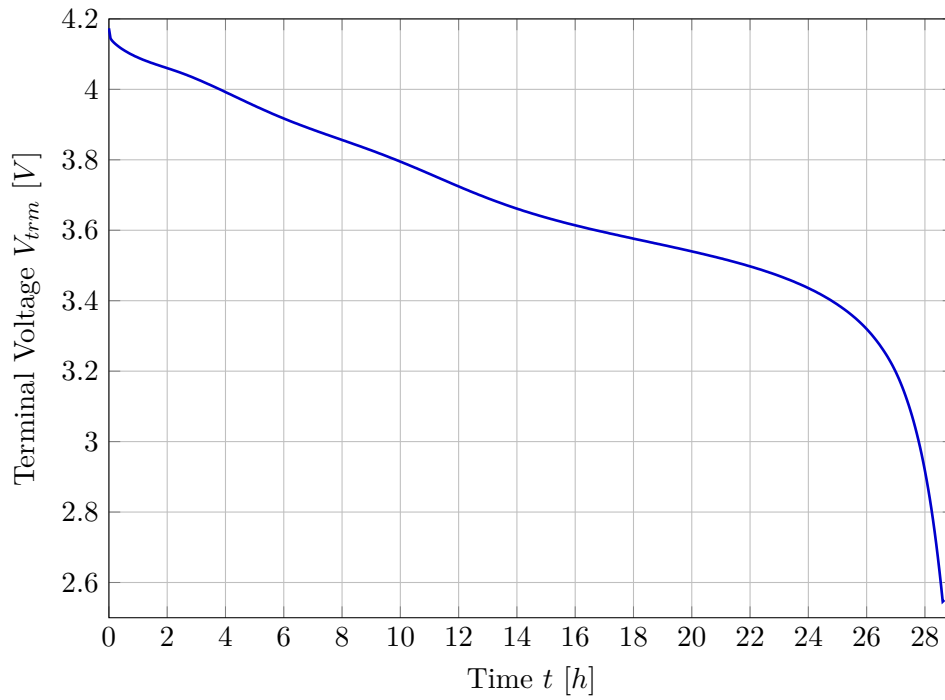


**Figure 2.1:** Demonstration of the first phase of capacity and OCV measurement, which took place at  $0\text{ }^{\circ}\text{C}$ , discharge current was  $0.11\text{ A}$

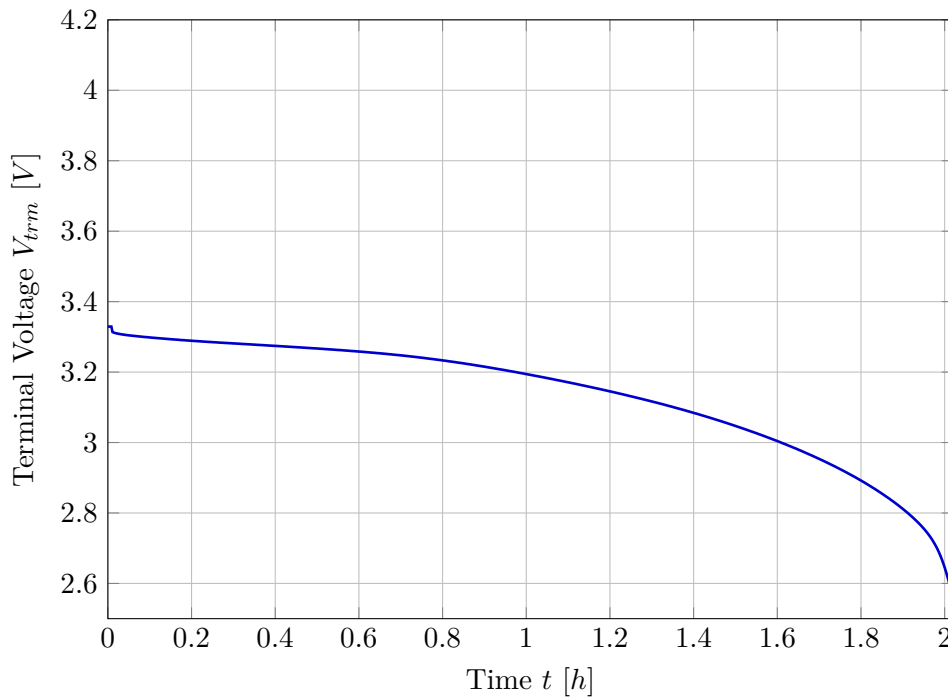


**Figure 2.2:** Demonstration of the second phase of capacity and OCV measurement, which took place at  $25\text{ }^{\circ}\text{C}$ . This phase was measured 2 hours after the first phase took place. The discharge current was  $0.11\text{ A}$ .

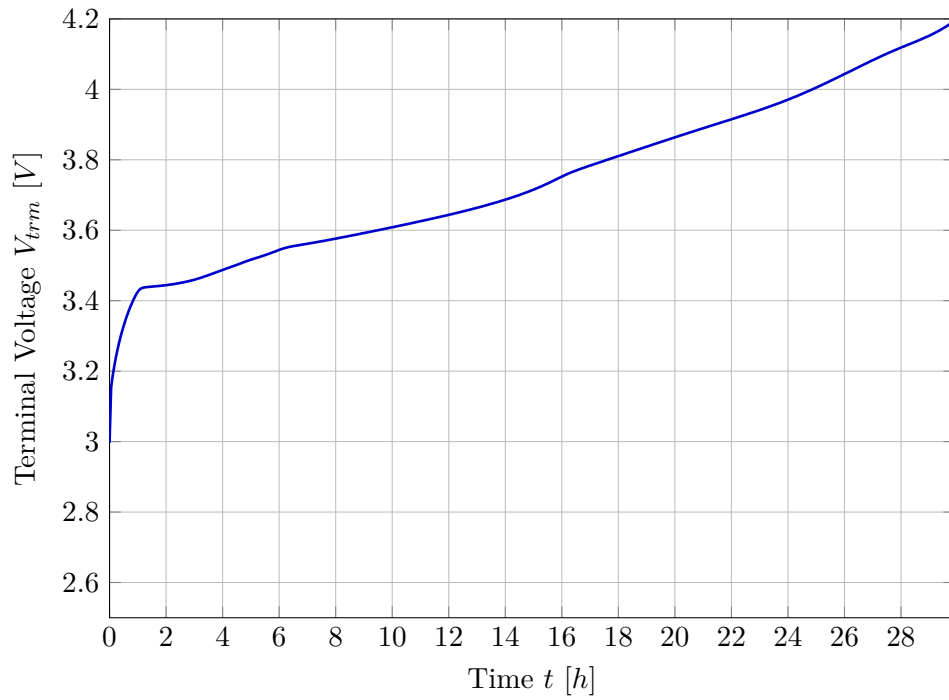


**Figure 2.3:** Demonstration of the third phase of capacity and OCV measurement, which took place at  $0\text{ }^{\circ}\text{C}$ , charge current was  $0.11\text{ A}$

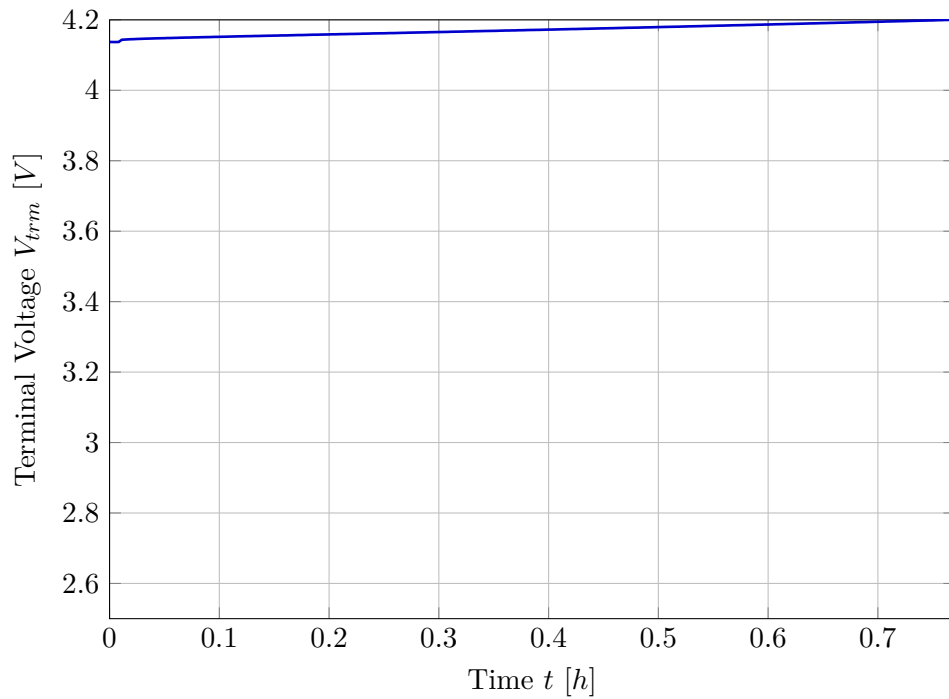


**Figure 2.4:** Demonstration of the fourth phase of capacity and OCV measurement, which took place at  $25\text{ }^{\circ}\text{C}$ . This phase was measured 2 hours after the third phase took place. The charge current was  $0.11\text{ A}$ .

## 2.3 Pulse Measurements

The pulse measurements consist of discharging the cell with successive current pulses until a terminal voltage lower threshold is reached. Then, a pulse charging procedure, that is similar to the discharge procedure, is conducted. An upper voltage threshold was considered as the end of the measurement. Active cooling was incorporated into these measurements. Thus, the second group of cells was used ( $C_{7...12}$ ).

These measurements are suitable for estimating the equivalent circuit model parameters. Namely, internal resistance ( $R_0$ ) and RC pairs ( $R_1, C_1, R_2$  and  $C_2$ ). The equivalent circuit model used is described in Section 3.1.

An excerpt from the measurement can be seen in Figure 2.5. A regular

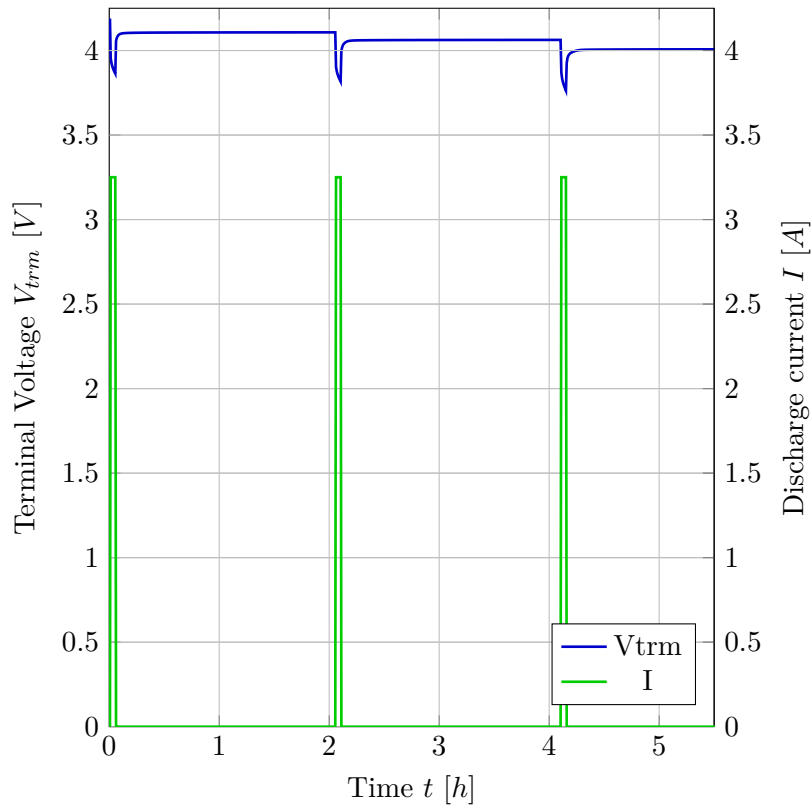


**Figure 2.5:** Pulse measurement illustration

discharge pulse lasted for 3 minutes. A 2 hour resting time was inserted between each discharge cycle to allow the battery to achieve a steady state. Measurement sample time  $T_s = 0.1$  s was used.

## 2.4 Driving Profiles

The last measurement scenarios used in this thesis were the driving profiles. International standard and certification organizations use predefined cycles

(the so called dynamometer drive schedules) to test car's fuel consumption and emissions production. [1] These driving cycles are used to imitate real driving experience for different conditions (e.g. driving on a highway or in a city). Current profiles based on the drive schedules were applied to the battery cell repeatedly until the low-level voltage threshold was met.

The following driving profiles were measured.

- Urban Dynamometer Driving Schedule (UDDS), which represents city driving conditions [1]
- US06, which represents an aggressive driving schedule [1]
- Worldwide harmonized Light duty driving Test Cycle (WLTC), which represents an internationally accepted driving cycle developed for general light vehicle testing [30]

An excerpt from the US06 driving profile can be seen in Figure 2.6.

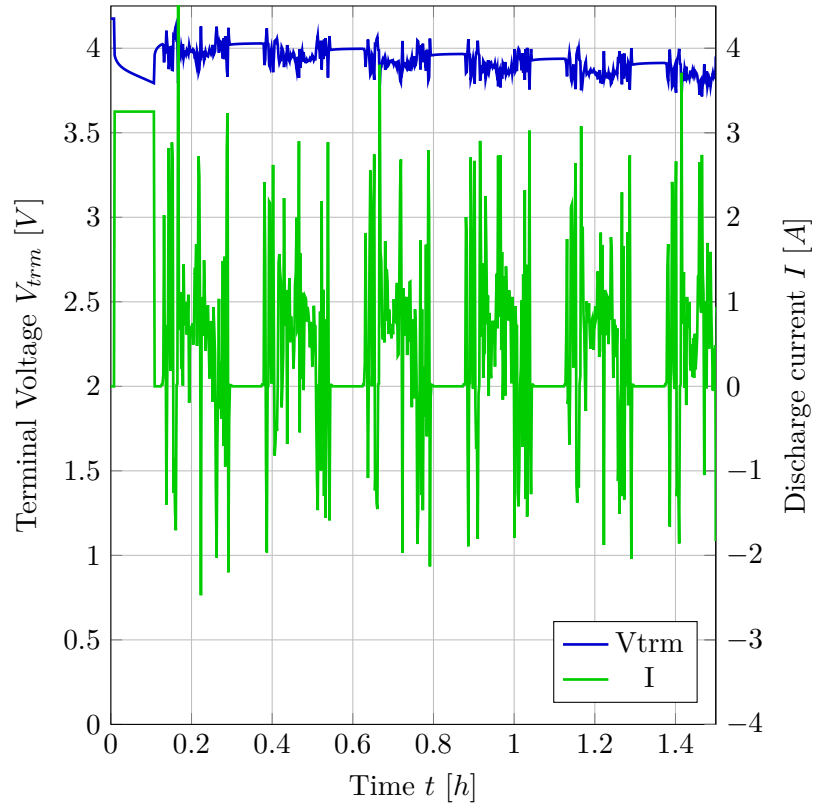


**Figure 2.6:** US06 driving profile measurement illustration

The driving profiles were used mainly for the validation of the final model and estimator. The measured signals were compared with the simulated and estimated outputs. Validation using driving profile data is described in Chapter 6.

Measurement sample time  $T_s = 0.1$  s was used.





## Chapter 3

### Mathematical Model

To develop a battery pack estimation algorithm, a mathematical model of the battery pack needs to be derived beforehand. Generally, when modeling an electric vehicle battery pack, a single cell model is first established and is later augmented to reflect the pack behavior. [22]

This chapter describes the development of the cell mathematical model. Further, modeling of the entire battery pack and implementation of the cell model in Matlab are given. Finally, a conclusion with a discussion on the selected modeling approach is presented.

#### 3.1 Cell Model

As stated in the introduction to this chapter, a cell model is developed first and later augmented to reflect the entire battery pack. Such a procedure can be seen e.g. in [22]. As it is described in [22], there are two main approaches to cell modeling. An equivalent-circuit model (ECM) consists of modeling the cell as an electrical circuit. The second approach is called physics-based modeling (PBM). These are based on first-principles modeling, including electrochemical reactions.

As a starting point, an ECM mathematical model from [12] was selected. Choice of ECM in [12] is further justified by being a “sweet spot of both acceptable accuracy, complexity, and computational effort.” As it is stated in [22] “equivalent-circuit type models are used extensively (almost exclusively) as the basis for real-time control algorithms in commercial battery packs.” Although it is written in [22] that PBMs can be reduced to similar a complexity as ECMs, ECMs are used more widely.

The decision to adopt a model from [12] was also made because it was desirable to continue the team development conducted previously. In addition, Garrett Motion, which supported this thesis, aimed at improving their models, which were partly based on [12].

##### 3.1.1 2RC Model

In [12], the author’s main target was mainly battery state of charge (SOC) and state of health (SOH) estimation in a student formula car for improving

competition results. The model adopted from [12] is structured as follows.

$$\dot{SOC}(t) = -\frac{I(t)}{Q_{max}} \quad (3.1)$$

$$\dot{V}_1(t) = -\frac{V_1(t)}{R_1 C_1} + \frac{I(t)}{C_1} \quad (3.2)$$

$$\dot{V}_2(t) = -\frac{V_2(t)}{R_2 C_2} + \frac{I(t)}{C_2} \quad (3.3)$$

$$\dot{T}_{bat}(t) = \frac{V_1(t)I(t)}{C_{th}} + \frac{V_2(t)I(t)}{C_{th}} + \frac{R_0(SOC, T_{bat}) \cdot I(t)^2}{C_{th}} + \frac{T_{air}(t) - T_{bat}(t)}{R_{th} C_{th}} \quad (3.4)$$

$$\dot{Q}_{max}(t) = 0 \quad (3.5)$$

$I(t)$  denotes input current,  $Q_{max}$  stands for maximum available charge,  $V_1$  stands for voltage on the first RC pair,  $R_1$  and  $C_1$  stand for values of the first RC pair elements,  $V_2$ ,  $R_2$ , and  $C_2$  are equivalent for the second RC pair,  $T_{bat}$  stands for battery temperature,  $C_{th}$  stands for thermal capacitance,  $R_{th}$  stands for thermal resistance,  $R_0$  stands for internal resistance and  $T_{air}$  stands for temperature of the ambient air.

As can be seen, the so-called 2RC version of ECM is used, which describes an equivalent circuit of a structure, as shown in Figure 3.1. The meaning of 2RC stems from the use of an electrical circuit consisting of two resistor-capacitor (RC) pairs.

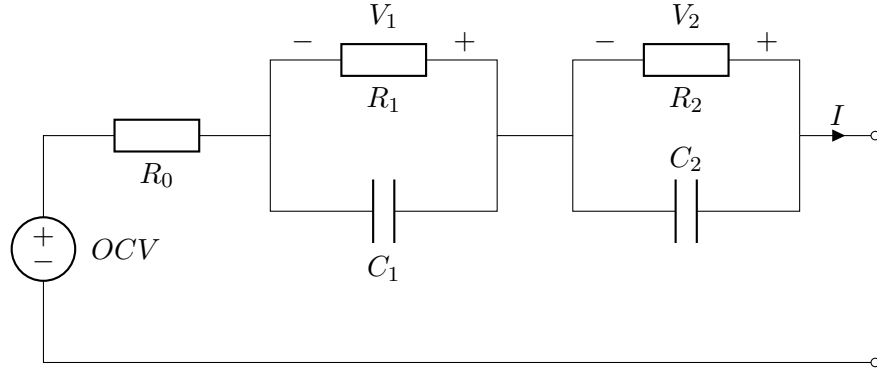


**Figure 3.1:** Schematics of the 2RC equivalent circuit model,  $OCV$  stands for an open circuit voltage

### 3.1.2 Enhancing SOC Modeling

A drawback of the adopted model is its approach to modeling SOC. The author of [12] chose to interpret SOC based on [8], which is taken as the ratio of the available charge to the total charge.

$$SOC = \frac{Q_{cur}}{Q_{max}} \cdot 100 \quad (3.6)$$



As it is stated in [12], this approach does not reflect the temperature dependency of  $Q_{max}$ . However, a simple solution was found in [9] where the authors used an approach of exchanging the  $SOC$  state by a state that represents the charge depleted from the battery with respect to a fully charged state. The state equation describing the dynamics of this state is then as simple as

$$\dot{Q}_d = I. \quad (3.7)$$

The momentary  $SOC$  can then be computed as an output equation

$$SOC = 100 \cdot \left(1 - \frac{Q_d}{C \cdot 3600}\right), \quad (3.8)$$

where  $C$  is the battery capacity available at the current moment with respect to the operating conditions (mainly temperature and age). Scaling by a factor of 3600 represents the conversion from ampere-hours (Ah) to ampere-seconds (As).

This approach of modeling SOC, as it is done in [9], is more supported by section 2.10.6 of [21], where it is shown that the total normalized capacity (available charge) is constant for all operating conditions. However, what changes with operating conditions is the capacity that the user can drain from the battery. This is deduced from the fact that while discharging the battery at  $-10\text{ }^\circ\text{C}$ , a low voltage threshold of  $2.5\text{ V}$  is reached for a lower amount of depleted charge compared to the situation when the battery is discharged at a higher temperature. However, after warming up the cell from  $-10\text{ }^\circ\text{C}$  to room temperature, the battery can provide some additional charge before the  $2.5\text{V}$  threshold is reached again. If the charge depleted from the battery at  $-10\text{ }^\circ\text{C}$  is summed up with the charge depleted later after rest at room temperature, a similar result is obtained as if the discharge phase was performed at room temperature. The obtained measurement data presented in Tables 3.1 and 3.2 support this fact. As can be seen, the total

Temp. [ $^\circ\text{C}$ ]	Dchgd. Capacity [Ah]	Capacity Left [Ah]	Sum [Ah]
-10	2.95	0.41	3.37
0	3.15	0.22	3.38
25	3.37	0.02	3.39
50	3.38	0.01	3.39

**Table 3.1:** Discharge capacity measurements, Dchgd. Capacity reflects the capacity discharged at a given temperature, Capacity Left reflects the capacity discharged at  $25\text{ }^\circ\text{C}$  after the battery achieved a steady state at  $25\text{ }^\circ\text{C}$

(dis)charged capacity, which is presented in the column Sum, does not vary as much with respect to temperature. This capacity is further referred to as the *total capacity*. However, the capacity (dis)charged at the given temperature varies by hundreds of milliampere-hours. This capacity is further referred to as the *available capacity*. Similar definitions are provided in Section 3.2 of [22].

Temp. [°C]	Chgd. Capacity [Ah]	Capacity Left [Ah]	Sum [Ah]
-10	3.19	0.18	3.37
0	3.30	0.08	3.38
25	3.39	0.03	3.42
50	3.42	0.02	3.45

**Table 3.2:** Charge capacity measurements, Chgd. Capacity reflects the capacity charged at a given temperature, Capacity Left reflects the capacity charged at 25 °C after the battery achieved a steady state at 25 °C.

An immediate improvement in the modeling approach described by equations (3.7) and (3.8) can be seen from the fact that the proposed approach reflects changes in SOC when no power is drained from the battery and only the operating temperature is changed. Consider a situation in which a 50% charged electric vehicle stands in a garage at 25 °C. When the owner forgets to close the garage door in winter and the battery is cooled down, the available capacity changes. The proposed modeling approach reflects that in a way that the SOC value at the output changes accordingly.

### 3.1.3 Simplifying Thermal Dynamics

Furthermore, the thermal dynamics was simplified. In [12], a thermal model of the form

$$\dot{T}_{bat}(t) = \frac{V_1(t)I(t)}{C_{th}} + \frac{V_2(t)I(t)}{C_{th}} + \frac{R_0I(t)^2}{C_{th}} + \frac{T_{air}(t) - T_{bat}(t)}{R_{th}C_{th}} \quad (3.9)$$

is used. The voltage drops on resistors  $R_1$  and  $R_2$  are small and are further divided by the parameter  $C_{th}$ . Therefore, the first two terms in equation (3.9) are negligible. Removing them does not introduce significant errors. A new proposed thermal model has a structure

$$\dot{T}_{bat}(t) = \frac{R_0I(t)^2}{C_{th}} + \frac{T_{air}(t) - T_{bat}(t)}{R_{th}C_{th}}. \quad (3.10)$$

Another advantage of this simplification is that it improves computational efficiency.

### 3.1.4 State of Health Modeling

As it is stated in [12] and [22], battery SOH is mostly defined on the basis of either a gradual capacity decrease or an internal resistance increase. A standard definition of SOH is not established and BMS engineers need to make choices about how to represent and calculate SOH. Furthermore, it is proposed in [22] that with battery aging, not only capacity and internal resistance will change. However, the other parameters that change have a little impact on the overall behavior and thus state-of-the-art battery management systems mostly track either capacity or internal resistance value change or both. Proper SOH estimation is important because it enables detection

when battery degradation reaches a point when its characteristics are below acceptable performance.

As it is written in [22], proper internal resistance estimation has a significant role in available-power calculation. However, later it is stated that for Kalman-based filtering, change of internal resistance value has a minor effect when capacity degradation is estimated. Therefore, defining SOH in terms of capacity decrease is more suitable for this thesis. As it is used also in [12], the suitable SOH definition for this thesis is

$$SOH = 100 \cdot \frac{Q_{max}}{Q_{init}}, \quad (3.11)$$

where  $Q_{max}$  denotes the momentary maximal available capacity which decreases over time and  $Q_{init}$  denotes the maximum available capacity of an unused battery.

As shown in Tables 3.1 and 3.2, the battery's available capacity varies with respect to temperature. It was decided to structure the model in such a way that the battery capacity  $C$  is computed as  $C = C_0 \cdot C_{rel}$ , where  $C_0$  is the nominal capacity independent of temperature and  $C_{rel}$  stands for relative capacity, which is temperature dependent. More information is provided in Section 4.1. The  $C_0$  value is then subject to age capacity degradation estimation. Thus equivalently, (3.11) can be redefined as

$$SOH = 100 \cdot \frac{C_0}{C_{0,init}}, \quad (3.12)$$

where  $C_{0,init}$  is the value of  $C_0$  of a new cell. The estimation of  $C_0$  is covered in Chapter 5 of this thesis.

### ■ 3.1.5 Considering the Effect of Coulombic Efficiency

Another parameter that is generally present in cell models is the so-called coulombic efficiency, which models the different behaviour of the cell when charging compared to discharging. In [21], coulombic efficiency at room temperature (25 °C), is defined as

$$\eta(25^\circ C) = \frac{Q_{dch}}{Q_{ch}}, \quad (3.13)$$

where  $Q_{dch}$  represents total ampere-hours discharged from the cell at 25 °C and  $Q_{ch}$  represents total ampere-hours charged at 25 °C. In [21], the author provides these definitions with respect to performing cell measurements as described in Section 2.2. Thus the  $Q_{dch}$  and  $Q_{ch}$  values are the sum of ampere-hours (dis)charged at two consecutive steps.

Coulombic efficiencies for temperatures other than 25 °C are defined in a more complex way. Nevertheless, considering the procedures described in Section 2.2 of this thesis, the author of [21] defines the coulombic efficiency for an arbitrary temperature  $T$  as

$$\eta(T) = \frac{Q_{dch}}{Q_{ch,T}} - \eta(25^\circ C) \frac{Q_{ch,25^\circ C}}{Q_{ch,T}}, \quad (3.14)$$

where  $Q_{dch}$  still denotes total ampere-hours discharged from the battery (summed up discharging at temperature  $T$  and consequent discharging at  $25\text{ }^\circ\text{C}$ ),  $Q_{ch,T}$  denotes ampere-hours charged at temperature  $T$  and  $Q_{ch,25^\circ\text{C}}$  denotes the ampere-hours charged at  $25\text{ }^\circ\text{C}$ .

It was decided not to incorporate this coefficient into the model. Facts supporting this decision are, for example, the computed  $\eta$  values. It was found that for the measured cells, the coulombic efficiency is very close to 100 % and thus neglecting it will not produce a significant error while effectively reducing the model complexity. Specific values computed from the measured data can be seen in Table 3.3.  $Q_{dch,T}$  denotes ampere-hours discharged at temperature  $T$ . A validation procedure, which further supports the neglect

$T$ [ $^\circ\text{C}$ ]	$Q_{dch}$ [Ah]	$Q_{dch,T}$ [Ah]	$Q_{ch,T}$ [Ah]	$\eta(T)$ [-]
-10	3.37	2.95	3.19	99.8
0	3.38	3.15	3.30	99.9
25	3.39	3.37	3.39	99.3
50	3.39	3.38	3.42	98.4

**Table 3.3:** Capacity and coulombic efficiency values of one cell with respect to temperature, computed from the measured data

of coulombic efficiency, is described in Section 6.2 of this thesis.

### 3.1.6 Full dynamic model

The entire dynamic cell model used in this thesis takes the following form:

$$u = \begin{bmatrix} I(t) \\ T_{air}(t) \end{bmatrix} \quad (3.15)$$

$$\dot{Q}_d(t) = I(t) \quad (3.16)$$

$$\dot{V}_1(t) = -\frac{V_1(t)}{R_1 C_1} + \frac{I(t)}{C_1} \quad (3.17)$$

$$\dot{V}_2(t) = -\frac{V_2(t)}{R_2 C_2} + \frac{I(t)}{C_2} \quad (3.18)$$

$$\dot{T}_{bat}(t) = \frac{R_0 \cdot I(t)^2}{C_{th}} + \frac{T_{air} - T_{bat}}{R_{th} C_{th}} \quad (3.19)$$

$$y = \begin{bmatrix} SOC \\ V_{trm} \\ T_{bat} \\ C \end{bmatrix} = \begin{bmatrix} 100 \cdot \left(1 - \frac{Q_d(t)}{C \cdot 3600}\right) \\ OCV - V_1(t) - V_2(t) - I(t) \cdot R_0 \\ T_{bat} \\ C_0 \cdot C_{rel} \end{bmatrix}, \quad (3.20)$$

where the meaning of the symbols is the same as for equations (3.1) to (3.5) or as described above. Together with the other parameters of the equivalent circuit model, Chapter 4 provides details on the identification and parameter dependencies.

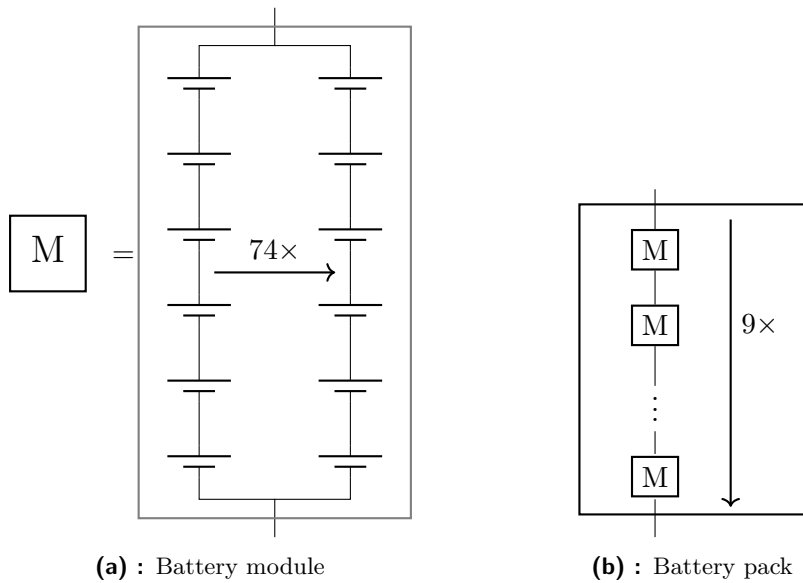


**Figure 3.2:** Schematic of the battery

## ■ 3.2 Battery Pack Modeling

Thus far, a single cell model has been considered. However, the battery used in an electric vehicle is composed of many similar cells. As previously stated in the introduction to this chapter, a cell model is usually developed first and later augmented to reflect the entire battery pack. This section describes the process of using the cell model to model the entire pack.

### ■ 3.2.1 Battery Pack Structure

For this thesis, it is aimed to model the battery pack in the demonstration vehicle. The demonstration vehicle uses battery modules from a Tesla Model S car. There are 9 such modules in the entire battery pack of the demonstration vehicle. All modules are connected in series. Each module comprises a total of 444 cells. [5] Each module is wired in such a way that groups of 6 cells connected in series are assembled in parallel. Thus forming 74 parallel connected groups. The module schematic is depicted in Figure 3.2a and schematic of the modules in a pack is illustrated in Figure 3.2b.

### ■ 3.2.2 Augmenting the Cell Model to the Whole Pack

This section is inspired by Chapter 2 of [22]. In general, it is necessary to model every cell individually. However, if some simplifying assumptions are met, a single cell model can be used to simulate the entire battery pack. The assumptions are

1. identical cell dynamics

2. equal initial conditions for all cells and
3. similar operating conditions.

The first two assumptions were taken from [22] while the third one was added.

Regarding the first point, every manufactured cell will have different dynamics. However, the measurements show that the differences in dynamics can be neglected. Figure 3.3 shows comparison of the measurements of the Urban Dynamometer Driving Schedule (UDDS) drive cycle measured at  $-10\text{ }^{\circ}\text{C}$ . Specifically, the last cycle is depicted, i.e., the cells are in a highly discharged state where highly nonlinear dynamics are expected. But even then, the measurements are very close.

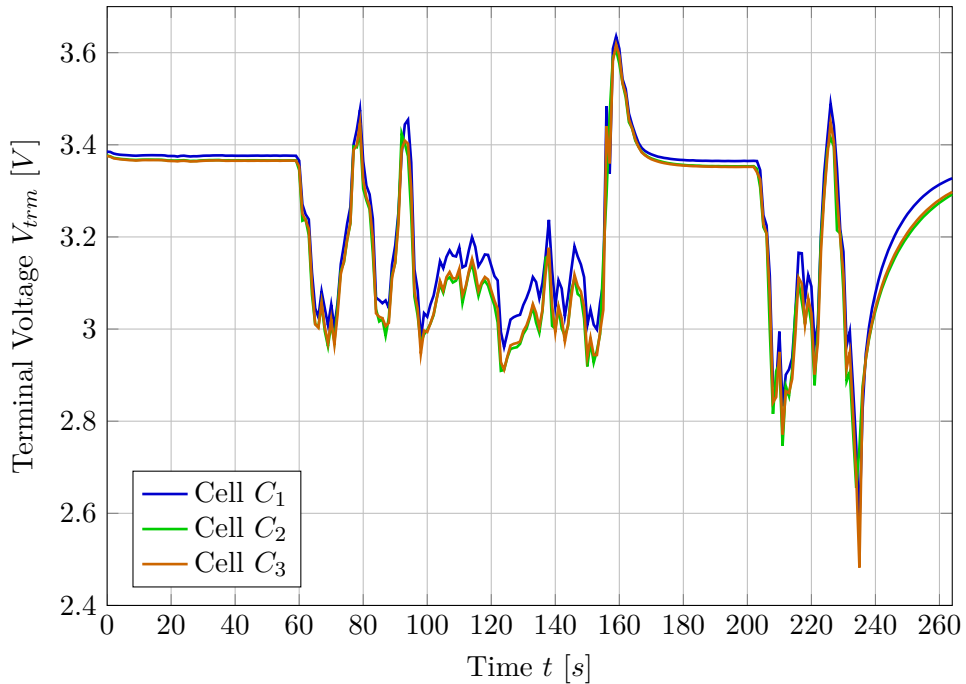


**Figure 3.3:** Comparison of drive cycle measurements of all 3 measured cells

Considering the second point, assuming similar initial conditions for a battery pack in a steady state is not a big simplification. However, one needs to ensure that the battery pack is truly in a steady state, the temperature distribution is homogeneous in the whole pack, and a cell balancing procedure takes place beforehand.

For the third point, one should consider that when using the battery in an environment where the difference between temperatures inside and outside of the battery pack is large, cells in the center of the battery pack might be warmer than those on the edges. Thus, there is a concern about the sufficiency of a single cell model in the case of extreme temperature conditions.

Although not all assumptions are perfectly satisfied, it is sufficient to accept them for this thesis. When these assumptions are accepted, it can be said that the input current is equal in all modules because they are connected in

series. Furthermore, the current is evenly divided into all parallel branches of each module because each parallel branch consists of the same number of cells connected in series. Furthermore, all series connected cells are exposed to a current of equal amplitude, and the temperature is evenly divided. By stating this, modeling the whole battery pack simplifies to dividing the input current by an appropriate factor and multiplying the output terminal voltage appropriately. The model's cell temperature is taken as the temperature inside the whole pack. The SOC state is treated similarly. Since there are 6 cells in series in each module, 74 parallel branches of cells in each module, and nine series connected modules in the pack (refer to Section 3.2.1 for more detail), this would mean that

$$\bar{I}(t) = \frac{I(t)}{74}, \quad (3.21)$$

$$\bar{T}_{air} = T_{air}, \quad (3.22)$$

$$SOC = \overline{SOC}, \quad (3.23)$$

$$V_{trm} = 6 \cdot 9 \cdot \bar{V}_{trm} = 54 \cdot \bar{V}_{trm}, \quad (3.24)$$

$$T_{pack} = \bar{T}_{bat}. \quad (3.25)$$

The overline symbols denote signals that come in or out of the cell model. The symbols without an overline denote the interface with the battery pack measurements.

### 3.3 Implementation in Matlab

The above described model was implemented in MATLAB in two variants. One without nominal capacity degradation and one with  $C_0$  as a state. (Refer to Chapter 5 for more details on capacity degradation modeling.) Both versions were implemented in the Energy Management Framework (EMF) of Garrett Motion as Matlab System objects with proper documentation. Both models are parametrized by the parameters described in Table 3.4.

Name	Symbol	Unit	Dimension	Dependency
Battery relative capacity	$C_{rel}$	-	1D	Temperature
Battery nominal capacity	$C_0$	Ah	1D	-
Internal resistance	$R_0$	$\Omega$	2D	Tmp., SOC
Open Circuit Voltage	$OCV$	V	2D	Tmp., SOC
$R_1$ resistance	$R_1$	$\Omega$	2D	Tmp., SOC
$R_2$ resistance	$R_2$	$\Omega$	2D	Tmp., SOC
$C_1$ capacitance	$C_1$	F	2D	Tmp., SOC
$C_2$ capacitance	$C_2$	F	2D	Tmp., SOC
Battery thermal resistance	$R_{th}$	K/W	Scalar	-
Battery thermal capacitance	$C_{th}$	J/K	Scalar	-

**Table 3.4:** Matlab model parameters

Both models implement look-up table input argument saturation, i.e., when a state reaches beyond the scope of a look-up table, the nearest value from the look-up table is chosen. This prevents runtime errors when simulating in extreme conditions. The interpolation of the look-up tables is set as linear. Because the models are implemented as Matlab System objects, they can be incorporated in Simulink schemes as regular blocks.

## 3.4 Conclusion of the Modeling Phase

Model selection and software implementation were described in this chapter. As a result, two new functional cell models in the Garrett Motion EMF are ready for use. Compared to the framework's original state, they are more adaptable with respect to temperature parametrization. The approach to pack modeling was simplified, and a validation procedure needs to be performed to test if this approach is sufficient in real operating conditions. This was not conducted during the work on this thesis because the demonstration vehicle was not fully assembled. In the case of larger pack model deviations, it is possible to include a cell junction resistance into the model by increasing the cell internal resistance  $R_0$  by an appropriate value.







## Chapter 4

### Model Identification

With the cell model being chosen, this section describes the process of identifying model parameters from the measured data. The procedure of each parameter estimation is described and encountered challenges are discussed.

#### 4.1 Cell Capacity

Cell capacity was determined from the slow discharge measurements described in Section 2.2. Discharged capacity was directly measured; therefore, this information was contained in the recorded data. The measurement was performed for temperatures  $-10\text{ }^{\circ}\text{C}$ ,  $0\text{ }^{\circ}\text{C}$ ,  $25\text{ }^{\circ}\text{C}$  and  $50\text{ }^{\circ}\text{C}$ . Results were already presented in Table 3.3. It can be seen that the total capacity differs very little with respect to temperature. On the other hand, the discharge capacity varies not negligibly. It can then be written that

$$C_{rel} = \frac{Q_{dch}}{C_0} = \frac{Q_{dch}}{Q_{dch,25^{\circ}\text{C}}}. \quad (4.1)$$

For this thesis, the total capacity was used instead of available discharge capacity.<sup>1</sup> If it is needed to provide the user with the state of charge (SOC) related to the available discharge capacity, it can be easily computed using the available data. Both the total and available discharge capacity values are available in the identified data. They are in the form of a lookup table that is dependent on temperature.

#### 4.2 Open-circuit Voltage

For the open circuit voltage (OCV) identification, the same measurement data were used as for the capacity identification (i.e. those described in Section 2.2). Because discharged capacity was directly measured during the scenarios, extracting SOC-OCV relationships was straightforward. The measured voltages are depicted in Figures 4.1, 4.2, 4.3 and 4.4 as curves “Charge OCV” and “Discharge OCV”.

---

<sup>1</sup>Difference between total and available capacity is explained in Section 3.1.2.

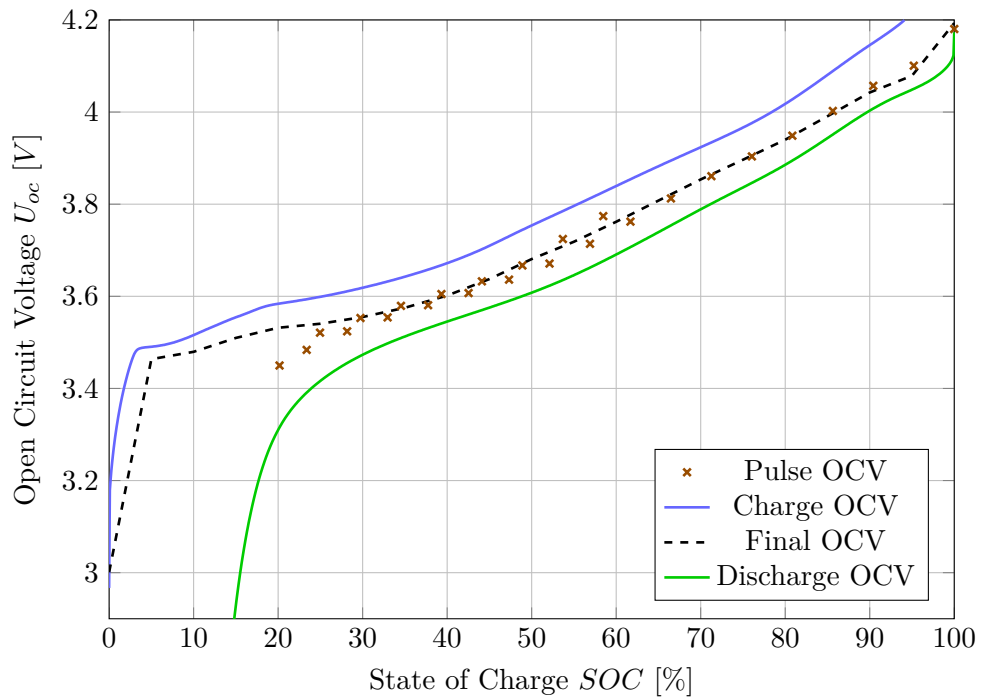


**Figure 4.1:** Transfer characteristic between the open-circuit voltage and the state of charge of one cell at  $-10\text{ }^{\circ}\text{C}$ . Comparison of charge, discharge and final characteristic.

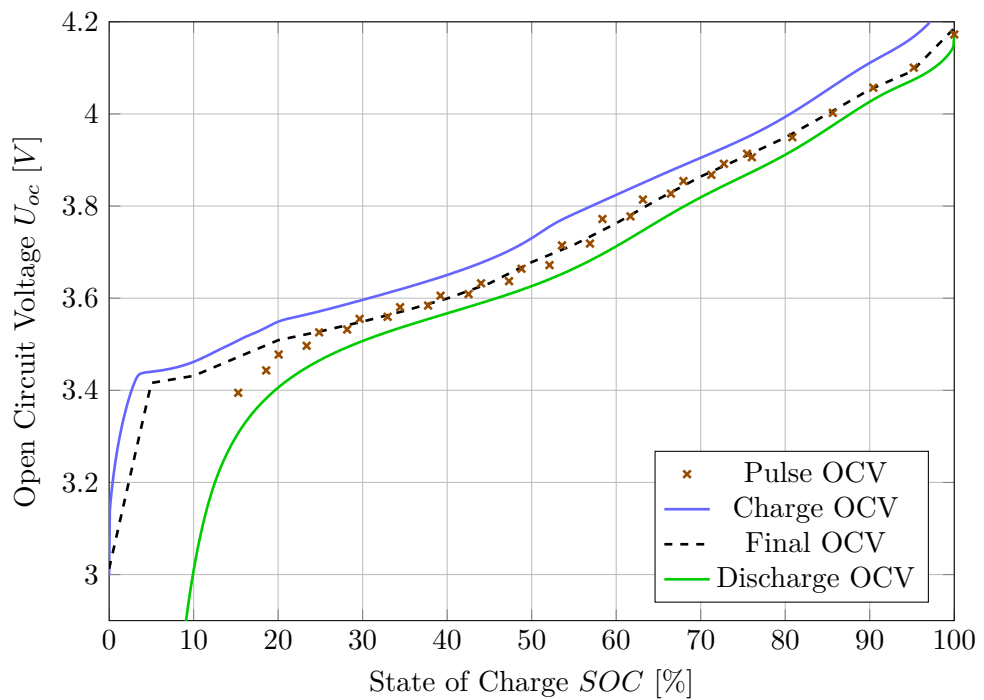


**Figure 4.2:** Transfer characteristic between the open-circuit voltage and the state of charge of one cell at  $0\text{ }^{\circ}\text{C}$ . Comparison of charge, discharge and final characteristic.

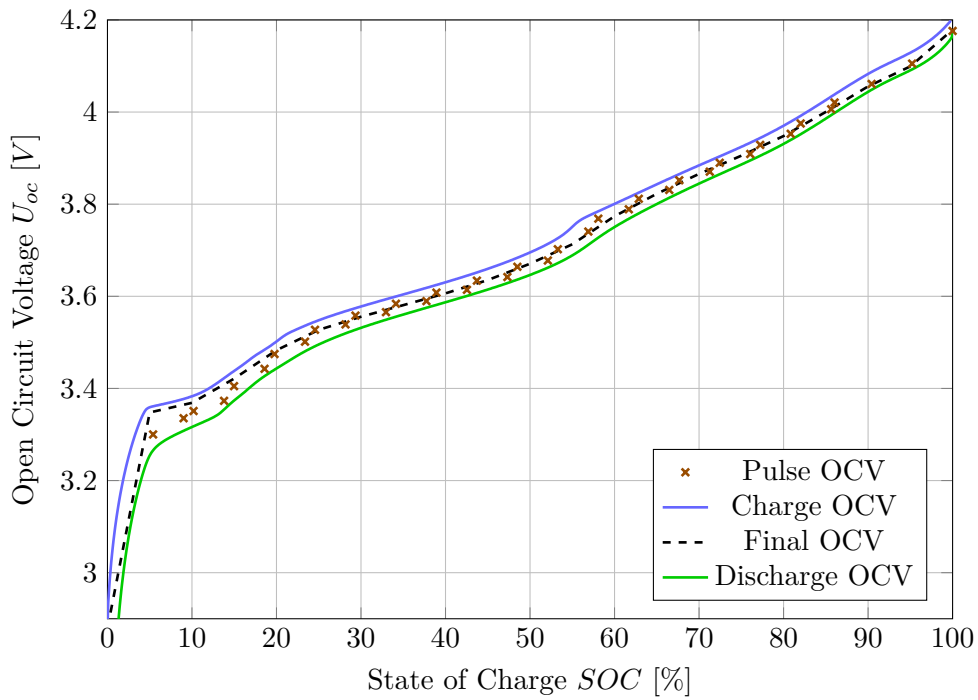


**Figure 4.3:** Transfer characteristic between the open-circuit voltage and the state of charge of one cell at 25 °C. Comparison of charge, discharge and final characteristic.

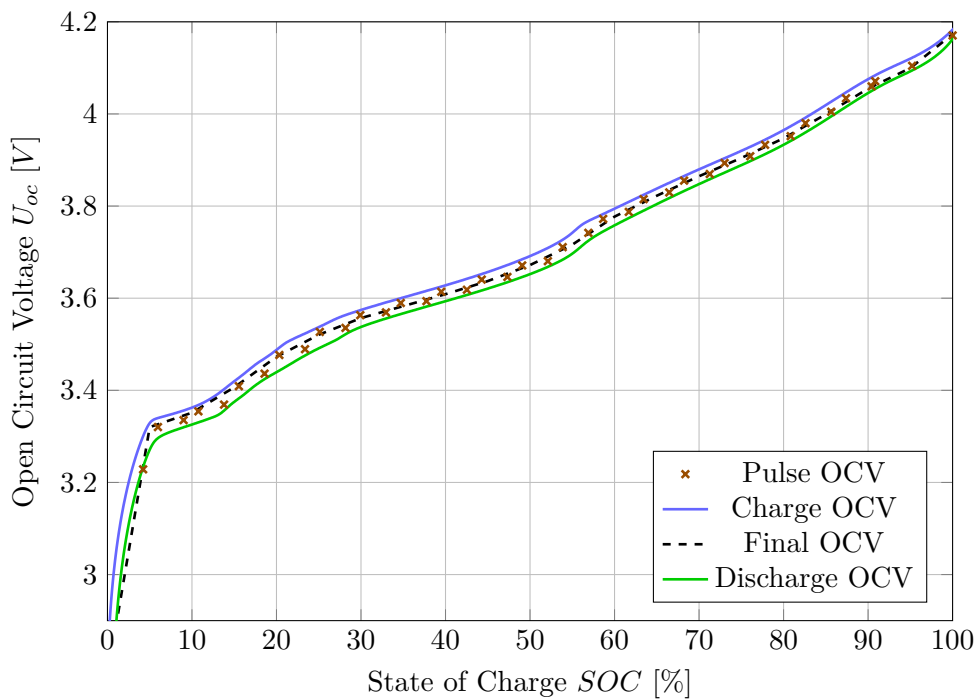


**Figure 4.4:** Transfer characteristic between the open-circuit voltage and the state of charge of one cell at 50 °C. Comparison of charge, discharge and final characteristic.

However, it can be seen that the curves obtained by charging and discharging differ, mainly at low temperatures. This can be attributed to internal resistance and hysteresis. [21]

In [21], the author suggests using the following procedure to extract the final OCV characteristic. Because so far only the cell capacity has been identified, it is necessary to estimate the cell's internal resistance  $R_0$ . It can be done at 100 % SOC and 0 % SOC by processing the immediate voltage drops at the start of charge and discharge cycles. The  $R_0$  value at 50 % SOC is approximated by the difference between the charge and discharge voltage curves at that particular SOC state. By this method, 3 sample values are obtained  $R_{0,100\%}$ ,  $R_{0,50\%}$  and  $R_{0,0\%}$ . Furthermore, it is suggested to suppose that the internal resistance varies linearly between these sample points. The final OCV curve is then obtained at two stages.

First, the discharge curve is taken in the range 100 % - 50 % and it is summed up with a value of

$$U_{add} = R_0(SOC) \cdot I, \quad (4.2)$$

where  $R_0(SOC)$  is a value linearly interpolated between  $R_{0,100\%}$  and  $R_{0,50\%}$ . Current  $I$  is the discharge current applied to the cell. So for 100 % - 50 % SOC range, the following equation is applied:

$$U_{final,100-50} = U_{dchg} + U_{add}, \quad (4.3)$$

where  $U_{dchg}$  is the measured discharge curve.

Second, the charge curve in the range 50 % - 0 % SOC it taken and from this a value

$$U_{sub} = R_0(SOC) \cdot I \quad (4.4)$$

is subtracted.  $R_0(SOC)$  is a value linearly interpolated between  $R_{0,50\%}$  and  $R_{0,0\%}$ . Current  $I$  is the charge current applied to the cell. So for 50 % - 0 % SOC range, the following equation is applied:

$$U_{final,50-0} = U_{chg} - U_{sub}, \quad (4.5)$$

where  $U_{chg}$  is the measured charge curve.

The final OCV characteristics obtained by this method are depicted in the above mentioned Figures 4.1, 4.2, 4.3 and 4.4. All of the final OCV characteristics are shown together in Figure 4.5. It can be observed that the final OCV curves do not differ very much with respect to temperature as far as the SOC range 20 % to 100 % is concerned. The main difference is evident in SOC values lower than 20 %. As stated in Section 3.3, the SOC-OCV relationship is represented by a look-up table that depends on both temperature and SOC.

#### 4.2.1 Comparison with Pulse Data

For comparison, the OCV voltages obtained from pulse measurements (Section 2.3) were also plotted in the above-mentioned figures. These values were

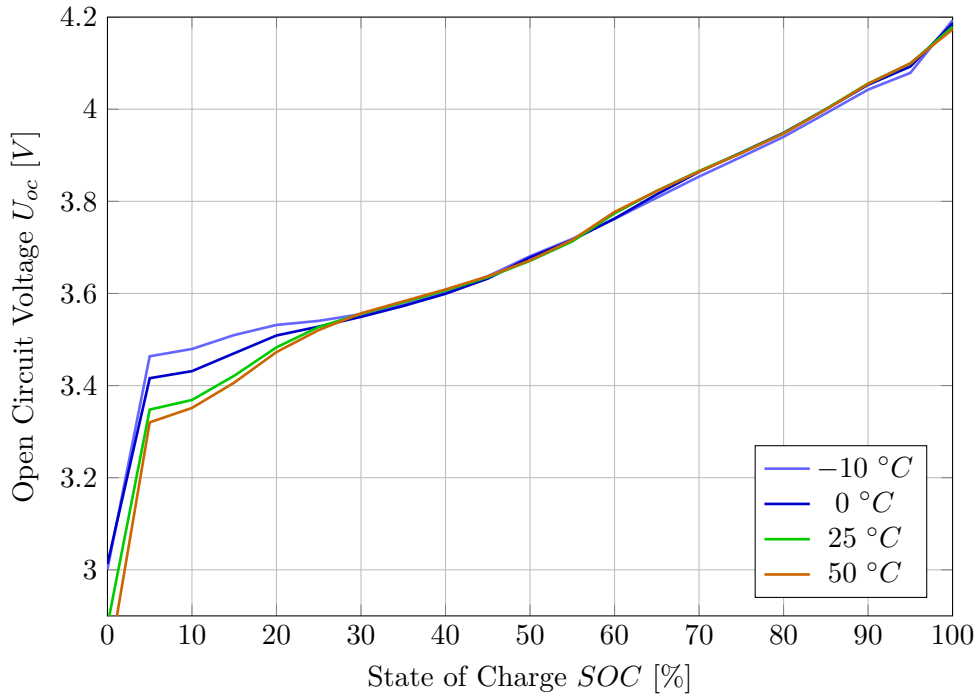


**Figure 4.5:** Transfer characteristics between the open circuit voltage and the state of charge of one cell for different temperatures

obtained as terminal voltages before each pulse, i.e., after the battery reached a steady state; thus, it can be assumed that the transients had already faded out and the terminal voltages corresponded to the open circuit voltage.

It can be seen that the pulse data correspond well with the final computed OCV curves in the SOC range  $\geq 25\%$ . However, the pulse data diverge from the final OCV curve, especially for low temperatures when approaching 0% SOC. This leads to doubts about the accuracy of the above procedure. The topic of inaccurate model identification at low SOC values is revisited in Section 4.4, where the estimation of the resistor-capacitor (RC) couple values is described.

## 4.3 Internal Resistance

### 4.3.1 Extracting Values from the Data

Article [2] provides a technique for identifying cell internal resistance. Specifically, it is stated in [2] that the pulse measurement data (described in Section 2.3) can be used. There is a visible voltage drop at the start of each pulse. This voltage drop is attributed to the static internal resistance  $R_0$  (an illustration is shown in Figure 4.6). Thus, by considering the magnitude of the current pulse, the value of  $R_0$  at the given SOC and temperature can be computed.

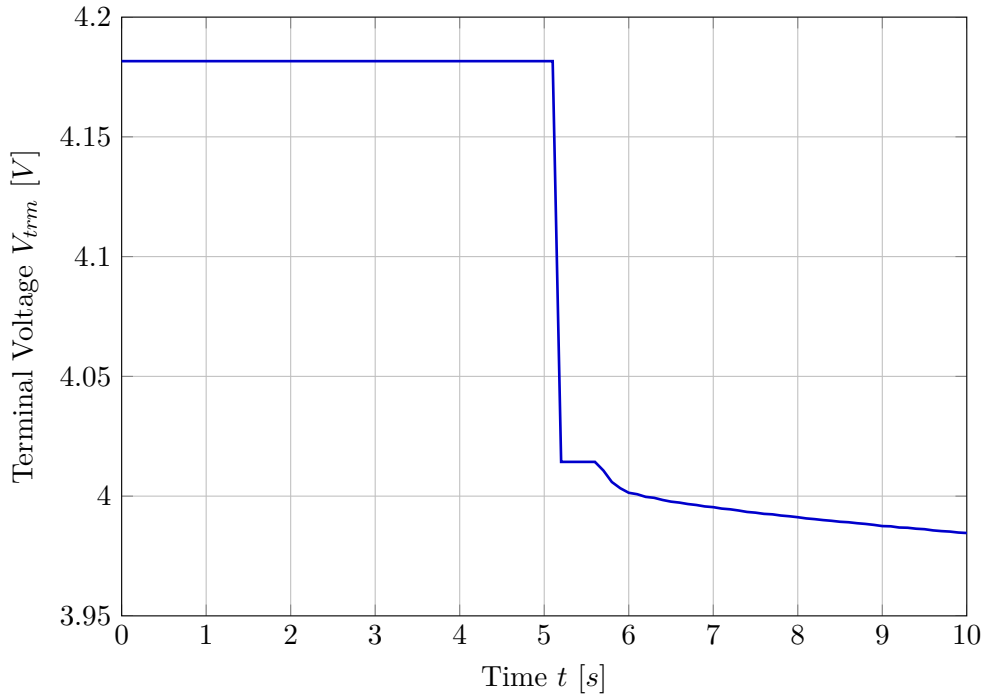


**Figure 4.6:** Demonstration of an immediate terminal voltage drop at the start of a current pulse

### 4.3.2 Considering Dependence on the C-rate

As it was mentioned in [33], dependency of  $R_0$  on the C-rate is a recorded phenomenon. Furthermore, this dependency changes with the cell age. Graphs documenting this dependency can be seen in Figures 4.7 and 4.8. It was investigated whether this behavior is also present in the cells used for this thesis. Different amplitudes of the current pulses were measured. Specifically, pulses of amplitudes  $0.5C$ ,  $1C$ , and  $1.5C$  were recorded. Since the minimal guaranteed capacity of the Panasonic NCR18650B cells is  $3250 \text{ mAh}$  [20], the corresponding current amplitudes are  $1.625 \text{ A}$  for  $0.5C$ ,  $3.25 \text{ A}$  for  $1C$ , and  $4.875 \text{ A}$  for  $1.5C$ . When the internal resistances were extracted, it was found that C-rate dependence was not evident. The result can be seen in Figure 4.9. This might be caused by low values of current amplitudes while performing the measurements, because data with  $40\times$  larger x-axis scale are presented in Figures 4.7 and 4.8. This range is much higher than the one in Figure 4.9. Nevertheless, the C-rate dependence of  $R_0$  was eventually not considered in model identification.

### 4.3.3 Measured Data Fitting

When plotting the measured data on an  $R_0$ -SOC axis for individual temperatures, it was noticed that the internal resistance measurements were similar to a basin shape. Thus a  $2^{nd}$  and  $4^{th}$  order polynomial fitting functions were tested. It turned out that they fit the measured data reasonably well. The



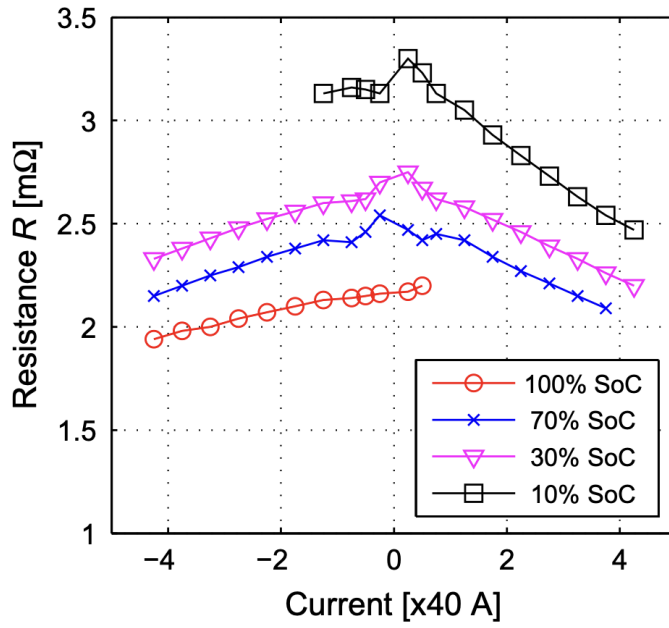


Figure 4.7:  $R_0$  dependence on C-rate for different SOC values, new cell [33]

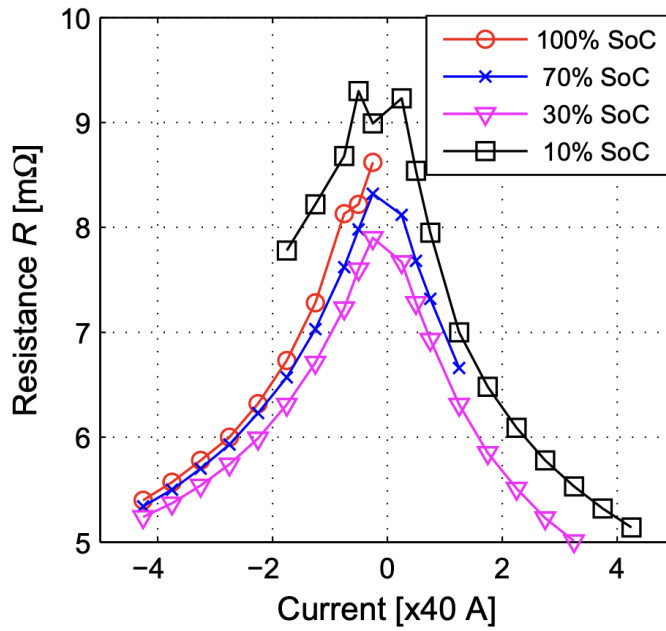
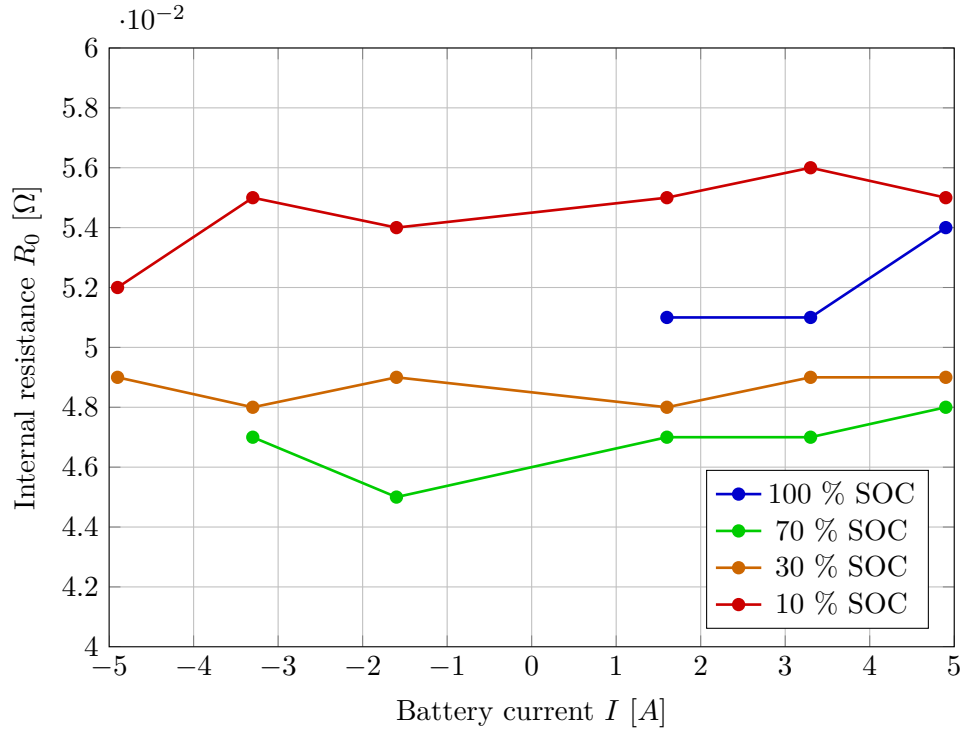


Figure 4.8:  $R_0$  dependence on C-rate for different SOC values, aged cell [33]



**Figure 4.9:** Measured  $R_0$  dependence on C-rate for different SOC values

fitting polynomial is described by the following formula.

$$f(x) = \sum_{i=1}^{n+1} p_i x^{n+1-i} \quad (4.6)$$

The polynomial is used to derive  $R_0$ -SOC dependence from the data. Later, polynomial values are used to create the  $R_0$  look-up table. The fitted polynomial coefficients are presented in Table 4.1. A comparison of measured data and fitted polynomials for individual temperatures is shown in Figures 4.10, 4.11, 4.12 and 4.13. Figure 4.14 shows all the fitted polynomials for all measured temperatures along one axis. It can be seen that internal resistance decreases with increasing temperature. Look-up table data were extracted from the fitted polynomials for cell model simulation.

Coefficient	$-10\text{ }^\circ\text{C}$	$0\text{ }^\circ\text{C}$	$25\text{ }^\circ\text{C}$	$50\text{ }^\circ\text{C}$
$p_1$	3.4e-09	3.5e-06	2.6e-06	7.4e-10
$p_2$	-7.1e-07	-4.0e-04	-3.4e-04	-1.7e-07
$p_3$	5.4e-05	8.9e-02	5.7e-02	1.5e-05
$p_4$	-1.9e-03	-	-	-6.0e-04
$p_5$	1.4e-01	-	-	4.8e-02

**Table 4.1:** Coefficients values of fitting polynomial for the transfer function of the internal resistance for different temperatures.

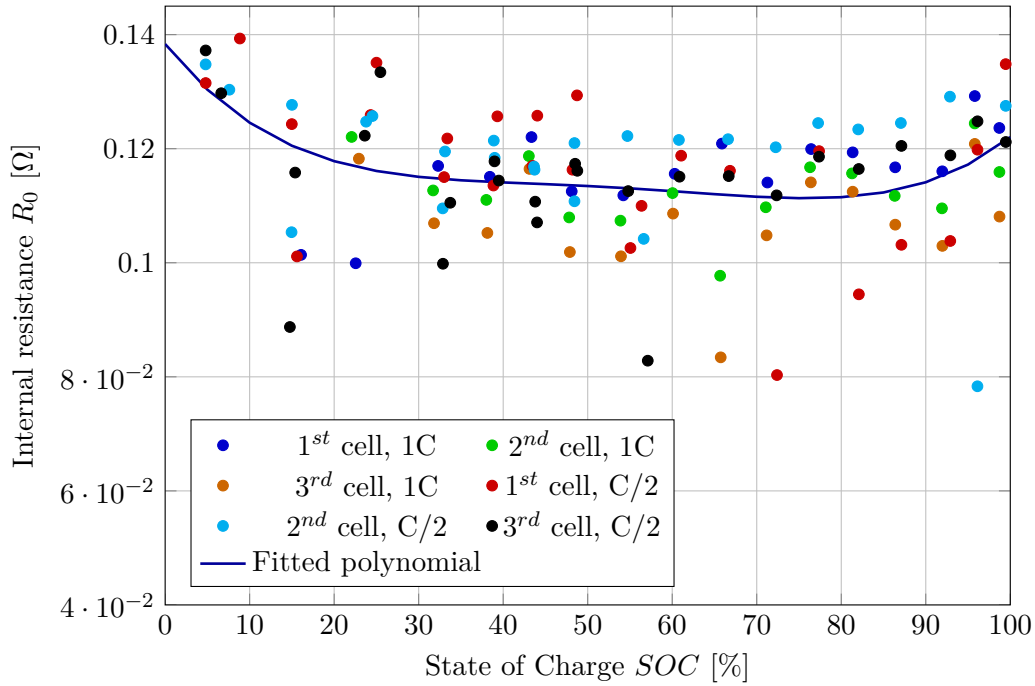


**Figure 4.10:** Comparison of measured and fitted characteristic of internal resistance at  $-10\text{ }^\circ\text{C}$

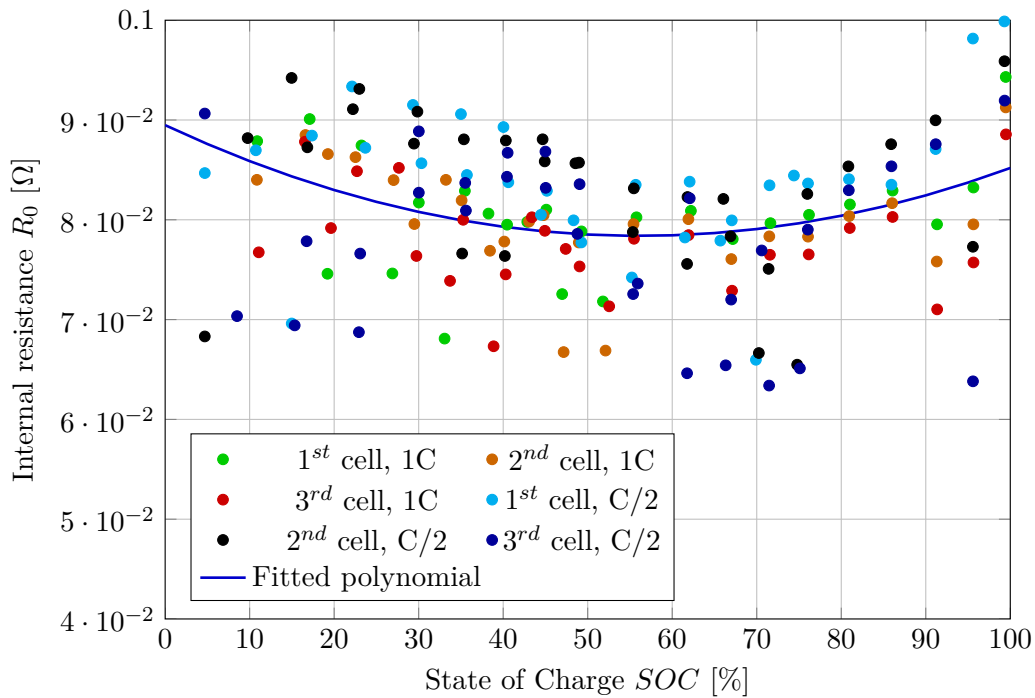


**Figure 4.11:** Comparison of measured and fitted characteristic of internal resistance at  $0\text{ }^\circ\text{C}$

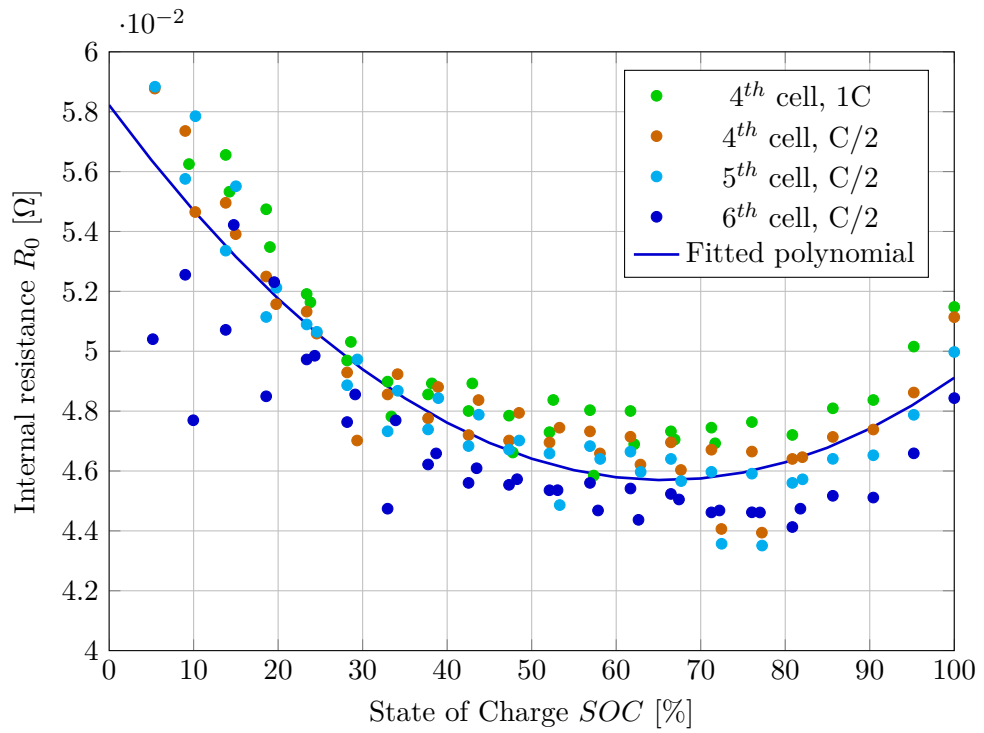


**Figure 4.12:** Comparison of measured and fitted characteristic of internal resistance at 25 °C

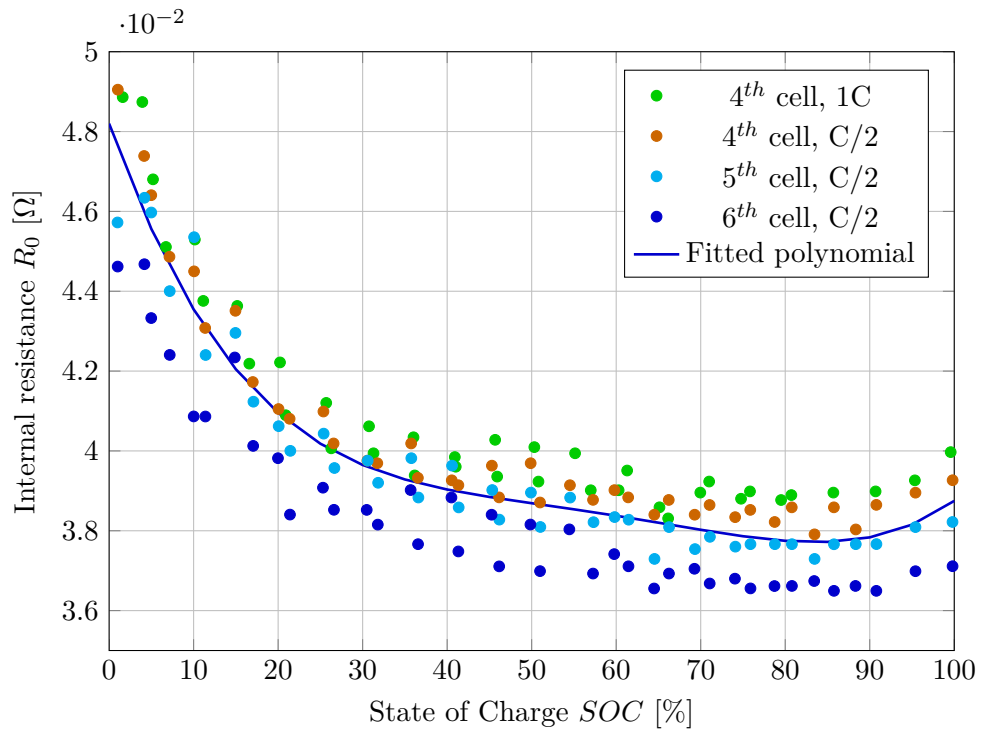


**Figure 4.13:** Comparison of measured and fitted characteristic of internal resistance at 50 °C

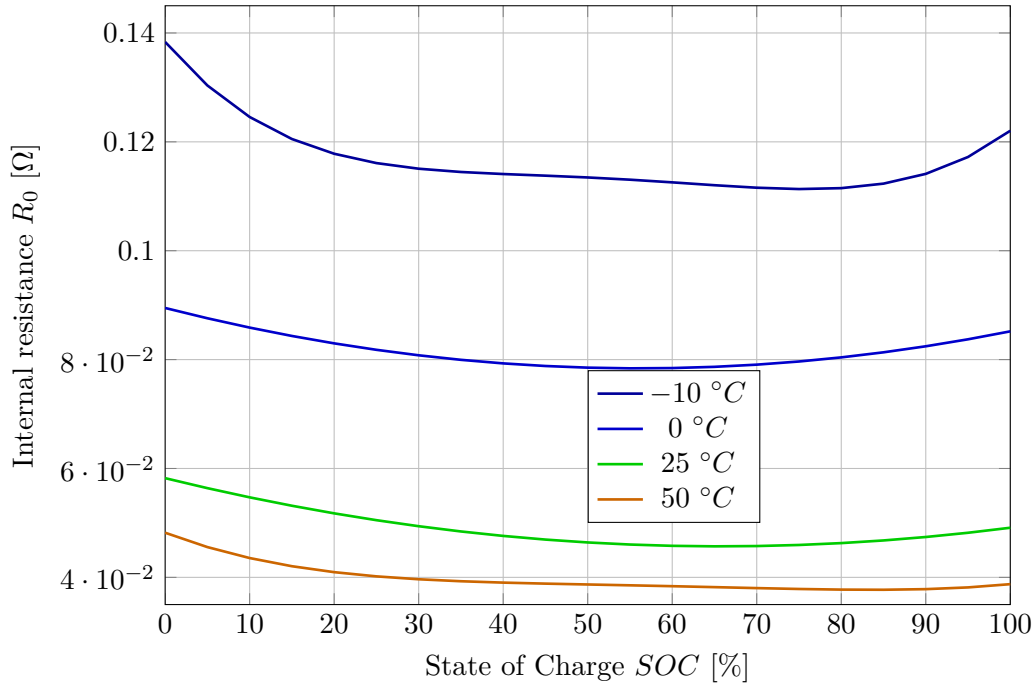


**Figure 4.14:** Transfer characteristics between the cell's internal resistance and the state of charge at different temperatures, and final fitted polynomials

## 4.4 RC Couples

### 4.4.1 Identification Method

Identifying the values of  $R_1$ ,  $C_1$ ,  $R_2$ , and  $C_2$  (RC) parameters was done according to [2] using the pulse data measurements (Section 2.3). While for capacity, OCV, and  $R_0$  identification, it was possible to develop fully automated scripts that extract the values from the measurements, it was not fully done for the RC parameters. The reason is that it is needed first to find the point where it is considered that the first RC pair reached a steady state and the second RC pair effect becomes dominant. Such a possible point (later denoted as the *middle* point) is depicted in Figure 4.15 as a red circle. On the other hand, an automatic script that identified the *start* and *end* points of the transition period (green circles in Figure 4.15), was programmed.

These points served as an initial guess for computing the RC values. Note that the computed values were assigned to a particular temperature and SOC based on the pulse processed. The  $R_1$  value was computed using the formula

$$R_1 = \frac{V_{start} - V_{middle}}{I}, \quad (4.7)$$

where  $I$  is the amplitude of the current pulse,  $V_{start}$  and  $V_{middle}$  correspond to the terminal voltage values at the start and middle points. The  $C_1$  value

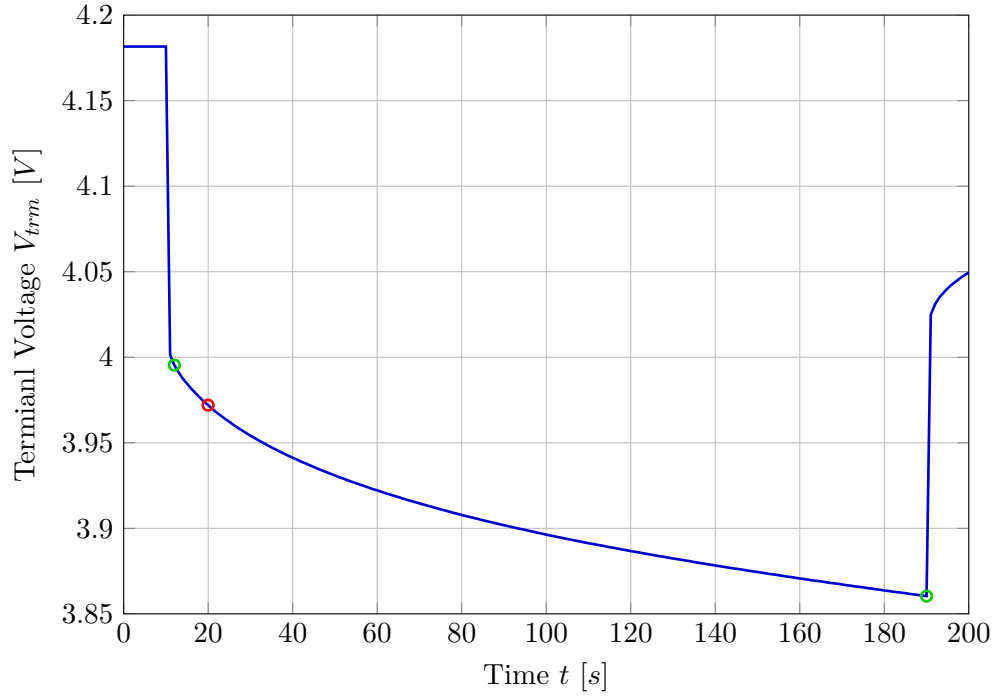


**Figure 4.15:** Demonstration of the border point (red) when effect of the 2<sup>nd</sup> RC pair starts to dominate the 1<sup>st</sup> RC pair. The green points indicate the start and end of the transition period

was computed using the fact that the time constant equation is  $\tau = R \cdot C$ . This leads to the formulas

$$C_1 = \frac{\tau}{R_1}, \quad (4.8)$$

$$\tau = \frac{t_{middle} - t_{start}}{3}, \quad (4.9)$$

where  $t_{start}$  and  $t_{middle}$  correspond to the times when the start and middle points were identified. The fact that a step response of a first-order system reaches 95 % of the steady-state value after time  $t = 3 \cdot \tau$  was used. Similarly,  $R_2$  and  $C_2$  were computed using the following formulas

$$R_2 = \frac{V_{middle} - V_{end}}{I}, \quad (4.10)$$

$$C_2 = \frac{\tau}{R_2}, \quad (4.11)$$

$$\tau = \frac{t_{end} - t_{middle}}{3}, \quad (4.12)$$

where  $V_{end}$  and  $t_{end}$  correspond to the terminal voltage and time value of the end point.

After obtaining the initial guesses, a rough manual tuning was conducted: measurements of all 3 cells were compared with a response generated by a cell model (3.15)-(3.20) and the RC values were adjusted by a trial-and-error

approach. After manual tuning was performed, fine tuning was performed using an automated optimal identification Matlab tool provided by the Garrett Motion company.

#### 4.4.2 Limitations of the Method Used

Before stating the actual limitations, the definitions of terms “active” and “passive” part of the current pulse must be provided. The terms “active” and “passive” part of a pulse simply distinguish between the part where the current pulse is applied and the part where the battery returns to the steady state. This is illustrated in Figure 4.16, where the “active” side is on the left of the black dashed line. This applies when we consider discharge pulses. For the charge pulses, the “active” part would be the one where the terminal voltage rises and the “passive” part would be the one where the terminal voltage decreases.

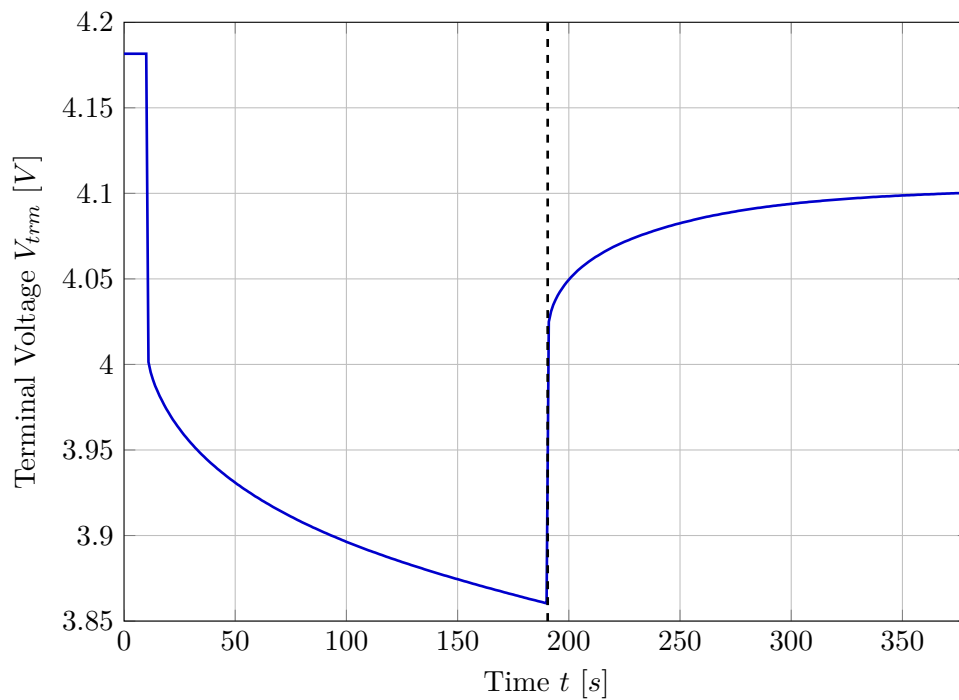


**Figure 4.16:** Explanation of the terms “active” and “passive” part of the current pulse

Regarding the actual limitations, note that identification was performed only on the “active” part of each pulse. The dynamics of the cell returning to the rested state after the pulse ends was not considered in deriving RC parameter values. This decision was based on the fact that, due to cell’s nonlinearity, the “passive” part has different dynamic properties than the “active” one. This is demonstrated in Figure 4.17. Identifying both parts at the same time would lead to poor match for both parts; therefore, only the “active” part was chosen as a reference. Adding a hysteresis to the cell

equations (3.15)-(3.20) might solve this issue. However, since the hysteresis is not modeled, the aforementioned approach was selected.

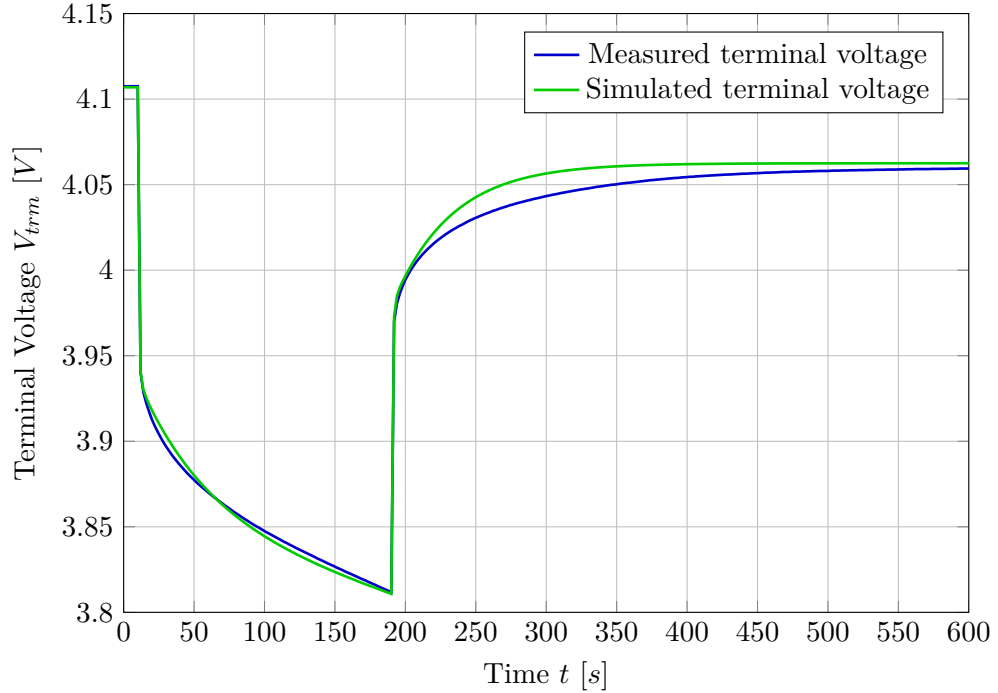


**Figure 4.17:** Demonstration of different dynamics for the active and passive part of a pulse

#### 4.4.3 Identification at Low SOC Values

Particularly difficult was identifying RC values for low SOC ranges (e.g., below 20 %). Figure 4.18 demonstrates a response to the last discharge current pulse of  $1C$  amplitude measured at  $25\text{ }^{\circ}\text{C}$ . The measured terminal voltage in the “active” part of the pulse exhibits a concave shape rather than the usual convex one. As mentioned before in Section 4.2, which deals with OCV estimation, there are doubts about the accuracy of the computed OCV values in the low SOC range.

One possibility that could explain the mismatch of simulation data at low SOC values, is that the identified SOC-OCV relationship is not accurate enough in that range. As mentioned earlier in Section 4.2, this is suspected partly because of the different results of the estimated OCV values compared with the pulse measurements. However, it can be seen that for the temperature  $25\text{ }^{\circ}\text{C}$  the OCV measurements correspond well. However, as depicted in Figure 4.18, the simulated and measured curves differ excessively.

It can be stated that the problem is not caused by the wrong values of the RC elements because the RC elements cannot produce a concave shape response. Eventually, the cause of this inaccuracy was not identified and can be attributed to the unmodelled behavior of the cell. However, the usual



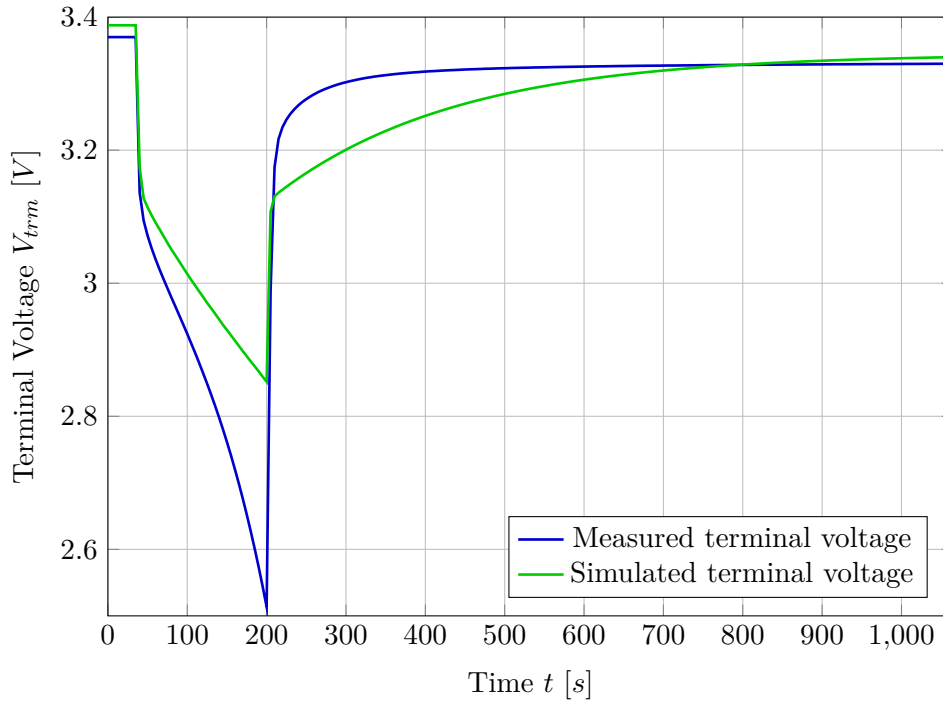


**Figure 4.18:** Demonstration of poor fitting at low SOC values, excerpt from measurement taken at 25 °C

operating range of Li-ion cells is between 80 % and 20 % SOC. This means that the model identification inaccuracy below 20 % SOC can be neglected.

#### 4.4.4 Final RC Estimation Results

The final identified values of  $R_1$ ,  $C_1$ ,  $R_2$ , and  $C_2$  parameters are showed in Figures 4.19, 4.20, 4.21 and 4.22. It can be observed that some dependencies are flat at low SOC values (e.g.  $R_1$  values at  $SOC \leq 30\%$ ,  $-10\text{ }^\circ\text{C}$ ). This is caused by a lack of measurement data. As mentioned, identification of these parameters was performed from pulse data. Especially at low temperatures, it happened that the low threshold voltage was hit soon, i.e., the pulse that started at e.g. 30 % SOC caused the terminal voltage to hit the threshold. This caused the discharging phase to stop and the charging phase to start, and thus only values down to 30 % SOC were obtained. Such a situation was handled by extrapolating the characteristic using the last measured value. Thus, a flat characteristic is produced. When the shape of the characteristic allowed this, the values were extrapolated in such a way as to follow the characteristic shape. Simulation verification was then conducted to test the performance of the model at low SOC values is acceptable.

Some of the characteristics appear chaotic and no specific curve can be fitted. Similar results are published in [9] or [14]. The author of [9] states that the shape of the characteristic of  $C_1$  is jagged and that “The reason for this behavior is not clear at this moment.” A possible explanation could be

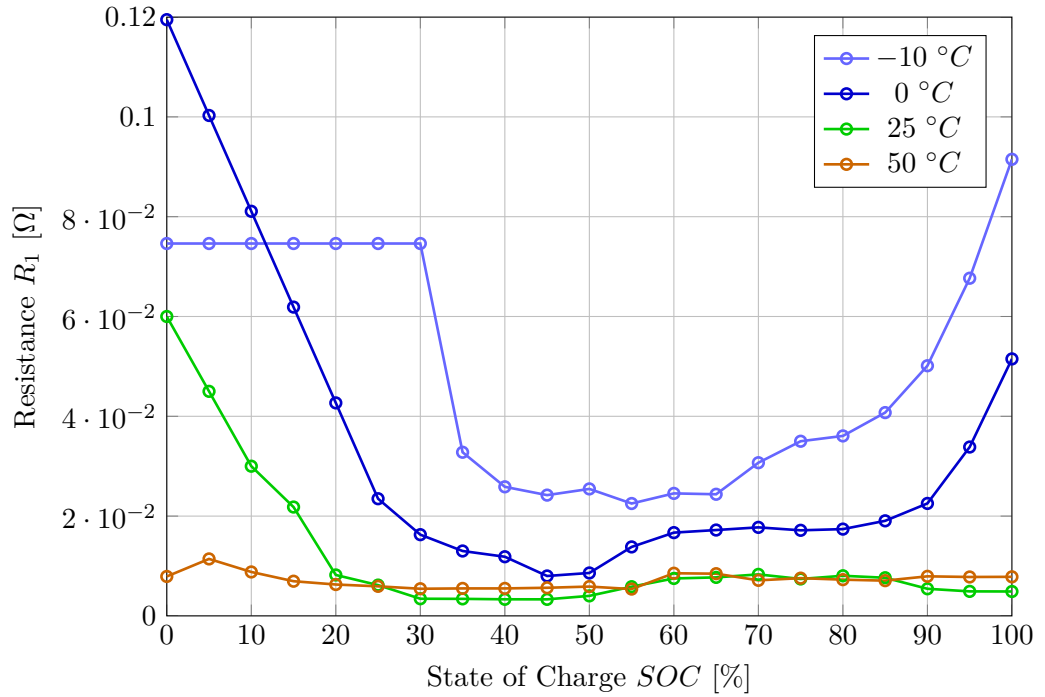


Figure 4.19: Final values of  $R_1$  parameter

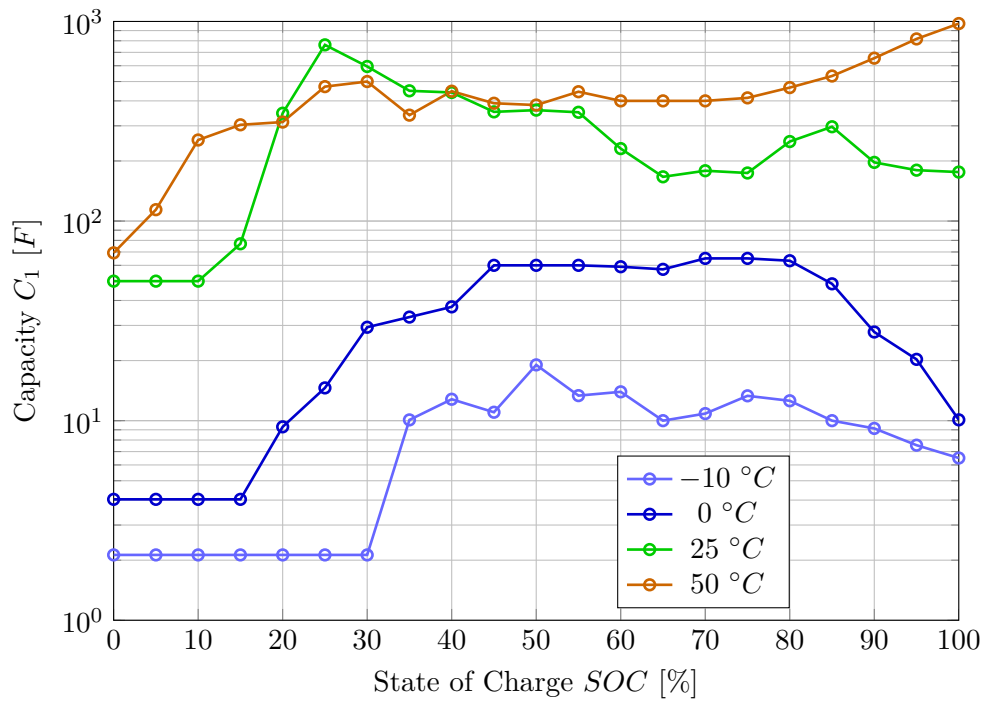


Figure 4.20: Final values of  $C_1$  parameter

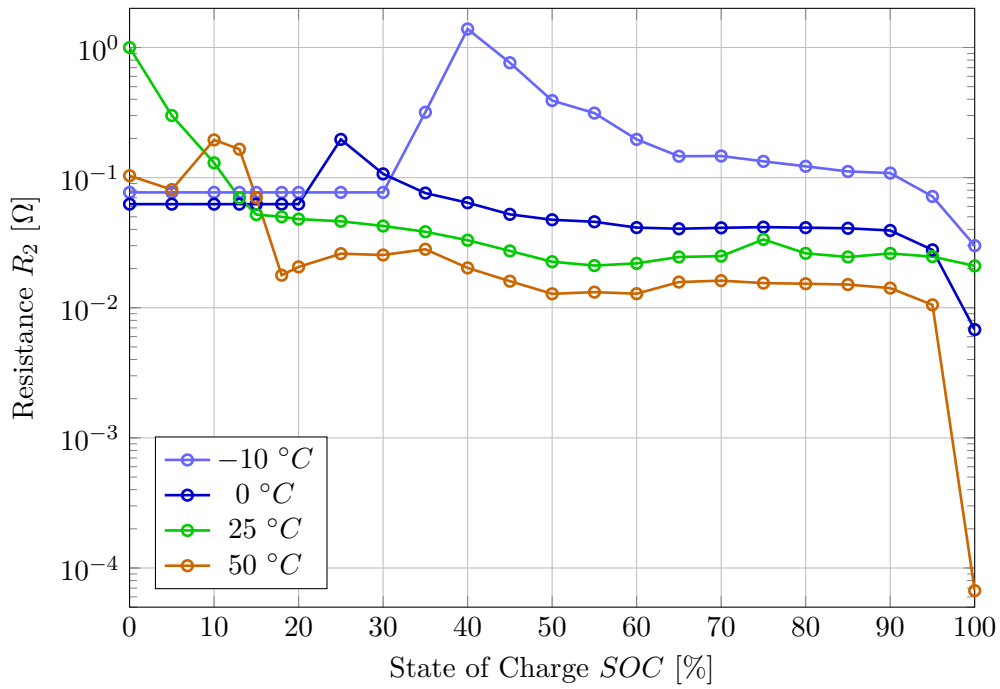


Figure 4.21: Final values of  $R_2$  parameter

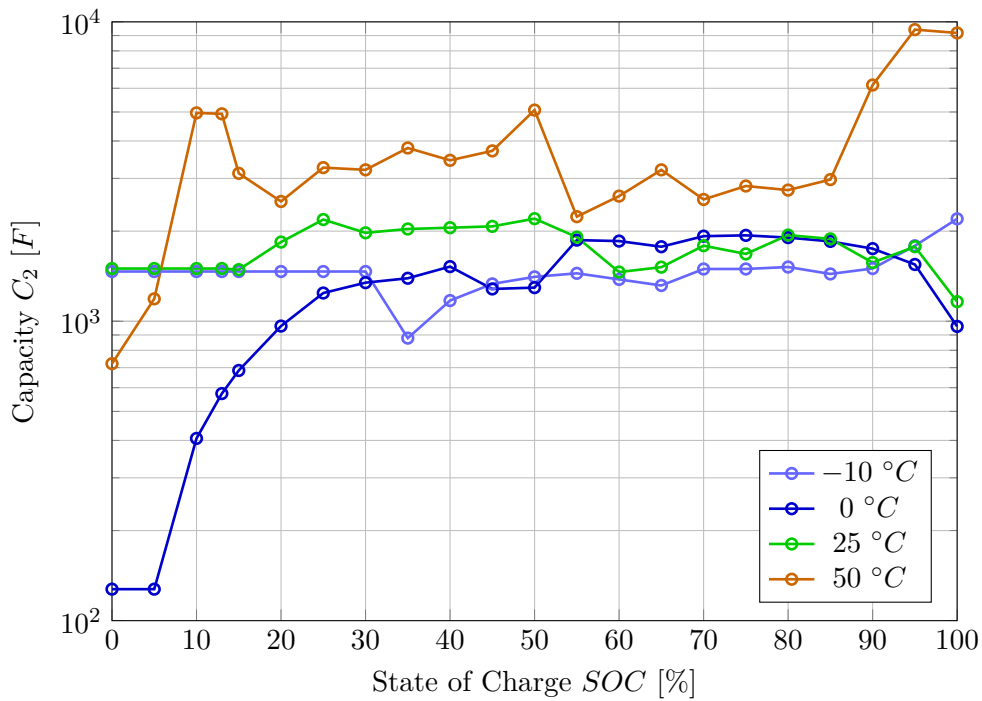


Figure 4.22: Final values of  $C_2$  parameter

that the equivalent circuit model (ECM) is just a representation of outer cell's behavior. Thus, since the ECM schematic parts do not correspond to all electrochemical phenomena that occur in the cell, but are just approximations; the measured characteristics do not need to exhibit any specific shape. If a more precise ECM is used (e.g. an ECM containing the Warburg impedance [21]), the resulting characteristics could exhibit less chaotic shapes.

It can be seen from the measured characteristics that temperature dependence is evident. This observation supports the fact that the values  $R_1$ ,  $C_1$ ,  $R_2$ , and  $C_2$  are represented by a lookup table with SOC and temperature as input parameters.

## 4.5 Thermal Dynamics

Identification of the temperature dynamics must be performed with data measured from the real battery pack to reflect the pack-specific conditions. The provided measurements were performed only on a single cell that was placed in a thermal chamber. Because the demonstration vehicle was not ready, thermal dynamics measurements were not conducted. Thus thermal dynamics, parametrized by the thermal resistance  $R_{th}$  and thermal capacitance  $C_{th}$ , was left unidentified and the values were guessed.

## 4.6 Comparison of the Identified Model and Measured Data

The cell model is compared with measured data. For this purpose, driving profile datasets, which are described in Section 2.4, were used. The input current and ambient temperature signals were taken as the cell model input, and the measured terminal voltage and model terminal voltage were compared. For this validation, a cell model without nominal capacity  $C_0$  as a state was considered. I.e. equations described in Section 3.1.6 were considered. Figures 4.23, 4.24, 4.25 and 4.26 depict comparison between the terminal voltage generated by the cell model and the measured data.

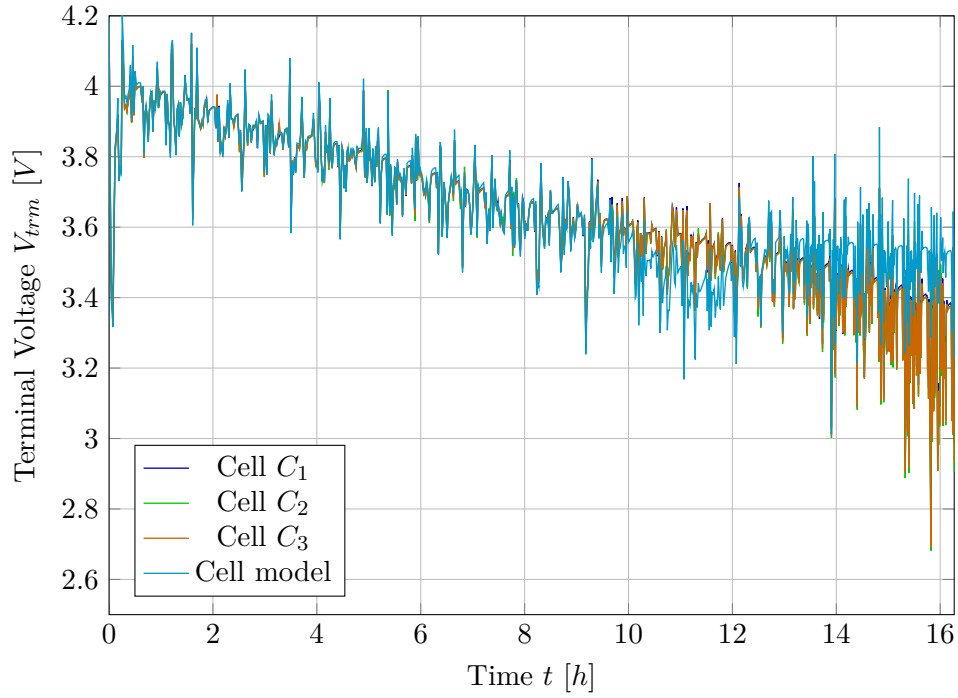


**Figure 4.23:** Validation of a cell model using UDDS data,  $-10\text{ }^{\circ}\text{C}$

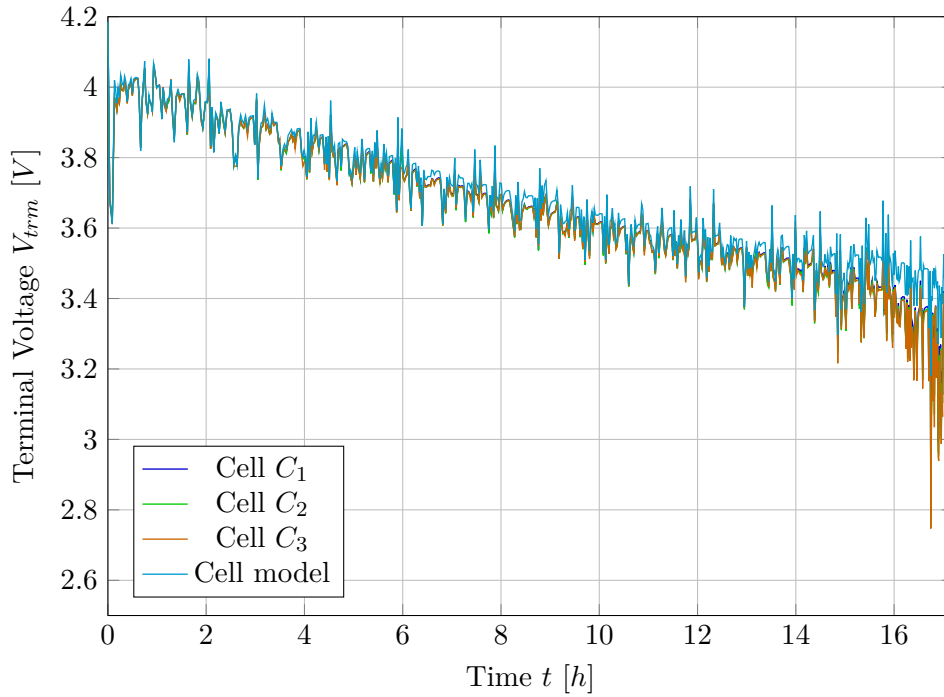


**Figure 4.24:** Validation of a cell model using UDDS data,  $0\text{ }^{\circ}\text{C}$

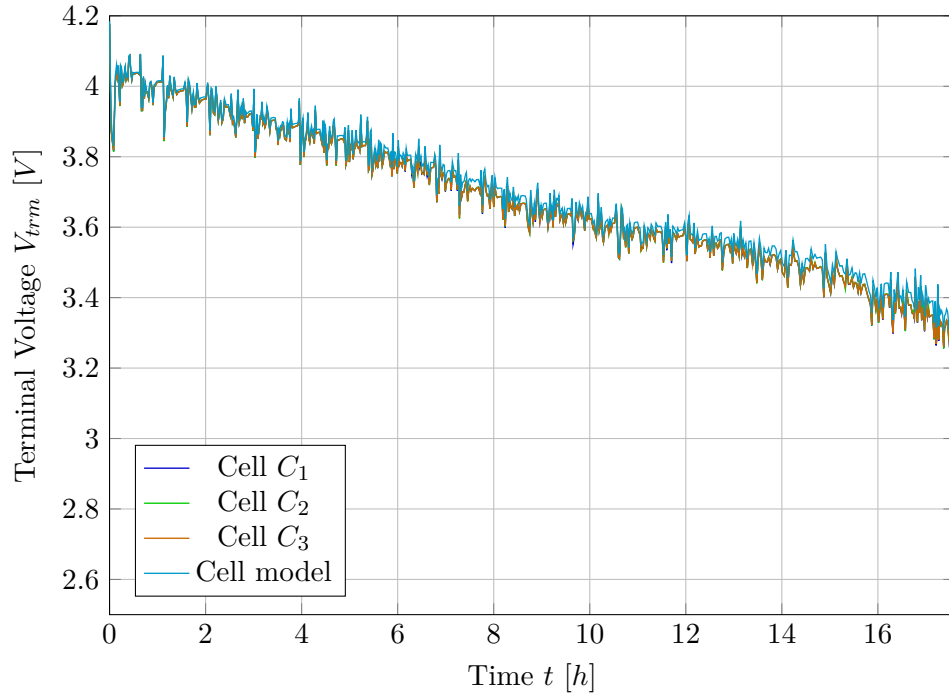


**Figure 4.25:** Validation of a cell model using UDDS data, 25 °C

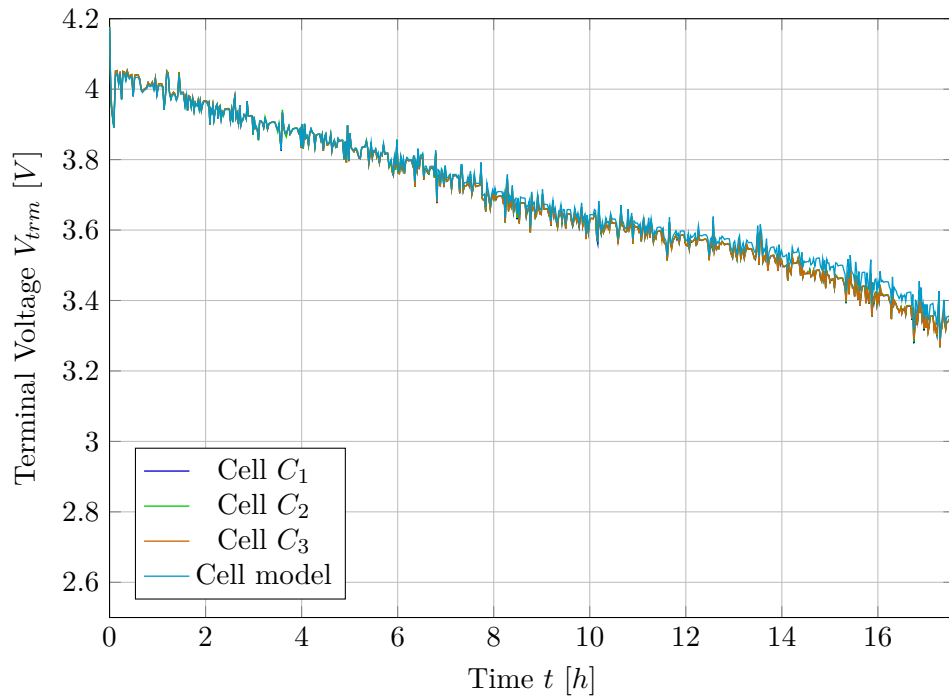


**Figure 4.26:** Validation of a cell model using UDDS data, 50 °C

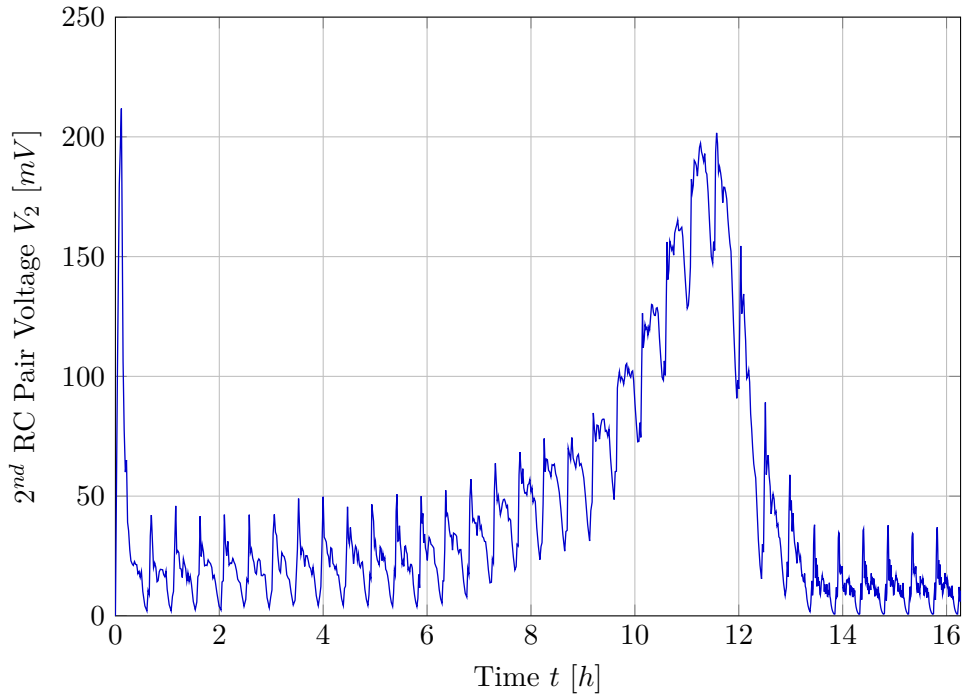


**Figure 4.27:** Voltage  $V_2$  generated by the cell model,  $-10\text{ }^\circ\text{C}$

It can be seen that, particularly for temperature  $-10\text{ }^\circ\text{C}$ , the cell model diverges significantly from the measured data at low state of charge (SOC) values. The cause might be attributed to an inaccuracy in open-circuit voltage identification, as described in Section 4.2.1. Furthermore, the values of the second resistor-capacitor (RC) pair might be inaccurate because it was observed that the second RC pair does not discharge fully in the rest time between measurement phases. Problems with RC values identification are described in Section 4.4.3. This behavior is depicted in Figure 4.27 and is represented by gradual ascent and descent around the middle of the test scenario. However, as stated earlier in this thesis, the general operating range of lithium cells is from 20 % to 80 % SOC. In this range, the overlap of the model and measurements is sufficient for all temperatures.

## 4.7 Conclusion of the Identification Phase

The identified model reflects cell behavior well in the SOC range  $\geq 20\%$ . Below this value, the parameters are considered inaccurate and further investigation should be conducted to improve the behavior if the operation in the SOC range  $\leq 20\%$  is desired in the future. Furthermore, thermal dynamics are still left to be identified. Thermal dynamics model identification and validation must be performed once the demonstration vehicle is prepared. Estimated look-up tables were stored in the form of a Matlab structure.





## Chapter 5

### State Estimation and Filtering

An extended Kalman filter (EKF), which was previously implemented in [12], was already available in the Garrett Motion repository. An unscented Kalman filter (UKF) was implemented for the sake of comparison. There are articles which state that UKF performs better than EKF when used for BMS state estimation. As an example, [6] or [23] and [24] can be cited. The superiority of UKF over EKF is supposedly due to the fact that UKF does not need to compute a Jacobian of the mathematical model. Numerical Jacobian approximation, which is needed by the EKF, using e.g. finite differences is an extra computational burden, and numerical inaccuracies are present when a nonlinear part of the model is encountered. Analytical Jacobian computation is not an option when the model contains look-up tables. UKF better suits this task because no jacobian is needed.

One of the goals of this thesis is to estimate the battery state of health (SOH) at runtime, an introduction to SOH estimation is provided first. This chapter then describes the implementation of UKF in Matlab. First, its conventional variant is presented, followed by its square root (SR-UKF) modification. The numerical properties of the implemented filters are then discussed, analyzed, and improved using a covariance matrix recovery algorithm. Possible improvements are also suggested. Finally, the conclusion of the estimator implementation phase is provided.

#### 5.1 State of Health Estimation

A general introduction to the SOH modeling methods is provided in Section 3.1.4 of this thesis. Thus, SOH is modeled according to equation 3.12.

With regard to the estimation of SOH degradation, section 4.6 of [22] provides mathematical derivation that shows that sensitivity of cell's output voltage to the total capacity is very small. Thus, estimating  $C_0$  is not an easy task. While in Section 4.4, the author of [22] derived a simple algorithm to estimate internal resistance from two consecutive cell measurements, this cannot be done in the case of capacity estimation, as the author states. The author of [22] further states that capacity is estimated more easily when a measurement containing a large SOC change is available. Two possible options for capacity estimation are provided in [22]. First, a nonlinear Kalman

filter is proposed. Second, regression techniques are discussed in [22].

In addition to the previously mentioned methods, machine learning is also widely used and tested for SOH estimation. As an example, [32] provides a survey of machine learning methods currently used for battery estimation.

The author of [12] used the Kalman filter approach. The nominal capacity  $C_0$  was modeled as an additional model state with zero dynamics.

$$\dot{C}_0 = 0 \quad (5.1)$$

Using Kalman filtering methods, a momentary estimate of nominal capacity degradation over time is provided. It can be noted that the value of  $C_0$  changes much slower than the other state variables such as the depleted charge  $Q_{dep}$ . However, the estimator can be guided to retain the nominal capacity value and change it very slowly by proper tuning. Specifically, if the model with zero dynamics for nominal capacity is trusted, (low Q matrix value for the Kalman filter) the estimator will change the nominal capacity value very slowly.

This thesis uses the same approach as [12] and compares the EKF previously implemented in [12] and newly implemented SR-UKF.

## 5.2 Conventional Unscented Kalman Filter

As stated in the introduction to this chapter, a basic form of the UKF was implemented first. UKF is part of a larger group of filters known as sigma point Kalman filters (SPKF). UKF was first proposed by the author of [10]. As stated in the cited article, the main problem that the UKF was designed to solve is estimation in nonlinear systems. The newly proposed technique is named *unscented transform* and is at the core of UKF.

### 5.2.1 Matlab Implementation

Basic UKF was implemented as a Matlab System class in the Garrett Motion Energy Management Framework (EMF). The class contains a reference to a model of the estimated plant that is used for propagation of the sigma points. Any dynamic model implemented in the EMF can be used with this filter. Furthermore, both continuous and discrete time models are supported.

The user can define input, output, and state scaling to improve the numerical properties of the filter. Thus, signals can be brought to a certain interval so that the values are in a similar order of magnitude. Furthermore, the user can specify the precision (single or double) with which the estimates are output.

Part of the UKF is a scaling parameter that controls the spread of sigma points. The user can specify it based on the needs of the current application. Each step of the filter is divided into separate data and time update step. The filter outputs the predicted next sample time output and state values.

### ■ Covariance Scaling

Because the filter implements input, output, and state scaling, the covariance matrices provided by the user need to be scaled accordingly. The following example illustrates how the covariance is scaled on the basis of the given scaling coefficients. Here, a mutual input-output scaled covariance is derived.

$$\begin{aligned}
 P_{xy} &= \begin{pmatrix} x_i - \hat{x} \\ c_{xi} \end{pmatrix} \begin{pmatrix} y_i - \hat{y} \\ c_{yi} \end{pmatrix}^T = \begin{bmatrix} \frac{\Delta x_{1,1}}{c_{x1}} \\ \frac{\Delta x_{1,2}}{c_{x2}} \end{bmatrix} \begin{bmatrix} \Delta y_{1,1} & \Delta y_{1,2} \\ c_{y1} & c_{y2} \end{bmatrix} \\
 &= \begin{bmatrix} \frac{\Delta x_{1,1} \Delta y_{1,1}}{c_{x1} c_{y1}} & \frac{\Delta x_{1,1} \Delta y_{1,2}}{c_{x1} c_{y2}} \\ \frac{\Delta x_{1,2} \Delta y_{1,1}}{c_{x2} c_{y1}} & \frac{\Delta x_{1,2} \Delta y_{1,2}}{c_{x2} c_{y2}} \end{bmatrix}
 \end{aligned} \tag{5.2}$$

The  $c_{xi}$  and  $c_{yi}$  parameters are the scaling coefficients of state  $x_i$  and output  $y_i$ , respectively. As observed in the very-last matrix, the scaling coefficients in the denominator form a dyad produced by the individual scaling coefficients.

### ■ Diagnostic Output

The UKF system also provides a diagnostic output that signals numerical issues encountered during runtime. In normal mode, the diagnostic port outputs 0. When a problem occurs, the output is set to 1 in the given sample time. If the problem does not occur again, the output returns to the value 0. Section 5.2.2 describes the numerical issues in more detail.

### ■ 5.2.2 Numerical Robustness Issues

In specific numerical conditions, it can be observed that UKF suffers from numerical instability. Namely, that the state covariance matrix can become non-positive definite. A non-positive definite covariance matrix causes numerical problems when the algorithm tries to decompose it using Cholesky factorization. [15] Cholesky factorization is used in UKF to compute the sigma points.

After a deeper investigation, it was found that the method by which the sigma points are computed affects the occurrence of this error. Specifically, a situation was encountered when simply transposing the covariance Cholesky factor solved the problem. That is, computing the sigma points using

$$x_i = \hat{x} \pm S_i \tag{5.3}$$

produced the error.  $S_i$  denotes the  $i^{th}$  column of the covariance Cholesky factor  $S$ . However, when using equation

$$x_i = \hat{x} \pm S_i^T, \tag{5.4}$$

the error did not occur. Although runtime errors in certain situations were mitigated, a different scenario was encountered where even this modification did not help to resolve the error. Therefore, SR-UKF was implemented.

### 5.3 Square Root UKF

As mentioned above, it was decided to implement the SR-UKF algorithm to resolve the above-mentioned numerical issue. SR-UKF is described in [18]. The author of [18] states, that “the square-root forms have the added benefit of numerical stability and guaranteed positive semi-definiteness of the state covariances.” With this being discovered, the SR-UKF was implemented in a very similar way as the conventional UKF. I.e., the Matlab System structure was preserved and only the necessary methods, which are different between these two implementations, were changed. This means that all the benefits described in Section 5.2 were preserved.

The square root implementation is superior to conventional UKF because Cholesky decomposition of covariance is computed only in the initialization phase of the filter and not at every sample time, as in the conventional UKF. In contrast, SR-UKF uses the computed Cholesky factor in every sample time, and all operations are conducted with the factored matrix. Some necessary covariance updates are computed using QR decomposition and a procedure called “cholupdate”, which is described in the next paragraph.

The function “cholupdate” computes a rank 1 update to the Cholesky factor matrix. [16] Cholesky update and downdate are distinguished based on the sign with which the rank 1 matrix is added to the original factored matrix.

Surprisingly, although it is stated that SR-UKF is numerically stable, it was observed that, in certain scenarios, the problem with non-positive definite covariance persists. This is caused by the following property of the “cholupdate” function. As the referenced documentation states, Cholesky downdate fails “when the downdated matrix is not positive definite and so does not have a Cholesky factorization.” The downdated matrix can in reality become negative definite if the rank 1 matrix, which is being subtracted, has a specific form that makes the overall matrix negative definite. Therefore, the Cholesky downdate operation is the high-risk part of the algorithm. With this being observed, a necessary covariance recovery method was implemented to prevent runtime errors caused by a negative definite covariance matrix both in both UKF and SR-UKF. The recovery method is described in Section 5.4.

### 5.4 Covariance Matrix Recovery

The covariance matrix recovery algorithm is a function of the implemented UKF and SR-UKF class, which is called when a problem with covariance definiteness occurs during runtime. This algorithm takes the original problematic covariance matrix and returns a Cholesky factor that corresponds to a positive definite matrix, which is close in a certain sense to the original covariance. The meaning of matrix closeness in this specific context is described later in this section. This algorithm was implemented after neither UKF nor SR-UKF provided sufficient numerical robustness.

In general, the recovery algorithm comprises decomposing the covariance matrix using spectral decomposition, manipulating the eigenvalues, and then composing back a modified covariance matrix with the desired properties. This modified matrix is then decomposed using Cholesky factorization, and the Cholesky factor is returned. Each of the abovementioned steps is described in more detail in the following sections.

### ■ 5.4.1 Covariance Decomposition

First, the input covariance matrix is decomposed using spectral decomposition

$$P_{in} = VDV^{-1} \quad (5.5)$$

as stated above. This procedure is inspired by [7] where a procedure for computing the nearest symmetric positive semidefinite matrix is described.

A necessary step is to prove that all matrices that can be expected at the input have their spectral decomposition. In Theorem 2.1 of [7] and its proof, the author requires the matrix  $A$ , which is to be made positive semidefinite, to be only square and real. The author then forms a matrix  $B = \frac{(A+A^T)}{2}$  which is then in the proof decomposed by spectral decomposition. Thus, if our input covariance matrix is real, square, and symmetric, it has its spectral decomposition according to proof of Theorem 2.1 in [7]. After the input covariance matrix is decomposed, a discussion on numerical tolerance for positive definiteness is provided in the next section. Eigenvalue manipulation is described later.

### ■ 5.4.2 Numerical Tolerance for Positive Definiteness

Before describing the procedure of manipulating the eigenvalues, a note on tolerance for positive definiteness from the numerical point of view must be presented. A specific procedure for testing for numerical positive definiteness is provided in [4]. The authors suggest comparing all eigenvalues to the value of a Matlab expression `length(d)*eps(max(d))`, where  $\mathbf{d}$  is a vector of eigenvalues, `length(d)` is the number of eigenvalues, and the term `eps(max(d))` corresponds to the order of the highest eigenvalue. If any of the eigenvalues are smaller than the tolerance

$$d_i < \text{length}(\mathbf{d}) \cdot \text{eps}(\max(\mathbf{d})), \quad \forall i, \quad (5.6)$$

the matrix is considered non-positive definite. This tolerance term is further explained in the following paragraph.

The floating point representation of numbers in a computer must be considered. The format of the floating point number representation is standardized in the IEEE 754 standard. In short, a floating point number is represented by 3 values: sign, mantissa, and exponent. The Matlab function `eps(x)` “returns the positive distance from `abs(x)` to the next larger floating-point number of the same precision as `x`.” [17] For double precision representation, where a

number  $x$  is represented by a 52-bit mantissa and its exponent  $e$  is offset by  $-1023$ , the value of  $\text{eps}(x)$  can be analytically represented as

$$\text{eps}(x) = 2^{-52} \cdot 2^{e-1023} = 2^{e-1075}. \quad (5.7)$$

This procedure of defining tolerance based on the current matrix eigenvalues is very helpful and will be used in a later description of the recovery algorithm. The usefulness is mainly caused by the fact that analytical positive definiteness is not sufficient. A matrix with positive eigenvalues with large differences in exponents does not need to be considered as positive definite by the numerical implementation of Cholesky decomposition in Matlab. However, from the analytical point of view, this matrix is truly positive definite. Next, the procedure of eigenvalue manipulation to achieve numerical positive definiteness is described.

### ■ 5.4.3 Eigenvalue Manipulation

Second, when the input matrix is decomposed and robust numerical tolerance is defined, the eigenvalues can be manipulated to achieve the desired numerical positive definiteness. In [7], the author suggests in the proof of Theorem 2.1 to set all negative eigenvalues to 0.

$$d_i = \begin{cases} d_i, & d_i \geq 0 \\ 0, & d_i < 0 \end{cases} \quad (5.8)$$

Thus, positive semi-definiteness is achieved. The author of [7] further states that by this approach, the “nearest symmetric positive semidefinite matrix in the Frobenius norm to an arbitrary real matrix” is composed (after composing the matrix back, which is described in the next section.) Our goal, however, is to find not a semidefinite matrix, but a positive definite one. Thus, the aforementioned procedure is further modified.

The implemented procedure first takes the absolute value of all the eigenvalues. Thus, the magnitude of the eigenvalues is preserved. Second, all eigenvalues are saturated from below by a lower threshold  $10^{-6}$ . Finally, an upper bound on eigenvalues is computed on the basis of the value of the smallest eigenvalue. With this upper bound, all eigenvalues are saturated from above.

### ■ Derivation of the Upper Bound

The eigenvalue upper bound is computed on the basis of the tolerance described in Section 5.4.2. From equation (5.6), the following requirement for all eigenvalues can be derived.

$$d_i > \text{length}(d) \cdot \text{eps}(\max(d)), \quad \forall i, \quad (5.9)$$

If the focus is on double-precision floating-point representation and the exponent of the largest eigenvalue is denoted as  $e_m$ , an analytical bound on

$e_m$  can be derived. Manipulation of equation (5.9) gives

$$d_i > \text{length}(\mathbf{d}) \cdot 2^{e_m - 1075}, \quad \forall i, \quad (5.10)$$

$$\frac{d_i}{\text{length}(\mathbf{d})} > 2^{e_m - 1075}, \quad \forall i, \quad (5.11)$$

$$\log_2 \left( \frac{d_i}{\text{length}(\mathbf{d})} \right) + 1075 > e_m, \quad \forall i, \quad (5.12)$$

where the values of  $\mathbf{eps}(\mathbf{x})$  from equation (5.7) were used. An analytical expression to compute the maximal possible exponent based on the smallest eigenvalue can be derived from equation (5.12).

$$e_m = \lfloor \log_2 \left( \frac{\min(d_i)}{\text{length}(\mathbf{d})} \right) \rfloor + 1074 \quad (5.13)$$

With an appropriate value of the exponent  $e_m$ , the upper bound for the actual eigenvalue can be computed. This can be done by considering the largest floating point number in double precision with an exponent equal to  $e_m$ . Such a number is represented as

$$(1.\underbrace{111\dots 1}_{52\times})_2 \cdot 2^{e_m - 1023}, \quad (5.14)$$

where

$$(1.\underbrace{111\dots 1}_{52\times})_2 \approx (1.9999999999999998)_{10} > (1.9999)_{10}. \quad (5.15)$$

Thus, using the eigenvalue upper bound

$$d_{max} = 1.9999 \cdot 2^{e_m - 1023}, \quad (5.16)$$

where  $e_m$  was computed according to equation (5.13), provides a numerically safe upper bound for all eigenvalues.

Matrix with saturated eigenvalues on its diagonal

$$d_i = \begin{cases} d_i, & 10^{-6} \leq d_i \leq d_{max} \\ 10^{-6}, & d_i < 10^{-6} \\ d_{max}, & d_i > d_{max} \end{cases} \quad (5.17)$$

is later denoted as  $\bar{D}$ . The process of covariance backward composition is described below.

#### 5.4.4 Composition of the Modified Matrix

In the second to last step of the covariance recovery algorithm, the modified covariance matrix is composed back. Backward composition of the form

$$P_{out} = V\bar{D}V^{-1} \quad (5.18)$$

can be performed. However, it is possible to replace inversion with transposition.

A classical spectral decomposition takes the form of equation (5.18). I.e., inversion is used. Here, a derivation of the fact that the spectral decomposition of a real and symmetric matrix is

$$P_{out} = V\bar{D}V^T \quad (5.19)$$

which is equivalent to  $V\bar{D}V^{-1}$ . This replacement improves the computation time and numerical accuracy of the algorithm.

As a quick explanation, the proof of Theorem 2.1 in [7] can be referenced because the author uses spectral decomposition with transposition instead of inversion. However, a more in-depth derivation is provided in the following paragraphs.

Schur decomposition of matrix  $P$

$$P = VUV^{-1} \quad (5.20)$$

contains by definition eigenvalues of  $P$  on the diagonal of the upper triangular matrix  $U$ . [29] But if  $P$  is normal, then  $U$  is diagonal. [28] A normal matrix is defined in [28] as a matrix with the property  $AA^* = A^*A$ , where the operator  $*$  denotes a conjugate transposition. Furthermore, if  $P$  is real and symmetric, [28] provides a fact that Schur decomposition becomes

$$P = VUV^T. \quad (5.21)$$

By stating these facts, it can be concluded that since our covariance matrix is real and symmetric, its Schur decomposition leads to a diagonal matrix  $U$ , and thus the spectral decomposition can be composed as

$$P_{out} = V\bar{D}V^T. \quad (5.22)$$

#### ■ 5.4.5 Computation of the Returned Cholesky Factor

In the last step, computation of the Cholesky factor of the modified covariance matrix is discussed. Although all computations are performed in the real domain, Matlab Code Generator does not recognize this fact. When a simulation is attempted to run in Code Generation mode, an error is thrown stating that the Code Generator cannot assure that the covariance matrix  $P_{out}$ , which is being decomposed using the Cholesky decomposition, is real. Therefore, a real part of the matrix  $P_{out}$  is extracted first, and then a final Cholesky decomposition is performed. In this way, the Code Generator accepts the input as formally correct.

### ■ 5.5 Possible Improvements

Although the covariance recovery algorithm was implemented to assure numerical stability of the implemented (SR-)UKF, there are other UKF implementations that should supposedly guarantee positive definiteness of the covariance matrix. As a reference, [19] can be cited. The authors claim that



they “propose a mathematically equivalent filter that numerically guarantees positive semi-definiteness for any arithmetic precision at the cost of a negligible runtime increase.”

Furthermore, additional research on possible improvements of the implemented recovery algorithm can be conducted to improve execution time. Possible simplifications and computational complexity reduction can be investigated.

## 5.6 Conclusion of the Estimator Implementation Phase

In this chapter, the SOH estimation methods were analyzed and estimation using an additional zero-dynamics state  $C_0$  was described. Furthermore, two implementations of the UKF were presented, namely the conventional UKF and SR-UKF. Both filters were implemented as Matlab System classes in the Garrett Motion EMF and were fully documented. The problem of covariance positive definiteness was resolved using a covariance recovery algorithm, which was precisely described and explained. Possible improvements were considered for future development and the implementation of another UKF version was suggested.



## Chapter 6

### Testing and Validation

In the previous chapters, model selection, model identification, and estimator implementation were described. When the model parameters are fixed and the state estimator is implemented, formal testing and validation must be performed to check if the model and estimator performance meet the required criteria.

In this section, the root-mean-square error calculation is established first. Next, a validation procedure, which supports the neglect of coulombic efficiency, is presented. Next, the state estimator is validated using modified real driving experience (RDE) data in a model-in-the-loop (MIL) scenario. Then, the estimator is validated using raw RDE data, and the computation time on the target hardware is presented. The conclusion of the testing and validation phase is provided together with an overall conclusion in Chapter 7.

Graphs are labeled using cell identifiers established in Table 2.1 of this thesis.

#### 6.1 Root Mean Square Error

To objectively quantify the quality of the validation data, the root-mean-square error (RMSE) is used. A definition of RMSE is provided in this section to ensure the correct interpretation of the provided data.

RMSE for signal processing is defined for the purpose of this thesis as

$$\text{RMSE}(\theta, \hat{\theta}) = \sqrt{E \left( (\theta_i - \hat{\theta}_i)^2 \right)}, \quad (6.1)$$

where  $\theta_i$  denotes a true sample value at time  $i$ ,  $\hat{\theta}_i$  denotes estimated or modelled sample value at time  $i$  and  $E$  denotes the operator of the expected value.

#### 6.2 Validation of Neglecting Coulombic Efficiency

An experiment was performed after the cell model was identified, which supports the neglect of coulombic efficiency. Drive cycle measurement data were taken and the cell model (without coulombic efficiency) was fed with the

same inputs as the cell during real measurement was driven with. Drive cycle data were considered appropriate because they simulate a real environment and contain many consecutive charge and discharge pulses, which makes them suitable for this test.

The discharged capacity at the end of the simulation was compared with the discharged capacity at the end of the real cell measurement. A summary of this experiment is presented in Table 6.1. The absolute difference between the simulated and measured discharged capacity is presented in the column  $Q_{diff}$ . Furthermore, the ratio of  $Q_{diff}$  compared to the total discharged capacity is presented. It can be seen that the difference is in the range of tenths per mille, and thus, coulombic efficiency truly represents a negligible value for this particular cell type.

$T$ [°C]	$Q_{diff}$ [mAh]	$Q_{diff}$ [‰]
-10	0.3	0.1
0	0.4	0.1
25	0.5	0.2
50	0.5	0.2

**Table 6.1:** Difference in total drained capacity, absolute difference and relative difference with respect to total drained capacity.

### 6.3 Estimator MIL Validation

In this section, estimator MIL validation is described. The MIL scenario consists of real RDE input data that are fed into the cell model. RDE inputs are then combined with model outputs. Model outputs were combined with white noise to simulate the measurement noise. These signals form an input to the estimator, which is being validated. For this validation, square root unscented Kalman filter (SR-UKF, Section 5.3) and extended Kalman filter (EKF, implemented by [12]) are compared. Schematic depicting the connection between individual elements of this scenario is shown in Figure 6.1.

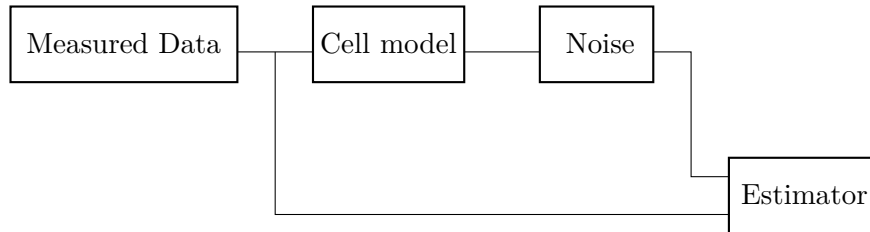


**Figure 6.1:** MIL scenario schematic

The RDE data used for MIL validation were modified to suit the validation purposes. The RDE data were repeated multiple times with simple charging

phases inserted. In this way, multiple discharge cycles were executed to simulate real-world operating conditions.

The MIL validation procedure consists of three scenarios. In the first scenario, the estimator response to incorrect initial conditions was tested. The second scenario tests the filter response to cell capacity degradation. The last scenario validates whether the filter correctly estimates through changing temperature conditions. The filter covariance setup is kept the same for all validation scenarios. Apart from the ambient temperature operation validation, all other MIL validations were executed at ambient temperature 25 °C. The symbols used in the following sections correspond to the cell model described by equations (3.15)-(3.20). All three scenarios are described in more detail in the following sections.

### 6.3.1 Incorrect Initial Conditions

The first validation scenario compares SR-UKF and EKF with respect to incorrect initial condition response. While the cell model was initialized with a value of  $Q_d = 1000$  As (see equation (3.16)) and  $C_0 = 3.4$  Ah (see equation (5.1)), the filters were initialized with values  $Q_d = 0$  As and  $C_0 = 2$  Ah.

The terminal voltage is depicted in Figure 6.2. The nominal capacity is depicted in Figure 6.3, depleted charge in Figure 6.4 and state of charge in Figure 6.5. It can be seen that both filters arrive at the model reference sufficiently fast and then track the dynamics very well. Table 6.2 shows RMSE values for the above mentioned signals. UKF performs better with respect to all mentioned signals.

Signal	RMSE SR-UKF	RMSE EKF
$V_{trm}$ [mV]	2.7	6.8
$C_0$ [Ah]	0.26	0.35
SOC [%]	0.34	0.76
$Q_{dep}$ [As]	417	658

**Table 6.2:** RMSE values for estimator validation, incorrect initial condition scenario

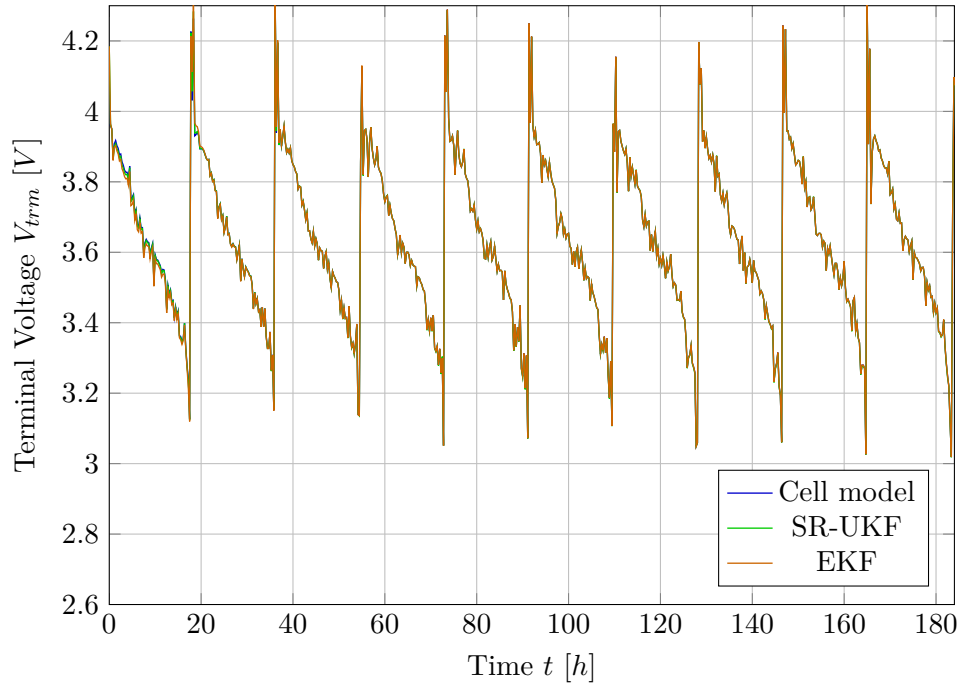


**Figure 6.2:** Estimator validation, response to incorrect filter initial conditions, terminal voltage course

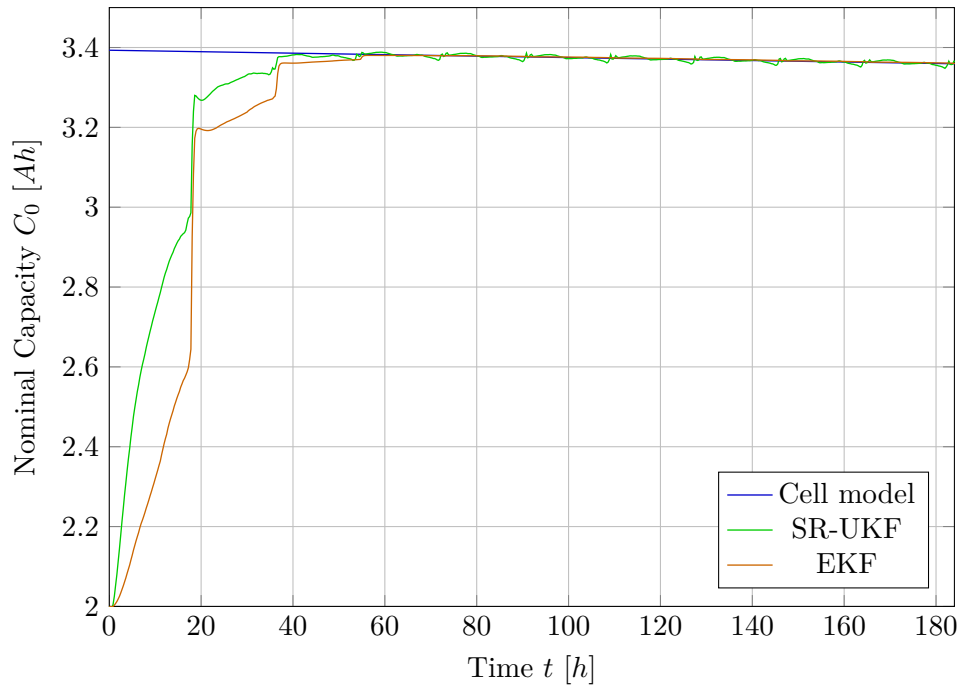


**Figure 6.3:** Estimator validation, response to incorrect filter initial conditions, nominal capacity course

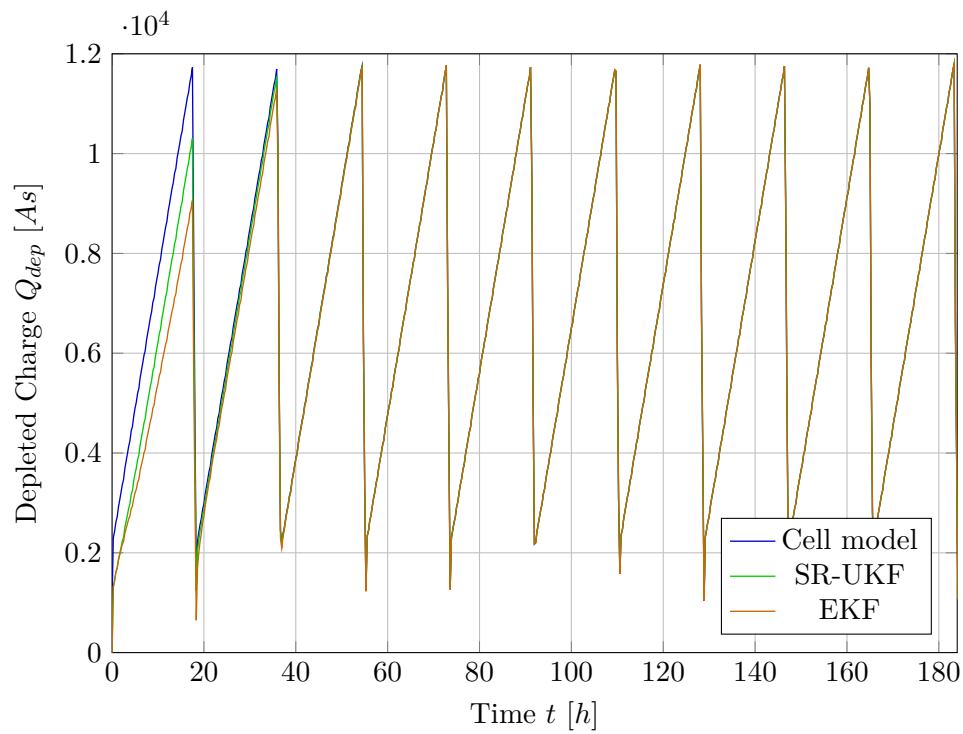


**Figure 6.4:** Estimator validation, response to incorrect filter initial conditions, depleted charge course

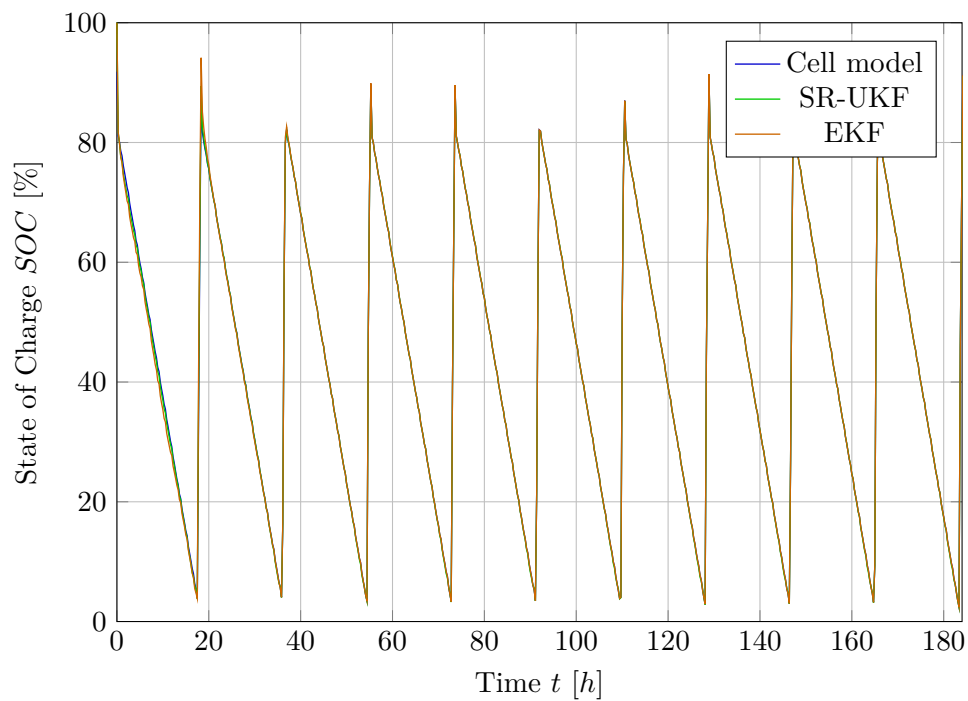


**Figure 6.5:** Estimator validation, response to incorrect filter initial conditions, state of charge course

### 6.3.2 Capacity Degradation

The next validation scenario consists of testing whether the filter can track the nominal capacity decrease during the simulation time. This time, a larger  $C_0$  decrease was set up compared with the previous validation scenario. The filter initial conditions were the same as for the cell model.

Table 6.3 depicts computed RMSE values for both SR-UKF and EKF. It can be seen that for this scenario, SR-UKF tracks the depleted charge and nominal capacity better than EKF. However, EKF is better at tracking the terminal voltage and SOC. The terminal voltage course is depicted in Figure 6.6. Nominal capacity is depicted in Figure 6.7, depleted charge in Figure 6.8 and state of charge in Figure 6.9. It can be observed that both filters estimate the signals precisely.

Signal	RMSE SR-UKF	RMSE EKF
$V_{term}$ [mV]	1.0	0.7
$C_0$ [mAh]	7.5	19.5
SOC [%]	0.10	0.08
$Q_{dep}$ [As]	7.6	39.3

**Table 6.3:** RMSE values for estimator validation,  $C_0$  decrease scenario

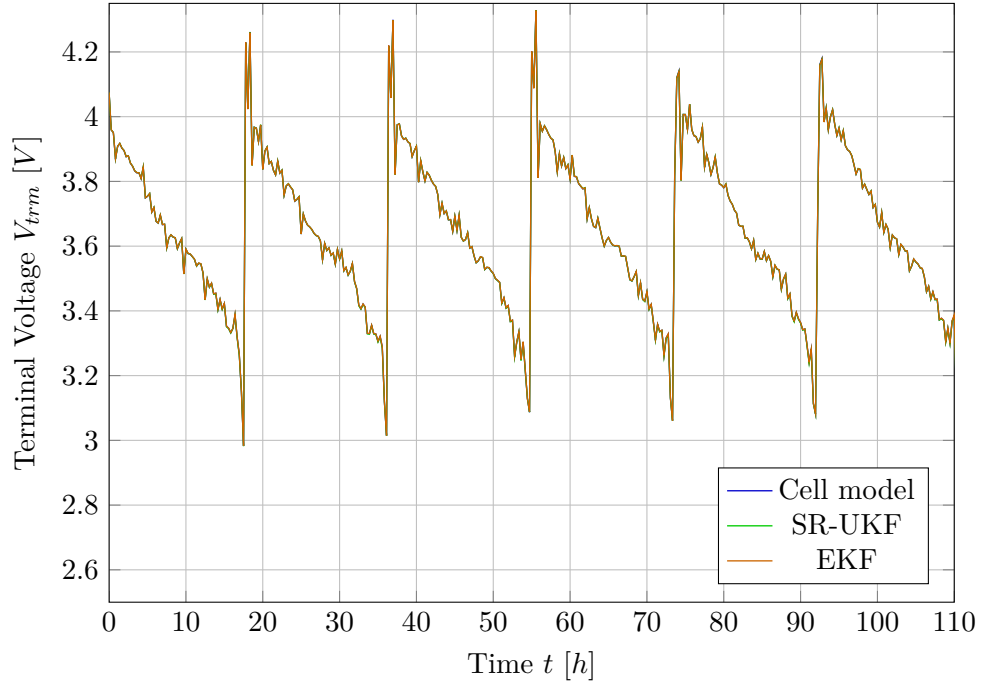


**Figure 6.6:** Estimator validation, response to nominal capacity decrease, terminal voltage course



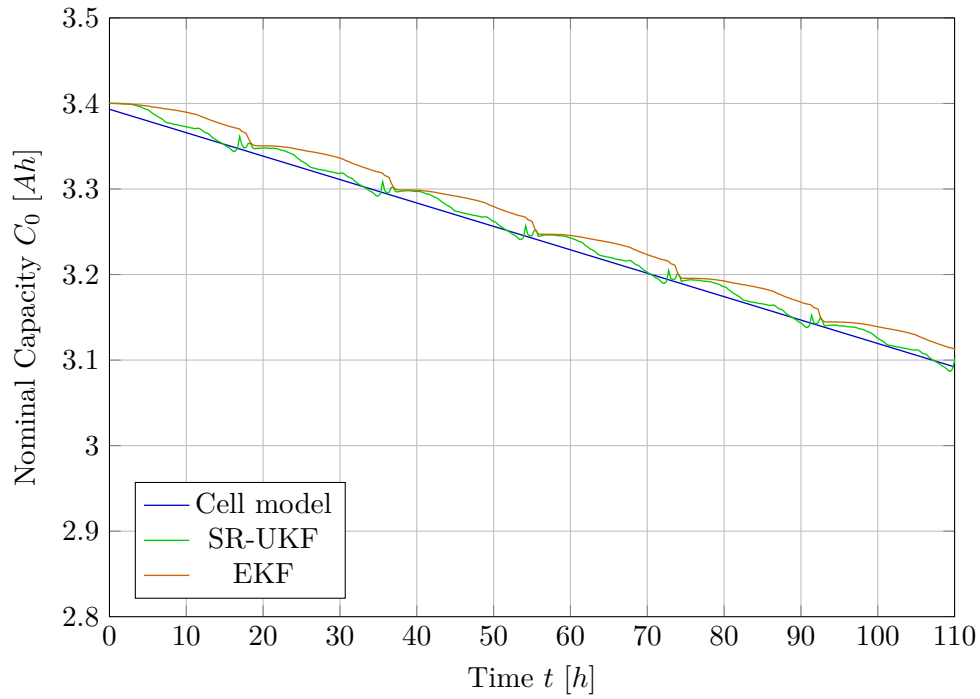


**Figure 6.7:** Estimator validation, response to nominal capacity decrease, nominal capacity course

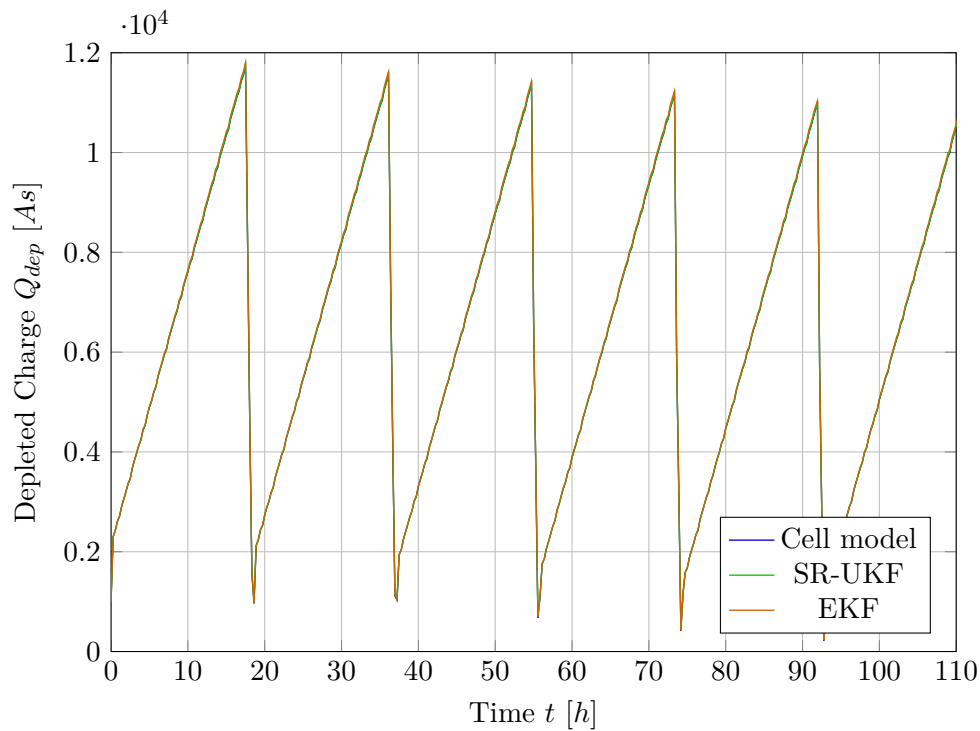


**Figure 6.8:** Estimator validation, response to nominal capacity decrease, depleted charge course

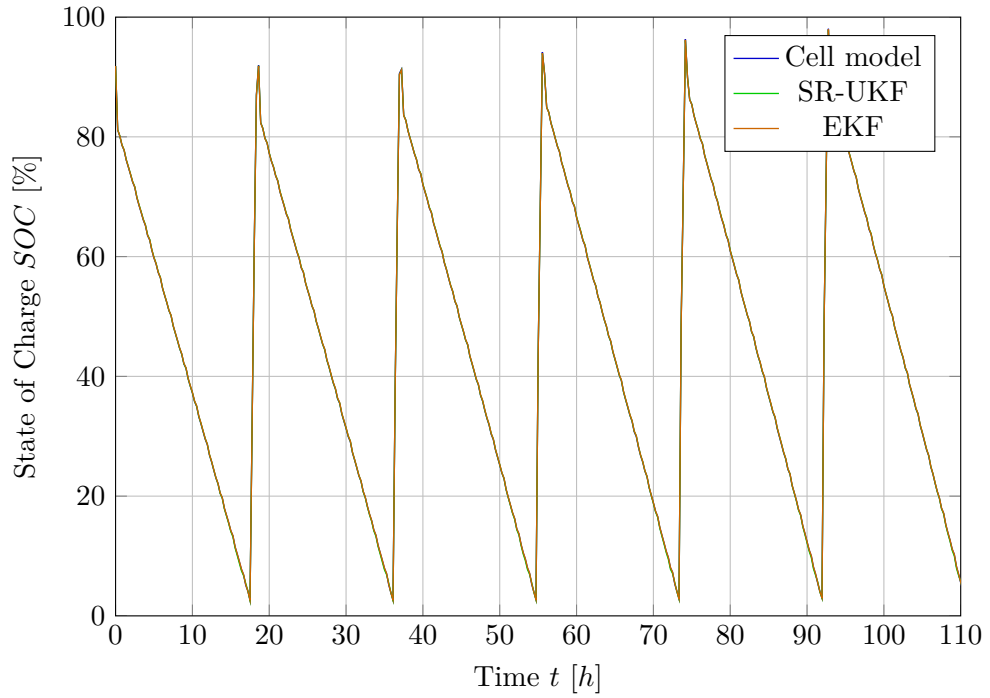


**Figure 6.9:** Estimator validation, response to nominal capacity decrease, state of charge course

### 6.3.3 Temperature Behavior

In this scenario, all initial conditions were the same for both the cell model and the estimator. The estimator's ability to estimate when the ambient temperature changes throughout the simulation time was validated. The ambient temperature was simulated in such a way that it exceeded the temperature range of the identified look-up tables. In this way, it was validated that there are no runtime errors originating in look-up table extrapolation issues. It must be noted here, that this validation scenario is not intended to test cell model thermal dynamics. The cell model thermal dynamics was not identified as described in Section 4.5.

Table 6.4 depicts comparison of RMSE values for both SR-UKF and EKF. It can be seen that EKF exhibits lower RMSE values than SR-UKF. The terminal voltage is depicted in Figure 6.10. The nominal capacity is depicted in Figure 6.11, depleted charge in Figure 6.12 and state of charge in Figure 6.13. The ambient temperature course is depicted in Figure 6.14. Even for this scenario, it can be stated that the signals are estimated properly.

Signal	RMSE SR-UKF	RMSE EKF
$V_{trm}$ [mV]	1.4	0.9
$C_0$ [mAh]	7.0	2.4
SOC [%]	0.15	0.01
$Q_{dep}$ [As]	6.1	4.6

**Table 6.4:** RMSE values for estimator validation, ambient temperature change scenario

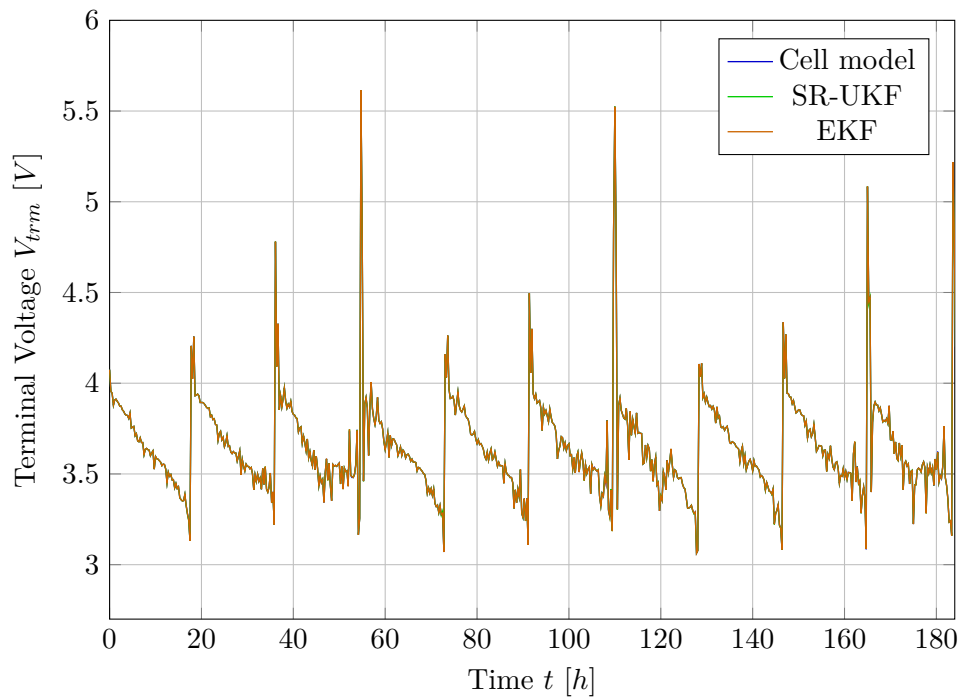


**Figure 6.10:** Estimator validation, response to ambient temperature change, terminal voltage course

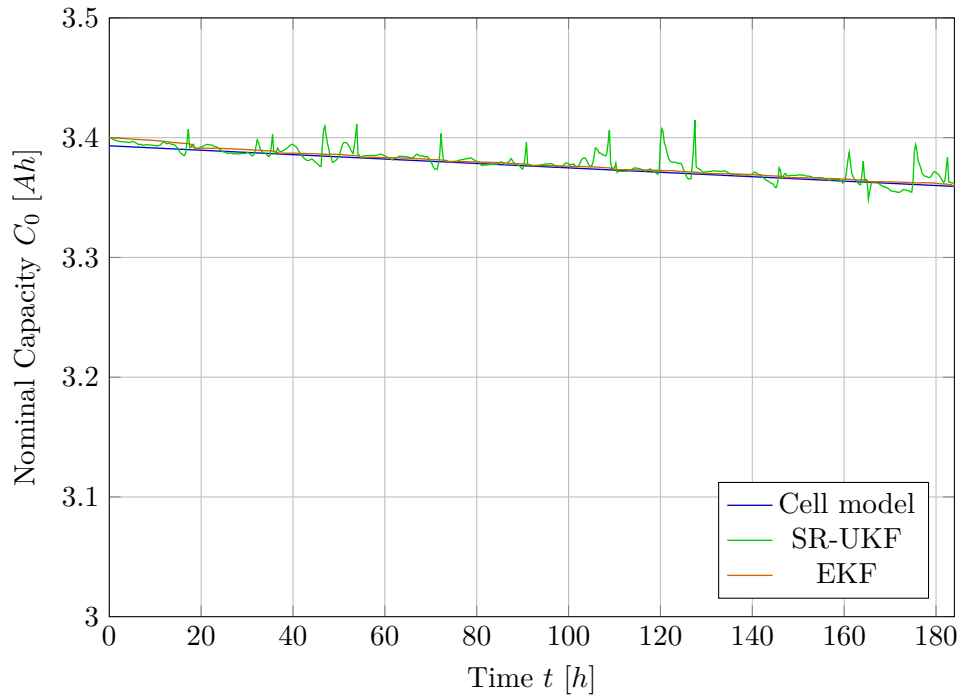


**Figure 6.11:** Estimator validation, response to ambient temperature change, nominal capacity course

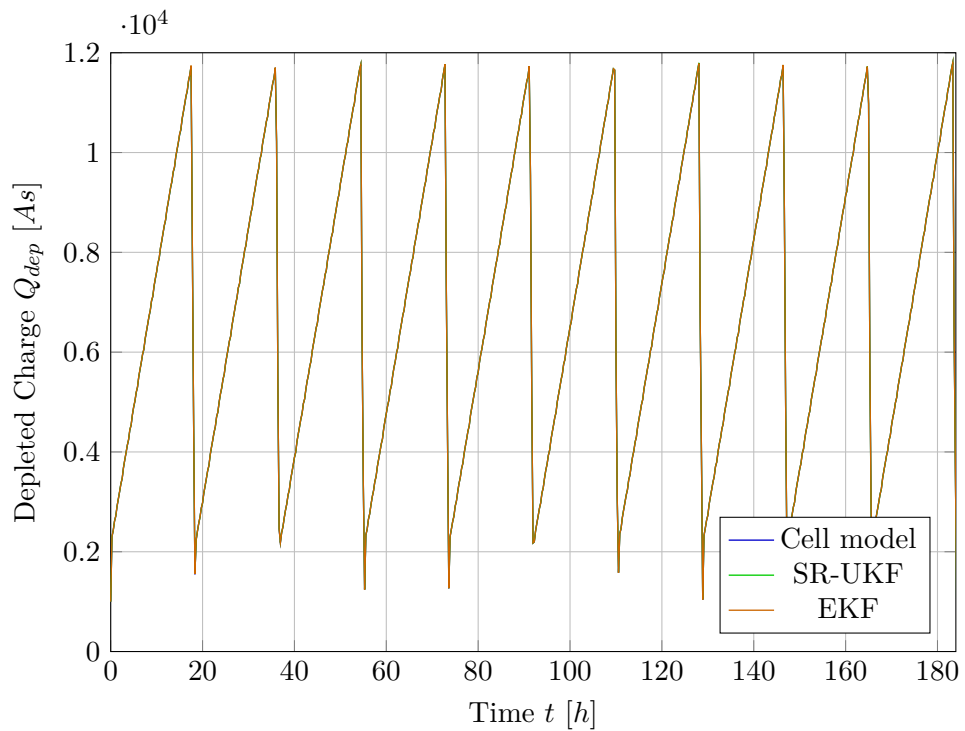


**Figure 6.12:** Estimator validation, response to ambient temperature change, depleted charge course

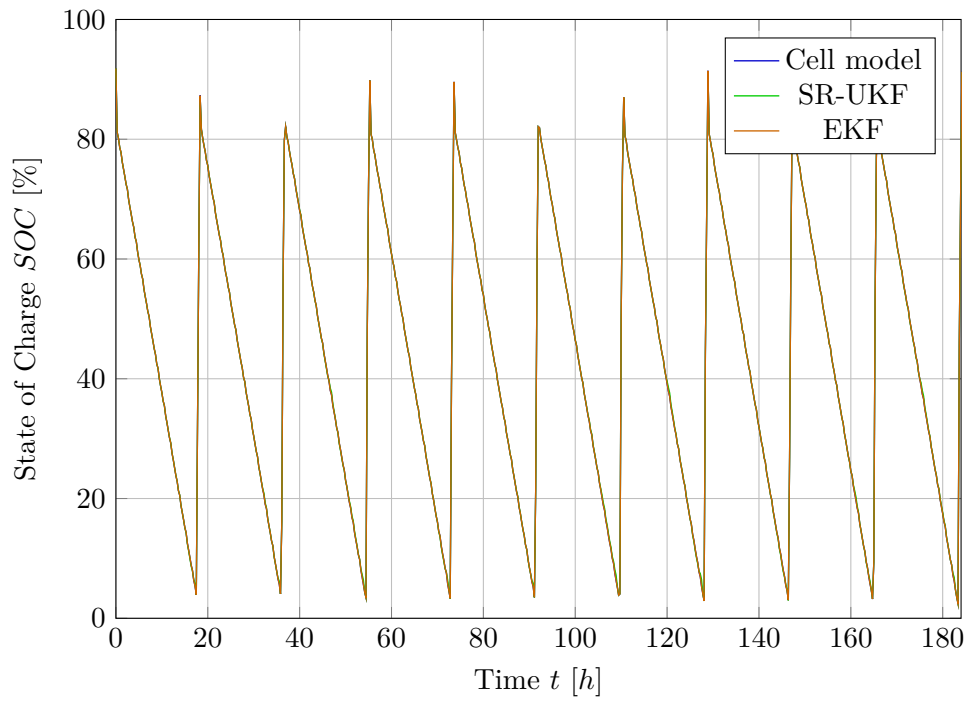


**Figure 6.13:** Estimator validation, response to ambient temperature change, state of charge course

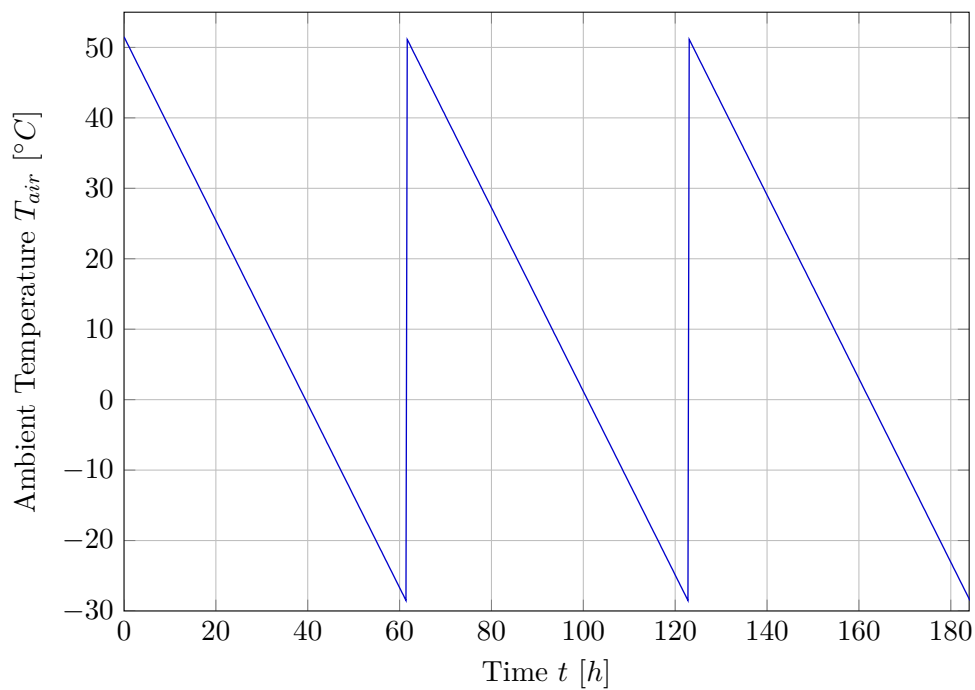


**Figure 6.14:** Estimator validation, response to ambient temperature change, ambient temperature course

## 6.4 Estimator RDE Data Validation

Next, the estimator was validated using raw measured data. That is, terminal voltage and cell temperature signals were taken directly from the obtained data set. Here, SR-UKF and EKF were compared as well. Intentionally, the initial nominal capacity of the filters was set to 3 Ah to test the estimator response. The true cell capacity is  $\approx 3.39$  Ah.

Table 6.5 depicts RMSE values of SR-UKF and EKF for comparison. It can be seen that here, SR-UKF is superior for signal tracking. Signal courses are depicted in Figures 6.15, 6.16, 6.17 and 6.18. It can be observed that terminal voltage tracking works well. However, the nominal capacity estimation does not reach the true value over the simulation time. This can be caused by the length of the validation data. Since there is no cell model in this scenario that generates terminal voltage and cell temperature signals, drive cycle data cannot be supplemented with an artificial charge phase and repeated to simulate more discharge-charge cycles. If more discharge-charge cycles were measured in the laboratory, the capacity estimation would improve after several cycles.

Signal	RMSE SR-UKF	RMSE EKF
$V_{trm}$ [mV]	3.4	5.1
$Q_{dep}$ [As]	147.2	301.1

**Table 6.5:** RMSE values for estimator validation, RDE data scenario

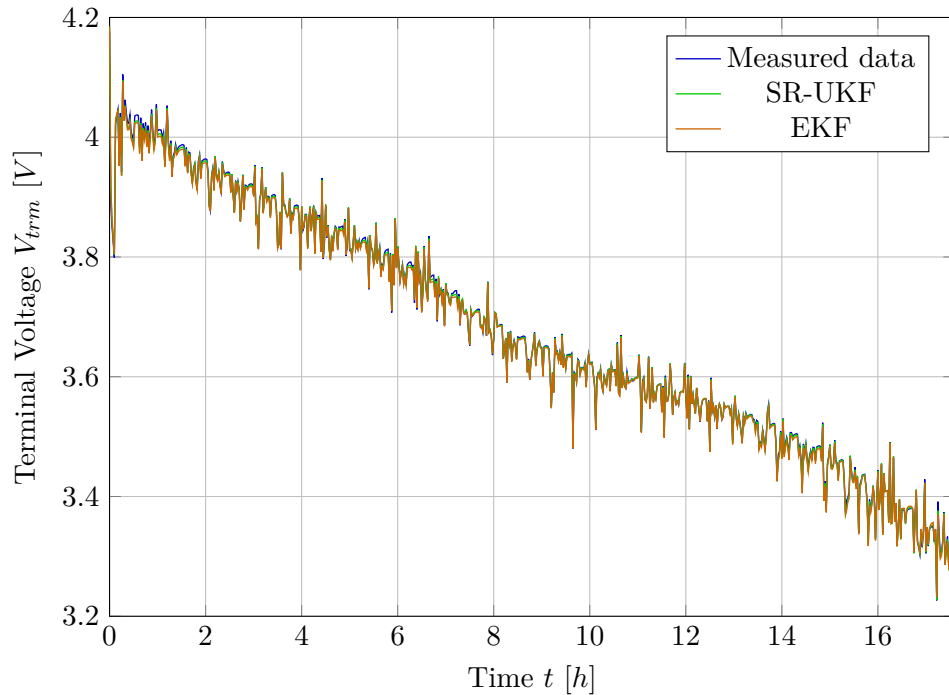


**Figure 6.15:** Estimator validation, RDE data scenario, terminal voltage course

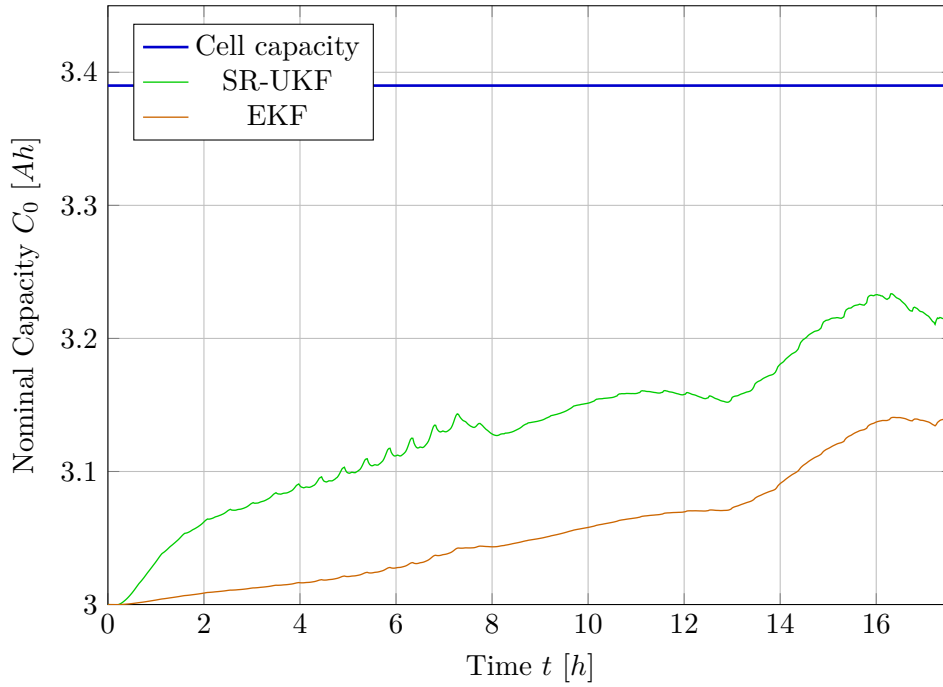


**Figure 6.16:** Estimator validation, RDE data scenario, nominal capacity course

## 6.5 Execution Time Measurement

In this validation scheme, a C code for the SR-UKF and EKF estimators was generated using Simulink Coder. This code was executed on the target vehicle computer. The computer operates on Intel Code i7 dual core processor with DDR3 memory capable of operation at up to 1600 MHz. Raw measured data were used as input. The goal was to measure the execution time of both filters. The time was measured using `CLOCK_THREAD_CPUTIME_ID` under Linux. Thus, the time spent only on filter execution was measured.

The statistical results are presented in Table 6.6. It can be seen that although SR-UKF exhibits a larger maximal execution time value, the minimal and average values are lower than those for EKF. Histogram in Figure 6.19 shows that the overall execution time of SR-UKF is superior to EKF. The large maximal execution time value of SR-UKF is caused by one measurement outlier around 220  $\mu\text{s}$ .

	SR-UKF	EKF
Minimum [ $\mu\text{s}$ ]	37.0	62.1
Maximum [ $\mu\text{s}$ ]	215.9	158.2
Average [ $\mu\text{s}$ ]	38.9	65.0

**Table 6.6:** Execution time statistics, comparison of SR-UKF and EKF

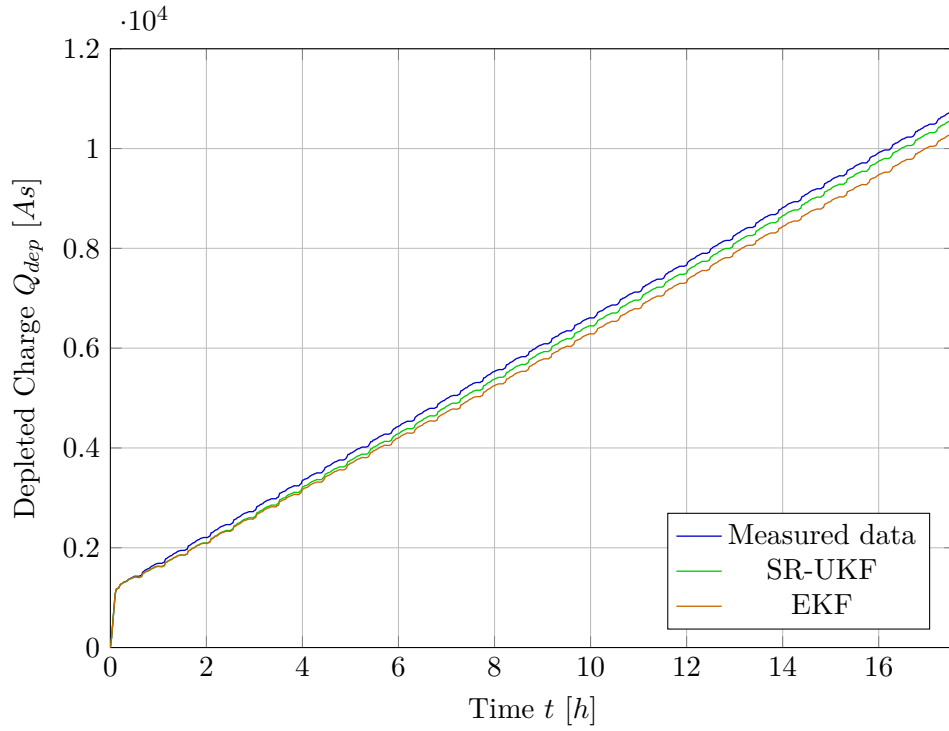


**Figure 6.17:** Estimator validation, RDE data scenario, depleted charge course

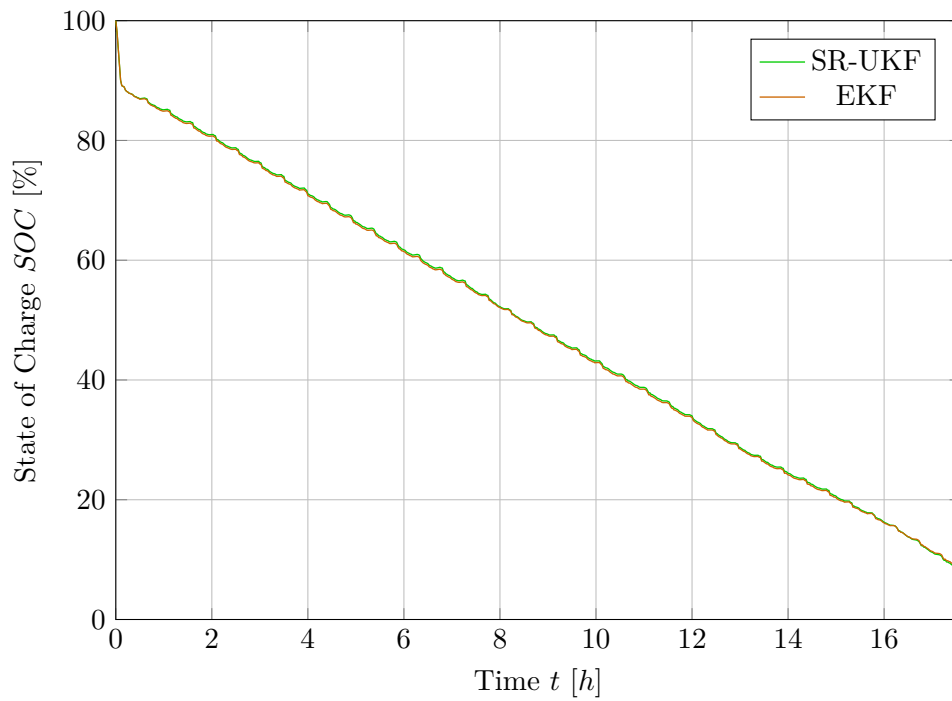


**Figure 6.18:** Estimator validation, RDE data scenario, state of charge course



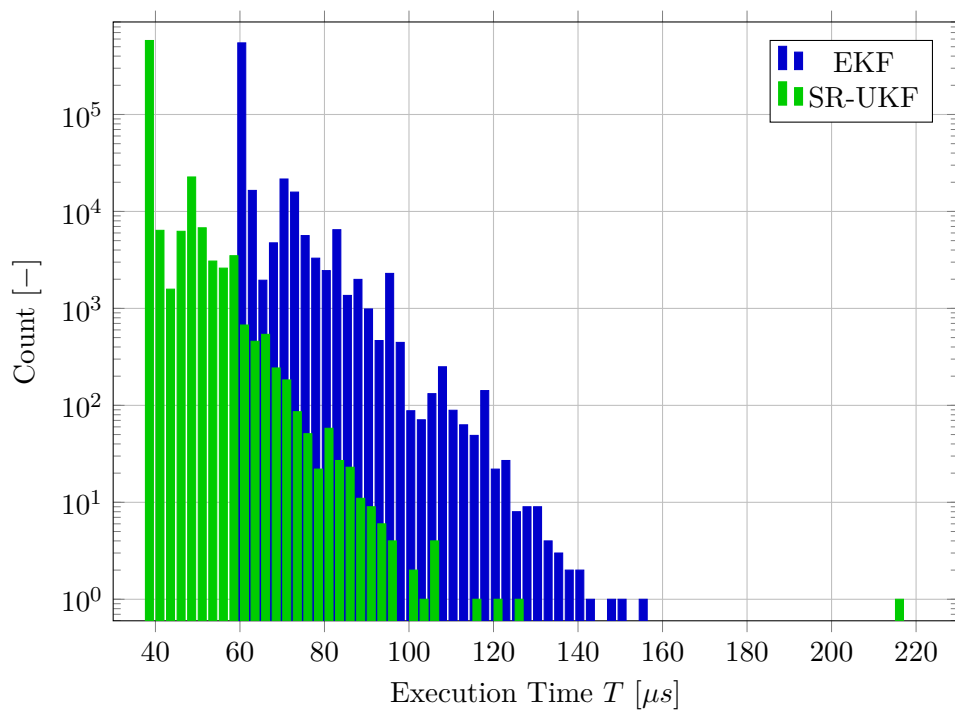


**Figure 6.19:** Histogram of execution times on the target computer



# Chapter 7

## Conclusion

### 7.1 Overall Results

The process of cell state and parameter estimator development was presented in this thesis. The obtained laboratory measurements were presented and cell model selection was described. The model was improved compared to [12]. The improvement consisted of modifying the state of charge (SOC) modeling and simplifying the thermal dynamics. The approach of using a cell model to simulate the entire battery pack was described.

The modeling framework of Garrett Motion Company was extended by the new cell models. The first model does not contain nominal capacity  $C_0$  as a separate state, and thus capacity degradation cannot be estimated using standard Kalman filtering methods. The second model contains  $C_0$  as a separate state and was used in the Kalman filters to validate the estimators.

Next, the model identification procedure was outlined. The obtained measurement data were used to estimate the cell parameter dependency on the state of charge and temperature. Because the demonstration vehicle being not assembled, the thermal dynamics was not identified. Further, the state estimator was implemented in two variants, namely the conventional unscented Kalman filter and square root unscented Kalman filter (SR-UKF). Because neither of the two variants provided sufficient numerical robustness, a covariance recovery algorithm was implemented to prevent runtime errors that terminated estimator execution.

Lastly, testing and validation procedures were conducted to examine whether the cell model and implemented SR-UKF performed correctly. The cell model simulates the real battery cells well enough in the main operation range from 20 % to 80 % SOC. A comparison of SR-UKF with an extended Kalman filter implemented in [12] was presented. Overall, both filters estimate the cell state variables well enough. However, SR-UKF exhibits a lower execution time on average. Testing and validation were performed using only simulations.

## 7.2 Possible Extensions of this Work

As stated in Section 4.5, the thermal dynamics of the cell model were not identified because the demonstration vehicle was not assembled at the time of work on this thesis. Therefore, it is advised to conduct identification measurements of the thermal dynamics of the battery pack after the vehicle is fully assembled.

If it is desired to operate the battery at a low SOC range, it is recommended to improve the battery model. Possible improvements include hysteresis or Warburg impedance modelling [21]. If possible, electrochemical impedance spectroscopy measurements can be performed to improve cell model identification. [2]

In addition, adding hysteresis into the equivalent circuit model might improve the dynamics of the passive side of pulses, as described in Section 4.4.2. Moreover, in general, charging dynamics might be improved by incorporating hysteresis.

Next, it is proposed to investigate whether the provided method of simulating the whole battery pack, presented in Section 3.2, is sufficient. After the demonstration vehicle is fully assembled, validation measurements should be performed to compare the behavior. In particular, it is advised to conduct the validation measurements at low ambient temperature if operation in such ambient conditions is desired. It is stated in [26] that “. . . in the case of HEVs and PHEVs including high power battery packs containing hundreds of cells some phenomena are exaggerated or even some are seen only in battery packs not in single cells. This shows that modeling battery packs of HEVs and PHEVs needs special attention.”<sup>1</sup> Thus, if the method proposed in Section 3.2 shows to be inaccurate, [13] or [26] are advised to be investigated.

As stated in Section 5.5, there is another unscented Kalman filter implementation, which guarantees numerical stability. It is advised to test this implementation if it performs better from the estimation and execution time viewpoints.

---

<sup>1</sup>Hybrid Electric Vehicle (HEV), Plug-in Hybrid Electric Vehicle (PHEV)





## Appendix A

### Bibliography

- [1] United States Environmental Protection Agency. *Dynamometer Drive schedules*. <https://www.epa.gov/vehicle-and-fuel-emissions-testing/dynamometer-drive-schedules> (Accessed on 5.1.2024).
- [2] Ed Brorein. *A deeper look at lithium-ion cell internal resistance measurements*. <https://www.keysight.com/blogs/tech/bench/2022/05/31/a-deeper-look-at-lithium-ion-cell-internal-resistance-measurements> (Accessed on 5.1.2024). June 2022.
- [3] Filip Dašek. ‘Vehicle steering systems development’. <http://hdl.handle.net/10467/109030> (Accessed on 5.1.2024). Bachelor’s Thesis. 2023.
- [4] *Determine Whether Matrix Is Symmetric Positive Definite*. <https://www.mathworks.com/help/matlab/math/determine-whether-matrix-is-positive-definite.html> (Accessed on 5.1.2024). The MathWorks, Inc.
- [5] EV Europe. *Tesla Model S module*. <https://eveurope.eu/en/product/tesla-model-s-module-53-kwhr-24-vdc/> (Accessed on 5.1.2024).
- [6] Hongwen He et al. ‘Comparison Study on the Battery SoC Estimation with EKF and UKF Algorithms’. In: *Energies* 6.10 (2013). <https://www.mdpi.com/1996-1073/6/10/5088> (Accessed on 5.1.2024), pp. 5088–5100. ISSN: 1996-1073. DOI: 10.3390/en6105088.
- [7] Nicholas J. Higham. ‘Computing a nearest symmetric positive semidefinite matrix’. In: *Linear Algebra and its Applications* 103 (1988). <https://www.sciencedirect.com/science/article/pii/0024379588902236> (Accessed on 5.1.2024), pp. 103–118. ISSN: 0024-3795. DOI: [https://doi.org/10.1016/0024-3795\(88\)90223-6](https://doi.org/10.1016/0024-3795(88)90223-6).
- [8] M. Hossain, M.E. Haque, and M.T. Arif. ‘Kalman filtering techniques for the online model parameters and state of charge estimation of the Li-ion batteries: A comparative analysis’. In: *Journal of Energy Storage* 51 (2022). <https://www.sciencedirect.com/science/article/pii/S2352152X22002067> (Accessed on 5.1.2024), p. 104174. ISSN: 2352-152X. DOI: <https://doi.org/10.1016/j.est.2022.104174>.

- [9] Tarun Huria et al. ‘High fidelity electrical model with thermal dependence for characterization and simulation of high power lithium battery cells’. In: *2012 IEEE International Electric Vehicle Conference*. 2012, pp. 1–8. DOI: 10.1109/IEVC.2012.6183271.
- [10] Simon J. Julier and Jeffrey K. Uhlmann. ‘New extension of the Kalman filter to Nonlinear Systems’. In: *SPIE Proceedings (1997)*. DOI: 10.1117/12.280797.
- [11] Stanislav Kolman. ‘Tesla Cybertruck je další splněný sen Elona Muska. Odolá střelbě a na stovce překoná hypersporty’. In: *Auto.cz* (2019). <https://www.auto.cz/tesla-cybertruck-je-dalsi-splneny-sen-elona-muska-odola-strelbe-a-na-stovce-prekona-hypersporty-132153> (Accessed on 5.1.2024).
- [12] Jan Kučera. ‘EV battery pack State of Charge and State of Health estimation’. <http://hdl.handle.net/10467/101620> (Accessed on 5.1.2024). Master’s Thesis. 2022.
- [13] Jianwei Li and Michael S. Mazzola. ‘Accurate battery pack modeling for automotive applications’. In: *Journal of Power Sources* 237 (2013). <https://www.sciencedirect.com/science/article/pii/S037877531300373X> (Accessed on 5.1.2024), pp. 215–228. ISSN: 0378-7753. DOI: <https://doi.org/10.1016/j.jpowsour.2013.03.009>.
- [14] Lifu Li and Jifei Li. ‘Research on Modeling and Characteristic Parameters Consistency of Retired Lithium Power Batteries’. In: *IOP Conference Series: Earth and Environmental Science* 358.5 (Dec. 2019). <https://dx.doi.org/10.1088/1755-1315/358/5/052063> (Accessed on 5.1.2024), p. 052063. DOI: 10.1088/1755-1315/358/5/052063.
- [15] *Matlab Documentation for chol*. <https://www.mathworks.com/help/matlab/ref/chol.html> (Accessed on 5.1.2024). The MathWorks, Inc.
- [16] *Matlab Documentation for cholupdate*. <https://www.mathworks.com/help/matlab/ref/cholupdate.html> (Accessed on 5.1.2024). The MathWorks, Inc.
- [17] *Matlab Documentation for eps*. <https://www.mathworks.com/help/matlab/ref/eps.html> (Accessed on 5.1.2024). The MathWorks, Inc.
- [18] Rudolph Merwe and Eric Wan. ‘The Square-Root Unscented Kalman Filter for State and Parameter-Estimation’. In: vol. 6. Feb. 2001, 3461–3464 vol.6. ISBN: 0-7803-7041-4. DOI: 10.1109/ICASSP.2001.940586.
- [19] Tino Milschewski and Jean-François Bariant. ‘A numerically stable formulation of the square root unscented Kalman filter for state estimation’. In: *2017 20th International Conference on Information Fusion (Fusion)*. 2017, pp. 1–7. DOI: 10.23919/ICIF.2017.8009711.
- [20] *Panasonic Lithium Ion NCR18650B datasheet*. <https://www.batteryspace.com/prod-specs/ncr18650b.pdf> (Accessed on 10.9.2023). 2012.
- [21] Gregory L. Plett. *Battery Management Systems, Volume 1 - Battery Modeling*. Artech House, 2015. ISBN: 978-1-63081-023-8.



- [22] Gregory L. Plett. *Battery Management Systems, Volume 2 - Equivalent-Circuit Methods*. Artech House, 2016. ISBN: 978-1-63081-027-6.
- [23] Gregory L. Plett. ‘Sigma-point Kalman filtering for battery management systems of LiPB-based HEV battery packs: Part 1: Introduction and state estimation’. In: *Journal of Power Sources* 161.2 (2006). <https://www.sciencedirect.com/science/article/pii/S0378775306011414> (Accessed on 5.1.2024), pp. 1356–1368. ISSN: 0378-7753. DOI: <https://doi.org/10.1016/j.jpowsour.2006.06.003>.
- [24] Gregory L. Plett. ‘Sigma-point Kalman filtering for battery management systems of LiPB-based HEV battery packs: Part 2: Simultaneous state and parameter estimation’. In: *Journal of Power Sources* 161.2 (2006). <https://www.sciencedirect.com/science/article/pii/S0378775306011438> (Accessed on 5.1.2024), pp. 1369–1384. ISSN: 0378-7753. DOI: <https://doi.org/10.1016/j.jpowsour.2006.06.004>.
- [25] Dana Popp. *Euro 7: Deal on new EU rules to reduce road transport emissions*. <https://www.europarl.europa.eu/news/en/press-room/20231207IPR15740/euro-7-deal-on-new-eu-rules-to-reduce-road-transport-emissions> (Accessed on 5.1.2024). 2023.
- [26] Arash Shafiei, Ahmadreza Momeni, and Sheldon S. Williamson. ‘Battery modeling approaches and management techniques for Plug-in Hybrid Electric Vehicles’. In: *2011 IEEE Vehicle Power and Propulsion Conference*. 2011, pp. 1–5. DOI: 10.1109/VPPC.2011.6043191.
- [27] Weixiang Shen, Thanh Tu Vo, and Ajay Kapoor. ‘Charging algorithms of lithium-ion batteries: An overview’. In: *2012 7th IEEE Conference on Industrial Electronics and Applications (ICIEA)*. 2012, pp. 1567–1572. DOI: 10.1109/ICIEA.2012.6360973.
- [28] Marco Taboga. *Normal matrix, Lectures on matrix algebra*. <https://www.statlect.com/matrix-algebra/normal-matrix> (Accessed on 5.1.2024). 2021.
- [29] Marco Taboga. *Schur decomposition, Lectures on matrix algebra*. <https://www.statlect.com/matrix-algebra/Schur-decomposition> (Accessed on 5.1.2024). 2021.
- [30] Monica Tutuianu et al. *Development of a World-wide Worldwide harmonized Light duty driving Test Cycle (WLTC)*. Tech. rep. <https://unece.org/DAM/trans/doc/2014/wp29grpe/GRPE-68-03e.pdf> (Accessed on 5.1.2024). The United Nations Economic Commission for Europe, 2013.
- [31] Vojtěch Ullmann. ‘Vehicle brake system development’. <http://hdl.handle.net/10467/109024> (Accessed on 5.1.2024). Bachelor’s Thesis. 2023.
- [32] Carlos Vidal et al. ‘Machine Learning Applied to Electrified Vehicle Battery State of Charge and State of Health Estimation: State-of-the-Art’. In: *IEEE Access* 8 (2020), pp. 52796–52814. DOI: 10.1109/ACCESS.2020.2980961.

- [33] Wladislaw Waag, Stefan Käbitz, and Dirk Uwe Sauer. ‘Experimental investigation of the lithium-ion battery impedance characteristic at various conditions and aging states and its influence on the application’. In: *Applied Energy* 102 (2013). <https://www.sciencedirect.com/science/article/pii/S030626191200671X> (Accessed on 5.1.2024), pp. 885–897. ISSN: 0306-2619. DOI: <https://doi.org/10.1016/j.apenergy.2012.09.030>.